

**Study on the Electrical Properties and
Microstructure of Bismuth-Based High Voltage
Zinc Oxide Varistors**

A Dissertation Submitted in Partial Fulfillment
Of the Requirements for the Degree Of
Doctor of Engineering

Graduate School of Science and Engineering
Doshisha University

Yumeng Zheng

November 2021

Table of Contents

List of Symbol	v
Chapter 1 General Introduction.....	1
Chapter 2 ZnO varistors: overview and applications	5
2.1 ZnO varistors	5
2.2 Applications of ZnO varistors	8
2.2.1 ZnO varistors: types and applications	8
2.2.2 High voltage varistors for UHV applications.....	10
Chapter 3 Principles of ZnO varistors	12
3.1 Electrical properties and typical parameters	12
3.2 Microstructure and electro ceramic processes	13
3.2.1 Microstructure	14
3.2.2 Chemical reaction mechanisms during sintering.....	15
3.2.3 Additives effects on electrical properties	16
3.3 Conductive mechanisms	17
3.3.1 Double Schottky barriers.....	17
3.3.2 Interface states and oxygen absorption	18
3.4 Degradation phenomena and the mechanisms	18
Chapter 4 Experimental procedure.....	22
4.1 Sample preparation	22
4.2 Density determination.....	23
4.3 Thermal Annealing treatment.....	23
4.4 Evaluation methods.....	23
4.4.1 Electrical characteristics.....	23
4.4.2 Electrical degradation.....	23
4.4.3 Capacitance – voltage characteristics.....	24
4.4.4 Isothermal capacitance transient spectroscopy (ICTS)	25
4.5 Microstructure observation methods.....	27
4.5.1 Crystallographic evaluation with X-Ray diffraction	27
4.5.2 Scanning electron microscopy	28
4.5.3 Transmission electron microscopy	28

4.5.4 Electron probe micro analyzer	29
Chapter 5 Effect of Cr₂O₃ and NiO on Y-doped high voltage ZnO varistors..	31
5.1 Introduction.....	31
5.2 Utilization of Y ₂ O ₃ and Sb ₂ O ₃ amount	32
5.3 Sample Preparation	33
5.4 Microstructure and Crystal structure with Cr or Ni addition.....	34
5.5 Electrical properties	38
5.5.1 Electrical degradation under DC bias.....	42
5.5.2 Interface state levels at gran boundaries.....	43
5.6 Simulation of electrical properties with thermionic mechanism model and comparison with experimental results	46
5.6.1 Simulation with thermionic mechanism model.....	46
5.6.2 Relationship between Electrical properties and interface states.....	49
5.7 Conclusion	52
Chapter 6 Effect of B₂O₃ on Y-doped high voltage ZnO varistors.....	55
6.1 Experimental procedures	56
6.2 Microstructure and the location of boron.....	56
6.3 Effect of B ₂ O ₃ additives on electrical properties	62
6.4 Thermal annealing effects	64
6.5 Analysis of interface states and double Schottky barriers	65
6.6 An analytical method for conducting processes of ZnO varistors	68
6.7 Relationship between B ₂ O ₃ and SiO ₂ additives.....	78
6.7.1 Microstructure and crystal structure when B ₂ O ₃ and SiO ₂ were added together	78
6.7.2 Electrical properties when B ₂ O ₃ and SiO ₂ added together	80
6.8 Conclusions.....	82
Chapter 7 High voltage Bi-based ZnO varistors adding with SiO₂.....	86
7.1 Introduction.....	86
7.2 Experiments	87
7.2.1 Sample preparation.....	87
7.2.2 Sample Evaluation.....	87
7.3 Microstructure and Crystallographic properties	88
7.3.1 Microstructure	88
7.3.2 Crystal structure	91

7.3.3 Relative mass density	97
7.4 Electrical properties	98
7.4.1 Voltage–current characteristics.....	98
7.4.2 Electrical degradation.....	101
7.4.3 Interface state levels and barrier structure	103
7.5 Effects of B ₂ O ₃ on improvement of electrical degradation	105
7.6 Conclusion	108
Chapter 8 Conclusion and outlook	112

ACKNOWLEDGEMENTS

List of Symbol

Symbol	Description
A^*	Richardson constant
C	capacitance
$C(t)$	transient capacitance
$C_{\text{NGB}}(V)$	capacitance when the DC bias voltage V is applied
e	electron charge
E_B	energy with respect to the Fermi level E_{FG} for ZnO grain
E_C	conduction band
$E_C - E_{\text{IS}i}$	the depth of i -th interface state level from E_C
E_F	quasi-Fermi level
E_{FG}	Fermi level for a ZnO grain
$E_{\text{IS}i}$	the i -th interface state level
E_V	valence band
f_B	potential barrier height
f_{B0}	equilibrium height of the double Schottky barriers
g	the degeneracy of the trap levels ($g = 1$)
h	Planck's constant
I	forward-biased Schottky barrier region
II	interface between I and III where the interface states are formed
III	reverse-biased Schottky barrier region
J	current density
J_D	leakage current density during degradation
J_L	leakage current density, the value of the current density at 80% of V_{NN}
$J_{L130^\circ\text{C}}$	leakage current density at 130°C
k_B	Boltzmann constant
m_e	rest mass of an electron
m_e^*	effective mass of an electron in ZnO

Symbol	Description
N_D	donor density
$N_{IS}(E)$	interface state density
N_{IS0}	interface state density under zero bias
N_{ISi}	density of electrons captured under V_{PHGB} at the i -th interface state level
N_{ISMAX}	total density of interface states between E_V and E_C
R_D	differential resistivity
$R_D(J)$	J -dependent differential resistivity
$S(V_{GB})$	the increase rate for interface charges
S_G	ZnO grain size
S_{MAX}	maximum of the increase rate for interface charges
V	voltage
V_{GB}	applied voltage per grain boundary
V_N	voltage per 1-mm sample thickness
V_{NN}	varistor voltage, voltage per 1mm thickness at current density $J = 1 \text{ mA/cm}^2$
V_{NNGB}	varistor voltage per single grain boundary
V_{phGB}	pulsed bias voltage per grain boundary
w_{DL0}	width of the depletion layer
α	non-linearity coefficient
α_{as}	non-linearity coefficient in the breakdown region
α_{asMAX}	experimental maximum point for the nonlinearity index
α_{MAX}	theoretical maximum value of the nonlinearity index
β_i	distribution parameter for τ_i caused by the distribution of interface state levels
$\Gamma(x)$	Euler's gamma function for x
ε	relative permittivity of ZnO
ε_0	permittivity of vacuum
θ	angle of incidence
λ	wave length

Symbol	Description
$\rho(E)$	energy density of the interface state levels
$\Sigma(00X)$	Integral of intensity of XRD diffraction peak
σ_i	capture cross-sectional area for the i -th interface state level
τ_{0i}	specific time constant for electron emission from the i -th interface state level
Φ_B	Schottky barrier height
Φ_{B0}	Schottky barrier height at zero bias

Chapter 1

General Introduction

Safe electric power supply is vital for the stabilization of a nation's electrical production, energy usage, industrial operations, and people's lives that enable an emerging information society in modern life. In recent years, electric supplementation has become increasingly important due to fossil fuel depletion. According to the latest report on the sustainable development goal, one out of ten people still lacks electricity. A growing concern is energy efficiency, refinement of the requirement and supply relationship to build a smart grid and power distribution systems that can be applied to all power sources including green energy, fossil fuel power, nuclear power.

With regard to electricity supplementation and preventing power outages, it is imperative to prevent the damage caused by switching surges, lightning strikes, and so on. Surge arresters serve this purpose, which are a key device for safe electric power supply around the world.

Variators are the main body of a surge arrester. A varistor ¹, which is a portmanteau of variable resistors, is an electronic component with “diode-like” nonlinear voltage–current ($V-I$) characteristics. There are several types of varistors according to the materials, such as silicon carbide (SiC) varistors ², zinc oxide (ZnO) varistor ³, titanium oxide (TiO₂) varistors ⁴, tin oxide (SnO₂) varistors ⁵, and so on. Among them, ZnO varistors are the most popular due to their excellently high nonlinear resistance characteristic and the rapid surge absorption ability ⁶⁻⁸, emerged with the rapid applications of the gapless surge protectors as a revolution of traditional gapped SiC arresters.

The first arrester came into use in the early 1930s ². These first materials were composed of sintered SiC ceramics, which applied to electrical power delivery systems and telephone systems in the 1960s. SiC arrester has low nonlinearity of the $V-I$ characteristics that causes problems such as large leakage current. Therefore, air gaps between series SiC bulks are necessary. However, new problems such as response time delay, follow current, and others are caused by those air gaps. In the 1970s, Matsushita Electric developed the first ZnO varistor ³. Comparing to SiC, ZnO varistors showed extremely low leakage current and high nonlinearity ^{3,6-8}, large surge absorption ability, which lead gapless arrester design became possible. After that ZnO varistors spread the whole world quickly. The improvement of ZnO varistors processes and properties were investigated for decades by researchers around the world.

ZnO varistor, which is a ceramic composed of primarily ZnO and a few amounts of multiple metal oxide additives, is formed from complicated reaction processes during sintering³. Its novel grain boundary properties⁹ between ZnO and intergranular layer contribute to the special nonlinear $V-I$ characteristics that lead to the large surge absorption ability. ZnO varistor is a voltage-dependent switching device, which exhibits highly nonohmic $V-I$ characteristics above the breakdown voltage. The ZnO varistors in normal applications operate as insulators when their voltage is below the breakdown voltage, so they do not conduct any current. When triggered by overvoltage, such as lightning strikes, it will shunt the current created by the high voltage away from sensitive components.

Today, ZnO varistors are available to protect devices over a very wide range of voltage, from a few volts electro-static discharge (ESD) for low voltage varistors in circuits to 1100kV in electrical power transmission networks⁸. Their stable and flat nonlinear $V-I$ characteristics made them suitable for different usage in lightning arresters, gas insulated switchgear (GIS), and switching surge suppression^{6,10}.

Development of 1100kV ultra-high-voltage (UHV) electricity transmission technology is more and more important and necessary to improve energy efficiency and reduce power loss for long-distance transmission^{11,12}. The withstand level, set amount, and position of surge arresters are designed according to the overvoltage caused by lightning strikes and switching surges in power systems. However, increasing the number of surge arresters for UHV transmission will also increase the cost. Reduction of the resistance of ZnO varistors under overvoltage to improve the surge conducting properties is also needed. This could be achieved by adding metal additives such as aluminum (Al) or gallium (Ga) to ZnO to increase the donor density and decrease the ZnO resistance^{12,13}. Furthermore, although the arrester's working voltage (which is called varistor voltage for ZnO varistors) can be increased by simply increasing the number of ZnO varistors in device, in this case, the size of surge arresters will also be largely increased which may be more than few meters. Considering the layout of the transmission system and the limited area in the city, downsizing of surge arresters is also needed. Hence, ZnO varistors need to be improved in order to be used in UHV transmission. ZnO varistors that exhibit high working voltage, good nonlinear characteristics, and high electrical stability are required.

When absorbing large surge energy as lightning, the temperature of the varistor rises together with the increase of leakage current, which leads to energy loss and damaged devices. Electrical degradation is also one big problem for the application of a lightning arrester. Commonly, leakage current will also be increased while increasing the varistor voltage of ZnO

varistors. Lack of studies was reported on the electrical degradation in recent days and direct proof of the degradation mechanisms was not found.

The author's target is to investigate ZnO varistors with a high varistor voltage to 1000V/mm (double of the commercial one) and good resistance to electrical degradation, which could be applied to the UHV transmission systems and reduce the ZnO varistor element amount in surge arresters. Varistor voltage is dependent on the number of grain boundaries between two electrodes and the voltage per single boundary. There are two methods to increase it, one is reducing the ZnO grain size and the other is increasing the voltage per single boundary. Both can be adjusted by additive doping. Also, the mechanisms and the conduction process in ZnO varistors need to be clarified. The effects of each additive and interaction between them with ZnO are essential to control the electrical properties of ZnO varistors.

The aims of this doctoral thesis are to improve the electrical properties of Bi-based ZnO varistors by doping Yttrium (Y), Chromium (Cr), Nickel (Ni), Boron (B), Silicon (Si) oxides as additives, clarifying the degradation phenomena, summary and create a guideline for the measurement of ZnO varistors. Chapter 1 is a brief introduction to this thesis. Chapter 2 introduces the background and application of ZnO varistors. Chapter 3 summarizes the principle of ZnO varistors, such as the electrical properties, the microstructure, the electrical degradation, and so on. Chapter 4 is the experimental method used in the study. Chapter 5 discusses the effects of Cr and/or Ni additives on Y-doped ZnO varistors. Chapter 6 studies the B addition to Y-doped ZnO varistors. Chapter 7 describes the high voltage ZnO varistors by controlling the Si amount. A summary and an outlook are discussed in chapter 8.

References

1. F.R. Stansel, The characteristics and some applications of varistors. Proc. I.R.E. 39 (1951) 342–358.
2. K.B. McEachron, Thyrite: a new material for lightning arresters. Gen. Electr. Rev.,33 (1930) 92–99.
3. M. Matsuoka, Nonohmic properties of zinc oxide ceramics. Jpn. J. Appl. Phys. 10 (1971) 736–746.
4. M. F. Yan and W. W. Rhodes, Preparation and properties of TiO₂ varistors, Appl. Phys. Lett., 40 (1982) 536-537.
5. P. R. Bueno, S. A. Pianaro, et.al., Investigation of the electrical properties of SnO₂ varistor system using impedance spectroscopy, J. Appl. Phys., 84 (1998) 3700.
6. T.K. Gupta, Applications of zinc oxide varistors, J. Am. Ceram. Soc., 73 (1990) 1817–1840.
7. M. Matsuoka, T. Masuyama, Y. Iida, Voltage nonlinearity of zinc oxide ceramics doped with alkali earth metal oxide. Jpn. J. Appl. Phys. 8 (1969) 1275–1276.
8. 松岡道雄, 細川武, 沖中秀行, 江田和生, 酸化亜鉛バリスタ: 日本が生んだ世界的発明, オーム社, (2009).
9. A.T. Santhanam, T.K. Gupta, W.G. Carlson, Microstructural evaluation of multicomponent ZnO ceramics. J. Appl. Phys. 50 (1979) 852–859.
10. T. Fukano, M. Mizutani, Y. Kayano, Y. Kasuga and H. Andoh, Development of GIS type surge arrester applying ultra high voltage gradient ZnO element, PES T&D 2012, (2012) 1-5.
11. Cuixia Zhang, Jianbin Fan, UHV Transmission Technology, Academic Press, 2018.
12. M. Candas, O. S. Meric, The Application of Ultra High Voltage in the World, J. Power Energy Eng., 3 (2015) 453-457.
13. T.K. Gupta, A.C. Miller, Improved stability of the ZnO varistor via donor and acceptor doping at the grain boundary, J. Mater. Res. 3 (1988) 745–754.
14. B. wen Wang, B. hui Chen, P. zhao Gao, H. hui Chen, P. Zhang, Mechanism of Ga₂O₃ addition on the enhancement of electrical and mechanical properties of ZnO based varistor, Ceram. Int. 47 (2021) 4157–4165.

Chapter 2

ZnO varistors: overview and applications

2.1 ZnO varistors

ZnO varistors are devices whose resistance is variable and dependent on the applied voltage, widely used to protect circuits and electric power transmission systems from overvoltage and subnormal surges, due to their special non-ohmic $V-I$ characteristics¹⁻⁴. The main part of the ZnO varistors is a ceramic composite, consisting mainly of ZnO and a matrix of other metal oxides, such as bismuth (Bi), cobalt (Co), manganese (Mn), chromium (Cr), nickel (Ni), silicon (Si), antimony (Sb) and arrayed between two electrodes, as shown in Figure 2.1 (a). ZnO is a piezoelectric semiconducting ceramic with a wide bandgap $\sim 3.2\text{eV}$. Additives such as Bi_2O_3 will melt and form a thin insulating layer between ZnO grains when sintered above 1000°C . Then a back-to-back Schottky barrier (also called double Schottky barriers, DSBs) will form at the grain boundaries that contribute to the non-ohmic $V-I$ characteristics, which inhibits electron movement and stops the current path, as shown in Figure 2.1 (b).

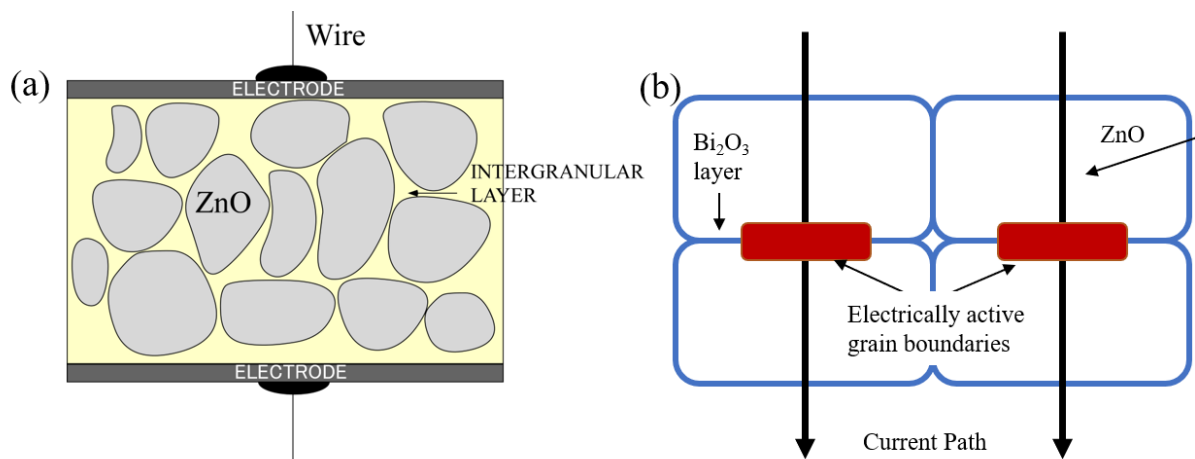


Figure 2.1 (a) The structure of a common ZnO varistor, and (b) schematic view of the electrical path of a ZnO varistor.

Figure 2.2 shows the typical V - I characteristics of a SiC varistor² and a ZnO varistor³. ZnO varistors show a very high nonlinearity compared to SiC varistors; their voltage almost keeps stable while increasing current. This excellent nonlinearity allows them to have a large surge absorbability. The nonlinear index α for SiC varistors is 3~7, which of ZnO varistors varies from 20~100. The electrical properties of ZnO varistors can be easily altered by changing additives in materials and grain boundary structures. Their excellent nonlinear V - I characteristics allows ZnO varistors to be used without series gaps due to their small current at

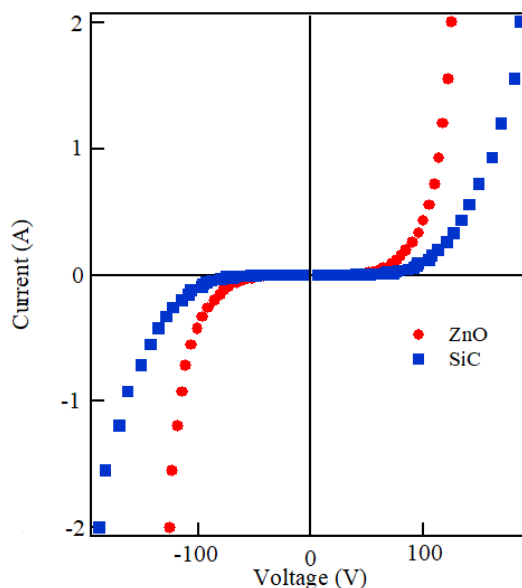


Figure 2.2 Current–voltage characteristics for ZnO and SiC varistors.

nominal voltage.

Varistors are connected in parallel to the devices, as shown in Fig. 2.3. When operating under normal conditions, a varistor is subjected to a voltage below its characteristic breakdown voltage and acts as an insulator, preventing current from flowing through it. Whenever a transient overvoltage is applied to a varistor, such as a lightning strike, the voltage exceeds the breakdown voltage and the varistor resistance will be rapidly decreased to conduct the large current and protect components.

The ZnO varistor was first developed as an arrester to protect low voltage electrical circuits from high surge voltages, as SiC varistors were unable to achieve that low voltage. It was considered that reducing the varistor units between electrodes could decrease the varistor voltage, therefore, the PN junction between the metal electrode and ZnO might be a useful way. In one abnormal experiment, samples made over 1100°C exhibited an unexpected high voltage as the Ag electrode melted on the ZnO surface, and a unique voltage–current symmetry was

obtained. The special symmetric nonlinear $V-I$ characteristics resulted from Bi and Mn diffusing into ZnO grains and forming insulator layers, which formed double Schottky barriers. DSBs increased the voltage range of the varistors, allowing them to absorb surges more effectively, which solved the gapless arrester's problem for electrical power delivery applications.

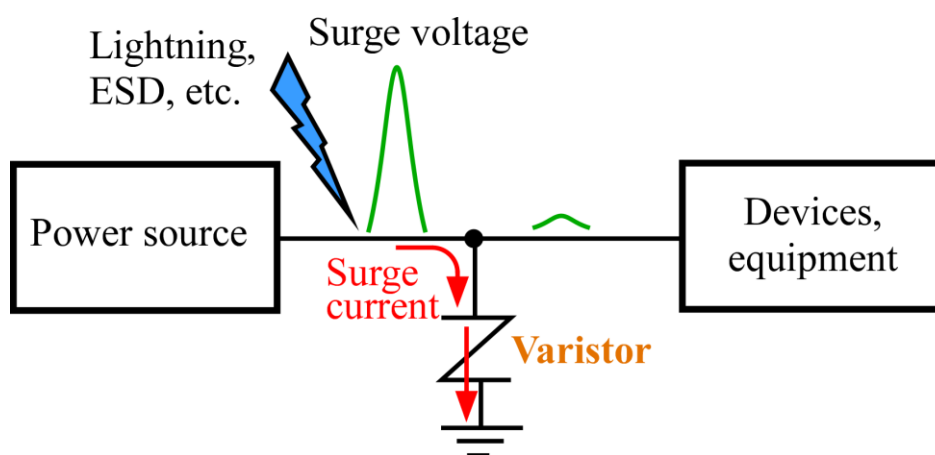


Figure 2.3 Schematic of the application of varistors to protect devices from abnormal voltage.

Now, matured electro ceramic processing technology has been fully developed for any specific recipe of ZnO varistors. The commercial method to fabricate ZnO varistors is the conventional solid-state reaction method. By adjusting the sintering temperature, time and atmosphere, the density and microstructure of the material can be controlled. A difference in additive properties will affect the secondary phases in ZnO varistors or the density of donors in ZnO grains, which results in a difference in ZnO grain conductivity and the electrical properties of ZnO varistors. ZnO varistors are determined by the behavior of the DSB junctions in series across the electrodes, so altering and studying the Schottky barriers represents an important method for improving their electrical properties.

Nowadays, ZnO varistors are widely spread and different application are developed, both for low voltage circuits protection and high voltage power transmission system³⁻⁴, such as ZnO varistor surge arresters⁵, multi-layer ZnO varistors⁶, ZnO-polymer nanocomposite micro varistors⁷.

2.2 Applications of ZnO varistors

2.2.1 ZnO varistors: types and applications

There are two types of zinc oxide varistors depending on their application: overvoltage protection or surge absorption, which are used in electrical and electronic systems in voltages that range from low voltages to ultra-high voltages⁴. The key property of both applications is nonlinearity. Electric power systems use ZnO varistor surge arresters as overvoltage protection equipment, and the insulation level of power apparatus is decided by the overvoltage protection level of surge arresters. There are a variety of ZnO varistors developed for specific uses, for example, disc-shaped varistors used for circuits and electronic devices, block-shaped varistors, rod-shaped varistors, and others. With the help of printing technology, a multi-layer chip-type ZnO varistor has been developed. To protect electrical power systems from lightning damage, ZnO varistors are used from power plants to common households. Because of the ever-increasing demand for electricity, a wide range of uses of ZnO varistors continues to arise in society and industry.

Zinc oxide varistors are used to conduct lightning strikes away from power transmission lines. During lightning strikes and transient voltages, the ZnO arresters provides a low-impedance path to ground and then returns to normal high-impedance operation as shown in Fig. 2.3. Figure 2.4 (a) shows the first ZnO varistor lightning arrester in the world. In recent years, line surge arresters have been applied to 110-500 kV AC transmission lines, and to 500 kV to 800 kV UHV DC transmission lines⁶. Figure 2.4(b) shows the structure of a polymeric type ZnO surge arrester most popularly used in electrical systems. The ZnO varistor (metal oxide varistors, MOV) bulks are connected in series, and they are covered with porcelain housing to keep surface insulated. Since the working voltage of arresters is determined by the MOV blocks, a device which has more MOV blocks will have a higher working voltage. This means to protect higher voltage power transmission lines, the surge arresters have to be very large. Furthermore, by installing these polymeric line surge arresters, the lightning protection of transmission lines has been greatly improved.

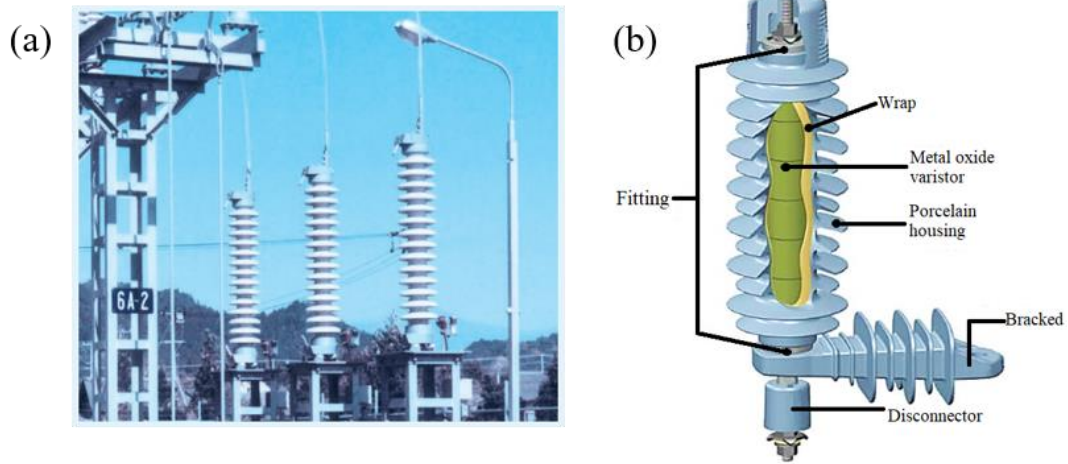


Figure 2.4 (a) first ZnO varistor lightning arresters in the world, 66kV electric transmission line⁵, (b) Polymeric type ZnO surge arrester.

Figure 2.5 shows two typical types of ZnO surge arresters for electronic circuits. Fig. 2.5 (a) is the schematic for multi-layer ZnO varistors (MLVs). This device is designed by pressing electrodes and ZnO varistor layer-by-layer, so the number of grain boundaries between the electrodes are reduced and the response speed is increased. MLVs are designed for low voltage circuits. Because of the limit of increasing the ZnO grain size, the reducing of the varistor voltage reaches the limit in bulk ZnO varistors. Some MLVs are also capable of acting as noise filters. Fig. 2.5 (b) is the leaded disc-shape surge arresters, the ZnO varistors are packaged by epoxy resin to ensure the insulating ability⁷.

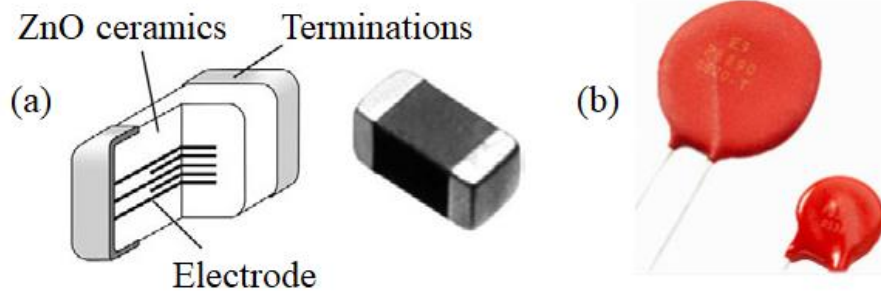


Figure 2.5 ZnO varistor types for electronic usage, (a) multi-layer ZnO varistors, (b) epoxy resin coated ZnO varistors.

2.2.2 High voltage varistors for UHV applications



Figure 2.6 Over ultra-high voltage power line in China. (China dialogue)

Consumption and demand of power keep rising with the rapid development of the economy. In order to protect the environment and reduce CO₂ emissions, clean energy is becoming increasingly important. For a diverse electrical power grid, it is important and urgent to build a network that is efficient in combining fuel energy, solar energy, wind energy, hydroelectric energy, and other types. Energy loss occurs during the transmission process. Thus, in order to realize safe, efficient, clean, and low carbon electricity supply, the development of ultrahigh voltage power transmission technologies is required⁸. Using UHV power transmission to provide power, the next-generation system will have the advantages of long distances, high capacity and efficiency. Lightning damage reduction is a key challenge for next-generation UHV power transmission to withstand such high voltages. Higher voltage lightning arresters, such as ZnO varistors, play a key role in increasing the transmission line voltage. In Figure 2.6, it is shown that the arresters used for UHV power lines are very large. High voltage ZnO varistor materials are gaining interest because they will reduce arrester size while retaining protection ability. The varistor voltage is determined by the product of the voltage per grain boundary and the number of grain boundaries between the electrodes. In order to increase the varistor voltage, there are usually two approaches, one is to decrease the ZnO grain size, the other is to increase the single boundary varistor voltage. Both of them can be achieved by adjusting the experimental method and the recipe of materials, especially those that adjust double Schottky barriers.

References:

1. K. Mukae, K. Tsuda, Effects of interface states on applied voltage dependence of double schottky barrier (Part I), Nippon Seramikkusu Kyokai Gakujutsu Ronbunshi/Journal Ceram. Soc. Japan. 101 (1993) 1125–1130.
2. F.R. Stansel, The characteristics and some applications of varistors. Proc. I.R.E. 39 (1951) 342–358.
3. J. Li, S. Li, P. Cheng, M.A. Alim, Advances in ZnO–Bi₂O₃ based varistors, J. Mater. Sci. Mater. Electron. 26 (2015) 4782–4809.
4. 松岡道雄, 細川武, 沖中秀行, 江田和生, 酸化亜鉛バリスタ: 日本が生んだ世界的発明, オーム社, (2009).
5. 電力用酸化亜鉛形 ギャップレス避雷器(MOSA)の歩み明電時報 通巻 346 号 (2015).
6. E. Ag, Multilayer Varistors for Automotive, (2014) 1–34.
7. Zhao, X., Guo, J., Wang, K., Herisson De Beauvoir, T., Li, B. and Randall, C.A., Introducing a ZnO–PTFE (Polymer) Nanocomposite Varistor via the Cold Sintering Process. Adv. Eng. Mater., 20 (2018)1700902.
8. Shu, Y., Development and execution of UHV power transmission in China, Electric Power, , 38 (2005)17. (in Chinese)

Chapter 3

Principles of ZnO varistors

3.1 Electrical properties and typical parameters

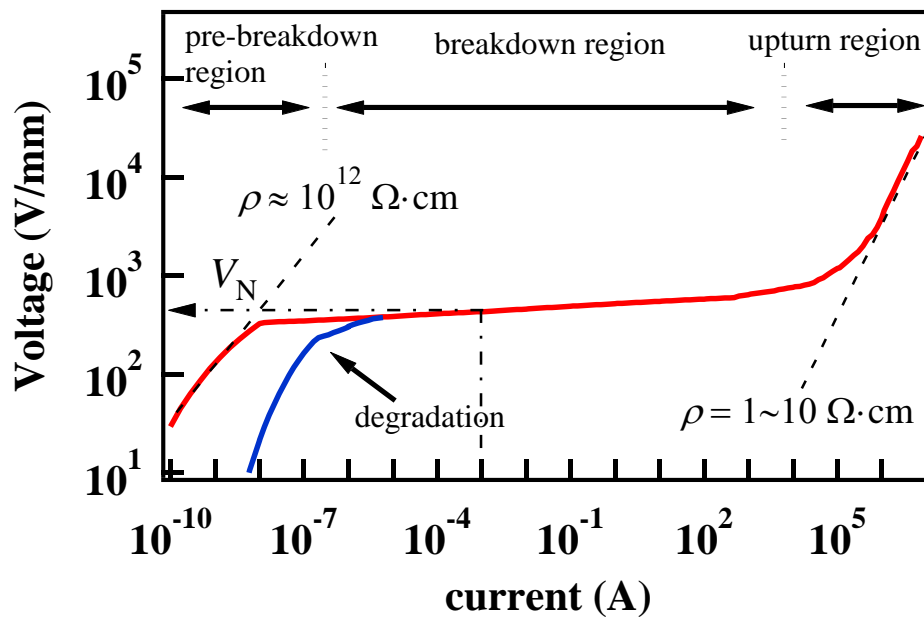


Figure 3.1 Typical $V-I$ characteristic curve of a ZnO varistor ¹.

A typical $V-I$ characteristic curve of a ZnO varistor is showed in Fig. 3.1. The three regions were distinguished by voltage-dependent switching properties, i.e., the pre-breakdown region, breakdown region and upturn region. The resistance of varistors is very large in the pre-breakdown region like an insulator. In both pre-breakdown region and upturn region, the $V-I$ characteristics are linear. In the breakdown region, the voltage of varistors is almost steady and the resistance changes with increasing the current, that results in a nonlinear $V-I$ characteristic. The sharp transient happened above breakdown voltage V_N , in the upturn region, when the varistor becomes highly conductive and passes a large current through it. In normal operating condition, the applied voltage is under the V_N and the varistor exhibits insulating property that can also stabilize the voltage on connected devices.

Commonly, the voltage–current is described by empirical relation:

$$I = (kV)^\alpha \quad (2.1)$$

V , I , and k are voltage, current and a constant, α is the nonlinear index, which is equal to

$$\alpha = \frac{\log I_2 - \log I_1}{\log V_2 - \log V_1} = \frac{\log (I_2/I_1)}{\log (V_2/V_1)} \quad (2.2)$$

V_1 , V_2 are voltage, I_1 , I_2 are current. Ohm resistor usually shows $\alpha = 1$. For a varistor, the larger the value of α , the better nonlinearity obtains. It is commonly decided that the voltage per 1mm thickness at current density $J = 1 \text{ mA/cm}^2$ is the varistor voltage (or breakdown voltage), V_N (V/mm). When varistors are connected to devices in parallel, current flows through the protected devices in normal working condition because of the high resistance of varistor in pre-breakdown region. If the abnormal surge attacks the circuit and over-voltage occurs between varistor, the resistance of varistor falls rapidly and varistors direct the current to the ground to protect devices.

3.2 Microstructure and electro ceramic processes

Figure 3.2 shows the crystal structure of wurtzite ZnO. ZnO has a wurtzite crystal structure

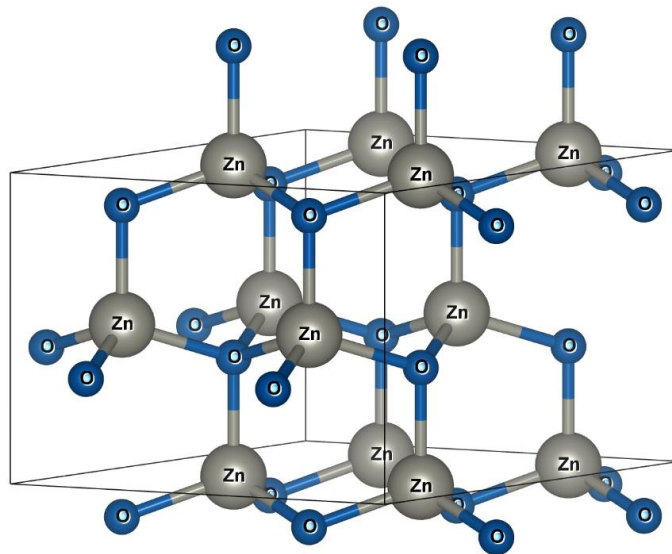


Figure 3.2 Crystal structure of ZnO (wurtzite).

with polar surfaces, with stable lattice parameters $a = 0.325 \text{ nm}$ and $c = 0.5204 \text{ nm}$ (hexagonal crystal system, P63mc space group). It is a wide band gap II-IV semiconductor, which band gap is around 3.2eV. The native defects such as oxygen vacancy or zinc interstitials make ZnO is a n-type semiconductor.

The electrical properties of ZnO varistors are completely controlled by the ceramic microstructure and the electrically active grain boundaries between two semiconducting ZnO grains. The double Schottky barriers formed at intergranular layer and ZnO grains contribute

to their nonlinear $V-I$ characteristics. The formation of liquid phase Bi_2O_3 and the chemical reaction between ZnO and additives during sintering determine the final crystal phase and microstructure of ZnO varistors. Furthermore, the non-ohmic characteristics and operation life properties are influenced by the Bi_2O_3 phase and thermal treatment temperature. The triple-point structure also affects the electrical properties.

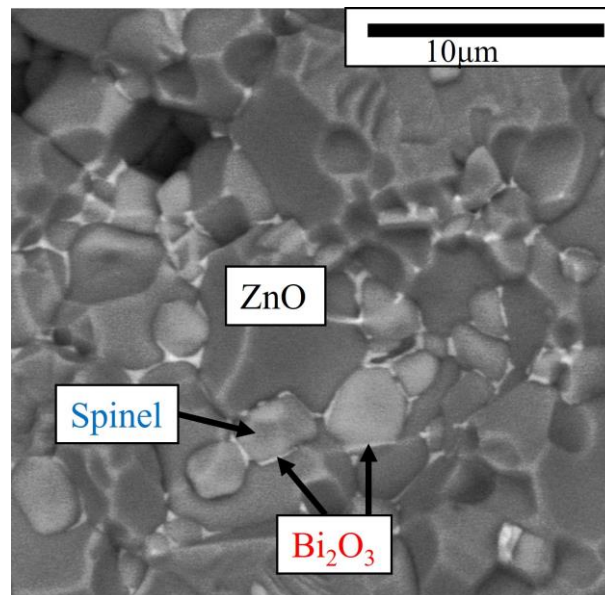


Figure 3.3 The microstructure of the typical Bi-based ZnO varistor is shown in the BSE image. The dark grey color grain is ZnO , the light grey grain is spinel particles, and the white layer at grain boundaries and triple-points is Bi_2O_3 .

3.2.1 Microstructure

The microstructure of a typical ZnO varistor, doped with 0.6 mol% Bi_2O_3 , 0.55 mol% MnO_2 , 0.63 mol% Co_3O_4 , 2 mol% Sb_2O_3 , 0.35 mol% Cr_2O_3 , 0.6 mol% NiO , (similar as commercial ZnO varistors) is discussed. The Backscattering Electron (BSE) image of sintered sample is shown in Fig. 3.3. ZnO grains are surrounded by Bi_2O_3 which is a few hundred nanometers in size; small $\text{Zn}_7\text{Sb}_2\text{O}_{12}$ spinel particles are generated at grain boundaries. In contrast, other additives dissolve in materials and do not form new compounds. The Energy Dispersive X-ray Spectrometer (EDS) can be used to determine element location. Most of Cr, Ni, Mn, and Co are found in spinel particles, small amount of Co and Mn are present in both the ZnO and intergranular layers, while Cr and Ni are found mainly in spinel particles, then grain boundaries and ZnO grains.

3.2.2 Chemical reaction mechanisms during sintering

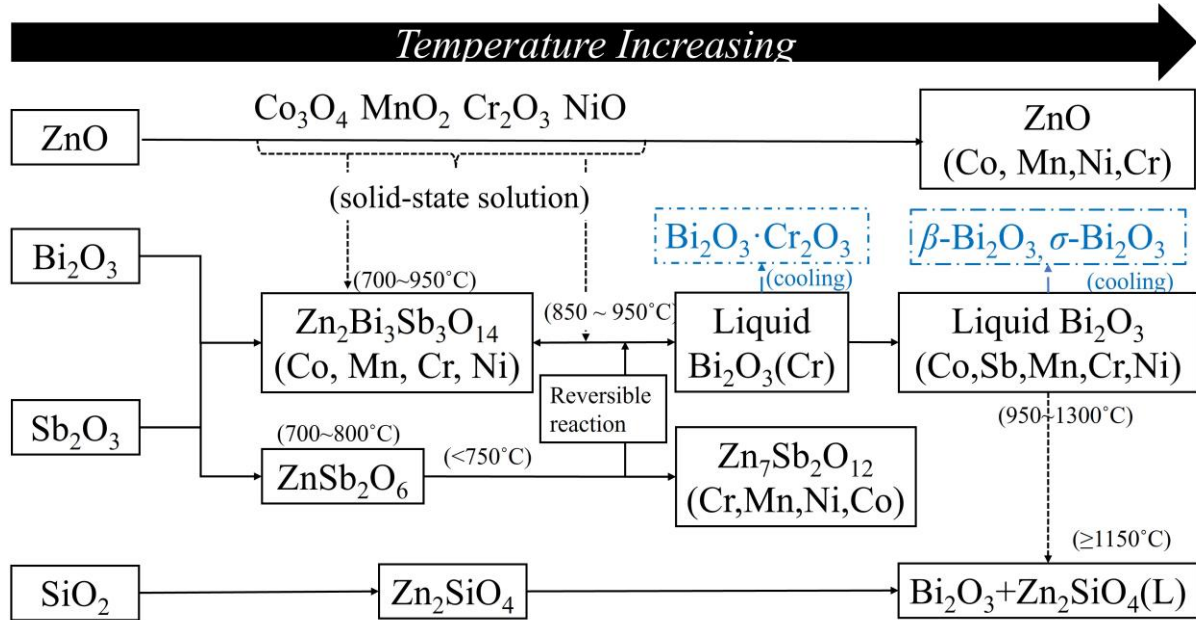


Figure 3.4 Mechanisms of reaction in Bi-based ZnO varistors with increasing sintering temperature. The solid-line is chemical reaction, the dotted-line means solid-state solution, the dashed-line indicates results after gradually cooling.

Figure 3.4 summarizes the chemical reactions that occur during sintering for Zn-Bi-Sb-Si-Co-Mn-Cr-Ni varistors^{1, 2}. The reaction between ZnO and Sb₂O₃ begins at react 700 °C, ZnSb₂O₆ is formed initially, which transfers to spinel structure Zn₇Sb₂O₁₂ with increasing temperature. Pyrochlore Zn₂Bi₃Sb₃O₁₄ is formed simultaneously by the reaction of ZnO, Bi₂O₃ and Sb₂O₃. Cr₂O₃ reacts with Bi₂O₃ below 700 °C to form Bi₂O₃·Cr₂O₃, which is absorbed by Zn₂Bi₃Sb₃O₁₄ when temperature is increased. The Zn₂Bi₃Sb₃O₁₄ divides into liquid spinel and Bi₂O₃ while increasing temperature to 850~950 °C, this is a reversible reaction. The Co, Mn, Cr, Ni ions is dissolved in ZnO and spinel particles while grain growth above 950 °C. Spinel particles and Zn₂Bi₃Sb₃O₁₄ absorb most of the impurities such as Cr from ZnO and liquid phase, converting it into Bi₂O₃. The particular structure of these secondary phases enables them to easily absorb the impurities, thus inhibiting the concentration of dissolving impurities in ZnO to maintain the semiconductive properties. It is SiO₂ reacts with ZnO that forms willemite Zn₂SiO₄, which melts into Bi₂O₃ liquid phase above 1150 °C, but separates during cooling. In cooling ZnO and spinel particles remain intact, but Bi₂O₃ will be affected by the cooling speed

and sintering temperature, which can result in the stable α , β , σ -Bi₂O₃ phase, or unstable λ -Bi₂O₃ phase. The oxygen diffusion between ZnO grain boundaries will be influenced by these phase changes, which in turn will change the nonlinear index. Electrical properties are created as a result of the dissolving donor ions impacting the double Schottky barriers. Therefore, it is common to set the sintering temperature above 1100 °C for good density and electrical properties. The sintering and pre-sintering treatment is important for ZnO varistor fabrication.

3.2.3 Additives effects on electrical properties

Table 3.1 Common additives in ZnO varistors ¹⁻⁵.

Additives	Role
Bi, Pr, Ba, Sr	Isolate ZnO grains and form DSBs
Bi, Be, Sn	Promote grain growth
Sb, Si	Inhibit grain growth
Co, Mn	Donor additives that improve the nonlinear coefficient and contributes to surface states,
Sb, Al, B, Ni, Cr	Improve stability

A summary of common additives is listed in Table 3.1. Additional additives, such as rare earth elements^{6,7}, gallium⁸, indium⁹, and so on, have been found to improve ZnO varistors' electrical properties. We will not describe those in detail here.

There are four types of Bi₂O₃ changing with sintering temperature as discussed above ^{1,2}. The monoclinic α -Bi₂O₃ that is the most stable phase; tetragonal β -Bi₂O₃ is meta-stable phase formed at high temperature; cubic σ -Bi₂O₃ formed at high temperature is a stable phase; λ -Bi₂O₃ formed with impurities. When Bi₂O₃ melts to form a liquid phase during sintering, it dissolves a part of the dopants and distributes them uniformly across the interface. Furthermore, this liquid phase promotes dense sintering and grain growth.

Sb₂O₃ has a melting point at 656°C. It inhibits ZnO grain growth by formation of spinel particles at grain boundaries ³. Addition of Sb will improve the varistor voltage and the stability.

Co₂O₃ dissolved in ZnO to increase the donor density at interface, results in an increasement of barrier height that increase the nonlinearity and voltage ^{1,2}.

MnO₂ dissolved in secondary phases and ZnO, which improve the nonlinearity.

Cr_2O_3 mostly existed in spinel particles, partial dissolved in ZnO that acts as donor and increase the Schottky barrier height. It improves the stabilities of ZnO varistors¹⁻⁵.

NiO mostly dissolved in spinel particles and improves the stability^{4,5}.

SiO_2 increases varistor voltage by forming willemite at grain boundaries¹, which also makes grains more homogeneous. It is the balancing nature of these effects that helps to achieve a uniform distribution of ZnO grain sizes in the polycrystal. Another crucial factor for the grain growth mechanism are inversion or twin grain boundaries.

3.3 Conductive mechanisms

3.3.1 Double Schottky barriers

Zinc oxide varistor possesses special electrical properties as a result of its microstructure at grain boundaries, a thin insulating layer of Bi_2O_3 surrounds the semiconductive grains. These grains are good wide-gap semiconductors. Essentially, the electrically active part of the material resides at the grain boundaries or common interfaces between these grains. The grain boundary potential in ZnO varistors arises from the combination of the energy band structures of the two grains and the dopant species that sit along with the interface between them.

Figure 3.5 draws the double Schottky barrier structure. The band structure of the individual grain boundary is formed when these energy bands come into contact between two grains. In order to achieve thermodynamic equilibrium, electrons must flow across the interface until their Fermi levels are equal on both sides. Because the Fermi level of the grains is higher than that of the grain boundary material, electrons flow from the grains to the grain boundary. Dopant species and crystallographic defects trap them, increasing the Fermi level until it is even across the interface. It leaves behind a layer of negatively charged donor sites on either side of the grain boundary caused by trapped electrons at the grain boundary. The depletion layer is the result. An upward bending of the energy bands near the grain boundary results in an electrostatic field with a barrier at the grain boundary known as a double Schottky barrier.

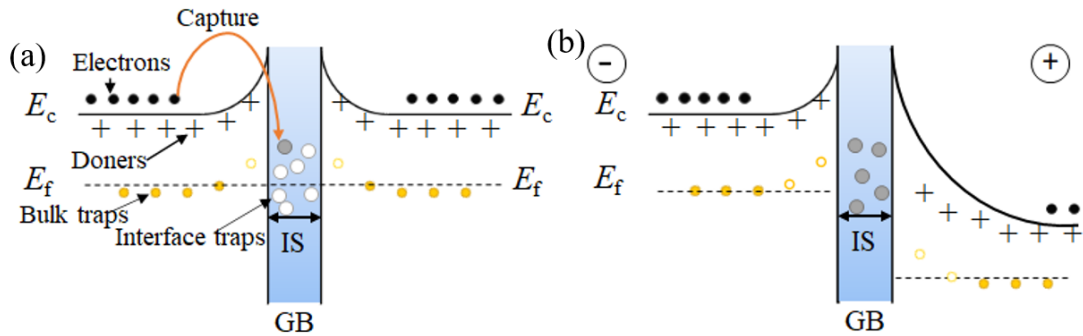


Figure 3.5 Band diagram of a single grain boundary of double Schottky barriers, (a) no bias, (b) under bias.

3.3.2 Interface states and oxygen absorption

For ZnO varistors, the interface states are very important that affect the electrical properties. Surface oxygen absorption on ZnO grains forms the interface states. Oxygen concentration plays a crucial role in Schottky barrier structures, and when it increases, donor density will increase^{1,10,11}. ZnO-based varistors require an absorbing layer of bismuth with a thickness of about 5 Å to create potential barriers at grain boundaries, and the height of these potential barriers depends on the amount of oxygen over the interface between grains¹⁰. Furthermore, transition metal oxides such as Co, Mn are primarily used as dopants to control the oxygen concentration at grain boundaries¹⁰.

The isothermal capacitance transient spectroscopy (ICTS) can be used to measure the interface state levels¹¹, described in chapter 4. The interface trap levels (derived from the interface states levels) strongly influence the recombination of electron-hole pairs. The depth and the distribution of interface states is found that influence the nonlinear index α ¹³. The electrical degradation is related to the interface traps but not the bulk traps.

The capacitance – voltage ($C-V$) method can be applied to measure the Schottky barrier height and donor density, which is also explained in chapter 4. A detailed discussion of Schottky barriers and interface states is presented in this study to understand the effect on electrical properties.

3.4 Degradation phenomena and the mechanisms

As discussed in chapter 2, ZnO varistors show excellent nonlinear voltage–current characteristics and are widely used without air gap between varistor bulks. In standby mode,

ZnO varistors are applied at voltages around breakdown voltage in the pre-breakdown region, and at leakage currents of tens to hundreds of μA . The phenomenon of electrical degradation is the increase in leakage current at the pre-breakdown region during application, as shown in Fig.3.1 the blue line. During electrical degradation, leakage current increases gradually, causing thermal heat to build up in varistors, which leads to device failure. Electrical degradation is an important problem that affects the device life and stability.

The Schottky barrier structure is also affected by electrical degradation, which reduces the varistor voltage in devices. Thermal annealing after sintering at 500-700°C improves the resistance to electrical degradation¹⁴. Different mechanisms have been discussed for centuries to explain electrical degradation^{1,14-17}. One of the most popular mechanisms is ion migration where, under applied bias, interstitial ions pass the grain boundaries, resulting in a decrease in interface states electron density as well as lowering of barrier height. Electrical degradation is also affected by the Bi_2O_3 phase states. Due to the evaporation of Bi_2O_3 , ZnO grains do not form a stable intergranular layer, and degradation occurs. Oxygen desorption on ZnO surface that distort double Schottky barriers is also one of the causes. Other mechanisms include asymmetrical distribution of impurity ions, electrons captured by interface traps, loss of oxygen species and $\beta\text{-Bi}_2\text{O}_3$ phase during degradation process and so on.

References

1. 松岡道雄, 細川武, 沖中秀行, 江田和生, 酸化亜鉛バリスタ: 日本が生んだ世界的発明, オーム社, (2009).
2. J. Li, S. Li, P. Cheng, M.A. Alim, Advances in ZnO–Bi₂O₃ based varistors, *J. Mater. Sci. Mater. Electron.* 26 (2015) 4782–4809.
3. N. Daneu, A. Rečnik, S. Bernik, Grain growth control in Sb₂O₃-doped zinc oxide, (2003).
4. H. Bai, S. Li, Y. Zhao, Z. Xu, R. Chu, J. Hao, C. Chen, H. Li, Y. Gong, G. Li, Influence of Cr₂O₃ on highly nonlinear properties and low leakage current of ZnO–Bi₂O₃ varistor ceramics, *Ceram. Int.* 42 (2016) 10547–10550.
5. T. Kato, I. Kawamata, A. Yamada, S. Ishibe, M. Kobayashi, Y. Takada, Effect of Ni and Cr on the stability of leakage current for spinel-reduced ZnO varistor ceramics, *J. Ceram. Soc. Japan.* 119 (2011) 234–237.
6. S. Bernik, S. Macek, B. Ai, Microstructural and electrical characteristics of Y₂O₃-doped ZnO–Bi₂O₃-based varistor ceramics, *J. Eur. Ceram. Soc.* 21 (2001) 1875–1878.
7. L. Ji-Le, G.H. Chen, C.L. Yuan, Microstructure and electrical properties of rare earth doped ZnO-based varistor ceramics, *Ceram. Int.* 39 (2013) 2231–2237.
8. B. wen Wang, B. hui Chen, P. zhao Gao, H. hui Chen, P. Zhang, Mechanism of Ga₂O₃ addition on the enhancement of electrical and mechanical properties of ZnO based varistor, *Ceram. Int.* 47 (2021) 4157–4165.
9. P. Meng, J. Hu, H. Zhao, J. He, High voltage gradient and low residual-voltage ZnO varistor ceramics tailored by doping with In₂O₃ and Al₂O₃, *Ceram. Int.* 42 (2016).
10. P.R. Bueno, E.R. Leite, M.M. Oliveira, M.O. Orlandi, E. Longo, Role of oxygen at the grain boundary of metal oxide varistors: A potential barrier formation mechanism, *Appl. Phys. Lett.* (2001).
11. L. Liu, Z. Mei, A. Tang, A. Azarov, A. Kuznetsov, Q.-K. Xue, X. Du, Oxygen vacancies: The origin of n-type conductivity in ZnO, *Phys. Rev. B.* 93 (2016) 235305.
12. A. Tanaka, K. Mukae, ICTS measurements of single grain boundaries in ZnO:rare-earth varistor, *J. Electroceramics.* 4 (1999) 55–59.
13. K. KUROKAWA, Y. SATO, S. YOSHIKADO, Electrical characteristics of SrCoO₃-added zinc oxide varistors, *J. Ceram. Soc. Japan.* 123 (2015) 583–588.
14. X.T. Zhao, J.Y. Li, R. Jia, S.T. Li, The Effect of DC degradation and heat-treatment on defects in ZnO varistor, *Wuli Xuebao/Acta Phys. Sin.* 62 (2013).

15. Y. Yamashita, S. Yoshikado, Evaluation of factors in the degradation of ZnO varistor, *IEEJ Trans. Power Energy*. 119 (1999) 652–657.
16. J. Lin, S. Li, J. He, L. Zhang, W. Liu, J. Li, Zinc interstitial as a universal microscopic origin for the electrical degradation of ZnO-based varistors under the combined DC and temperature condition, *J. Eur. Ceram. Soc.* 37 (2017) 3535–3540.
17. J. He, C. Cheng, J. Hu, Electrical degradation of double-Schottky barrier in ZnO varistors, *AIP Adv.* 6 (2016).

Chapter 4

Experimental procedure

4.1 Sample preparation

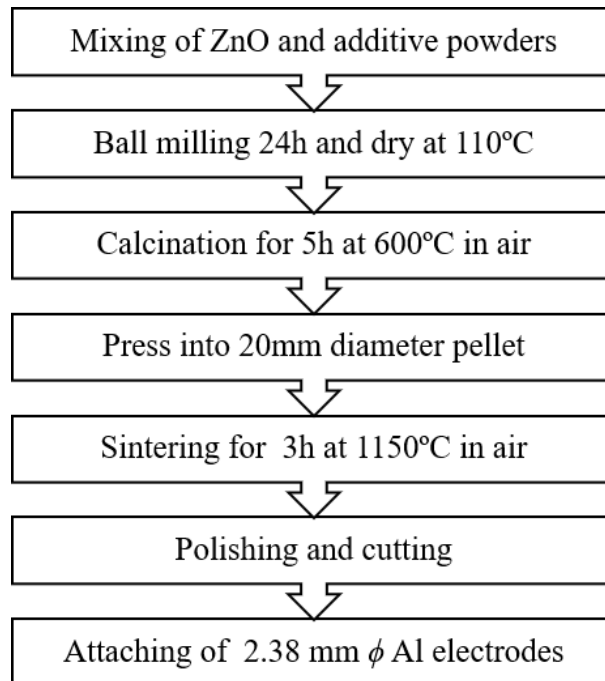


Figure 4.1 Sample preparation process flow chart.

Figure 4.1 demonstrates the flow chart of preparation process in this study. ZnO varistor samples were fabricated by solid phase sintering method with adjusting the amounts of different additives. 100mol% ZnO powder and additives powder in mole percent proportions were mixed with a total amount of 30g. The starting materials were wet-mixed by ball milling for 24 h with ethanol. Each mixture was subsequently pressed into a tablet and calcined at 600 °C for 5 h in air, after which it was ground in an agate mortar and then pressed into a 20-mm-diameter tablet at a pressure of 320 MPa. These tablets were sintered at 1150 °C for 3 h in air and then naturally cooled to room temperature. After polishing and cutting into 5 × 5 mm squares, 2.38-mm-diameter aluminum electrodes were formed on both faces of samples by vacuum evaporation.

4.2 Density determination

The density of each sintered sample was determined by the Archimedes method. The relative densities with respect to the theoretical density of wurtzite-type ZnO (5.61 g/cm^3)

4.3 Thermal Annealing treatment

Thermal annealing¹ is a useful method to reduce the defects and refine the crystal structure in ceramic materials. In this study, thermal annealing treatment was applied to some samples after sintering, by annealing at $700 \text{ }^\circ\text{C}$ in furnace for one hour in air.

4.4 Evaluation methods

4.4.1 Electrical characteristics

The V - J characteristics were determined at temperatures from 30 to $200 \text{ }^\circ\text{C}$ in air at current density J from 2.25×10^{-9} to $2.25 \times 10^{-2} \text{ A/cm}^2$ using a high-voltage measurement apparatus (237 or 2410, Keithley Instruments). Hereafter, the notation V_N - J is used, where V_N is the voltage per 1-mm sample thickness. The nonlinearity index, α , for the V - J characteristics was estimated in the breakdown region of current density from 0.1 to 1 mA/cm^2 based on the equation $V = V_K (J/J_K)^{1/\alpha}$. V_{NN} is the voltage at $J = 1 \times 10^{-3} \text{ A/cm}^2$, defined as the varistor voltage in units of V/mm in this thesis. (The units “V/mm” do not represent electric field strength.) The varistor voltage per grain boundary V_{NNGB} equals to V_{NN}/N_{GB} , where N_{GB} is the number of grain boundaries per 1 mm sample thickness. The leakage current density, J_L , was defined as the value of the current density at 80% of V_{NN} .

4.4.2 Electrical degradation

Long-term electrical degradation was evaluated from J_L -time (t) relations by applying DC voltage of 80% V_{NN} for 20 h at 130°C in air ($J_{LD130^\circ\text{C}} - t$ characteristic) to accelerate degradation and prevent the recovery of ion migration that can occur with an AC voltage, as ion migration is a major reason for degradation. Following degradation trial, samples were annealed at $200 \text{ }^\circ\text{C}$ in air for 1 h to check the recovery ability.

4.4.3 Capacitance – voltage characteristics

The nonlinearity in the V – J characteristics of ZnO varistors can be explained by a model involving the double Schottky barrier that forms at the boundaries between the ZnO grains. The electrons trapped at acceptor-type interface states at the grain boundaries are compensated by ionized donors or bulk traps near the grain boundaries. Therefore, the potential barrier within the depletion region forms a high-resistance layer in the unbiased state. Both the equilibrium height Φ_{B0} of the double Schottky barriers and the donor density N_D in ZnO grains can be determined by the C – V relationship using the following equation ²:

$$\left(\frac{1}{C_{\text{NGB}}(V_{\text{GB}})} - \frac{1}{2C_{\text{NGB}}(0)} \right)^2 = \frac{2(\Phi_{B0} + V_{\text{GB}})}{e\epsilon\epsilon_0 N_D}, \quad (4.1)$$

where $C_{\text{NGB}}(V)$ is the capacitance per grain boundary and unit area of a grain boundary when the DC bias voltage V is applied, e is the electron charge, ϵ is the relative permittivity of ZnO (≈ 8.5), ϵ_0 is the permittivity of free space ($\epsilon_0 = 8.854 \times 10^{-14}$ F/cm). Figure 4.2 shows the typical C – V characteristics measured in this study. The interface state density N_{ISO} for states at and/or below the Fermi level under zero bias voltage and the width of the depletion layer w_{DL0} under zero V are obtained by the following equations:

$$N_{\text{ISO}} = \left(\frac{2\epsilon\epsilon_0 N_D \Phi_{B0}}{e} \right)^{\frac{1}{2}}, \quad (4.2)$$

$$w_{\text{DL0}} = \left(\frac{2\epsilon\epsilon_0 \Phi_{B0}}{e N_D} \right)^{\frac{1}{2}} = \frac{N_{\text{ISO}}}{N_D}. \quad (4.3)$$

$C(V)$ was estimated from N_{GB} and the capacitance C per 1 cm^2 electrode area and 1 mm sample thickness. The capacitance was measured using a capacitance meter (Boonton 72B; signal frequency: 1 MHz, AC test bias voltage: 100 mVrms) and two digital voltmeters (34410A, Keysight Tech., USA) as digitizers applying the bias voltage using the DC offset of a pulse generator (1973, NF corp.) and power amplifier (4100, NF corp.). The maximum output voltage of the power amplifier is 250 V. The bias application time was set as 0.1–10000 s so that electrons might have sufficient time for capture by interface trap levels. This application time was determined by the transient capacitance measurement under a pulse from the Isothermal capacitance transient spectroscopy method. The measurements were performed

over the temperature range from 30 to 200 °C, and the temperature was controlled to within 0.1 °C.

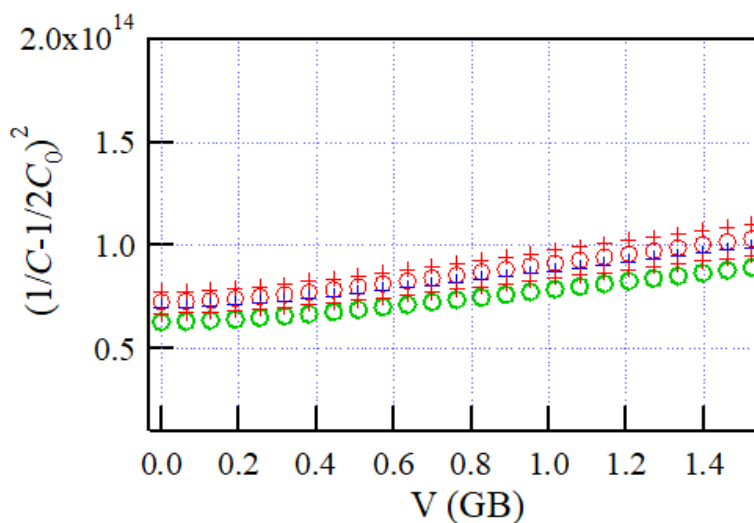


Figure 4.2 The typical C - V characteristics of ZnO varistors.

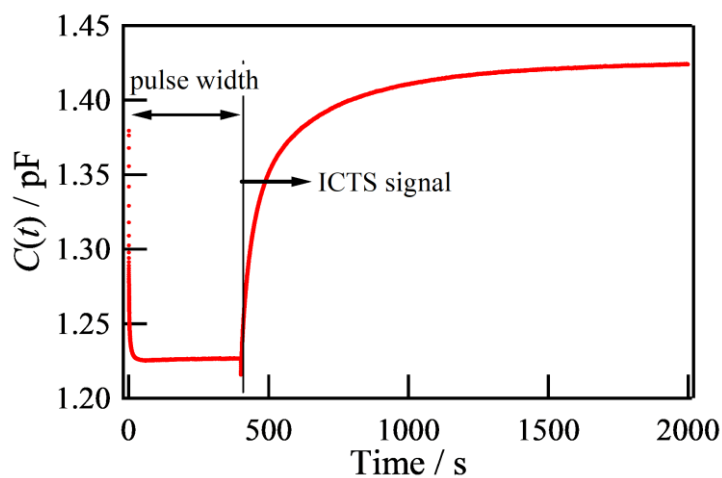


Figure 4.3 ICTS signal for ZnO varistors.

4.4.4 Isothermal capacitance transient spectroscopy (ICTS)

Because the electrical properties of ZnO varistors are predominantly determined by the trap levels (interface traps and bulk traps), Isothermal capacitance transient spectroscopy (ICTS) is a powerful tool for obtaining information on interface trap levels³⁻⁶. The time constant τ for electron capture or emission is obtained based on the transient capacitance $C(t)$ - t characteristics

after the application or removal of a pulsed voltage at constant temperature. Figure 4.3 shows the $C(t) - t$ characteristics from ICTS measurement. In order to ensure that electrons are fully captured by interface traps, the applied pulse width should be long enough until the capacitance becomes steady, as shown in Figure. This time is also used in $C-V$ measurement.

The time constant τ_{0i} for electron emission from the i -th ($i=1, 2, \dots, s$) level can be derived by^{3,5}

$$\tau_0 T^2 = B_i \exp\left(\frac{E_C - E_{ISi}}{k_B T}\right), \quad B_i = \frac{h^3 g}{4\sqrt{6}\pi^2 k_B^2 m_e^* \sigma_i}, \quad (4.4)$$

where E_{ISi} is the i -th interface state level and E_C is the bottom edge of the conduction band. k_B is the Boltzmann constant, T is the absolute temperature, m_e^* is the effective mass of an electron in ZnO ($m_e^* = 0.27m_e$; m_e : rest mass of an electron), σ_i is the capture cross-sectional area for the i -th interface state level, h is Planck's constant, and g is the degeneracy of the trap levels ($g = 1$). The transient capacitance $C_{NGB}(t)$ after removing a pulsed bias voltage V_{PHGB} is given by^{3,5}

$$\frac{1}{C_{NGB}(t)} = \frac{1}{C_{NGB0}} + \sum_{i=1}^s \frac{1}{C_{NGBi}(t)} \quad (4.5)$$

and

$$\frac{1}{C_{NGB0}} = \frac{N_{IS0}}{\varepsilon N_D}, \quad (4.6)$$

$$\frac{1}{C_{NGBi}(t)} = \frac{Q_{ISi}}{\varepsilon \varepsilon N_D} \exp\left[-\left(\frac{t}{\tau_{0i}}\right)^{\beta_i}\right] = \frac{N_{ISi}}{\varepsilon N_D} \exp\left[-\left(\frac{t}{\tau_{0i}}\right)^{\beta_i}\right], \quad (4.7)$$

where N_{ISi} is the density of electrons captured under V_{PHGB} at the i -th interface state level, τ_{0i} is the specific time constant at T for the emission process from the i -th interface state level, β_i ($0 \leq \beta_i \leq 1$) is the distribution parameter for τ_i caused by the distribution of interface state levels, and $\beta_i = 1$, as the interface state level has no distribution (δ -function like).

Since emission of electrons from bulk traps was not observed during the application of V , and the emission response of electrons is slower than that for capture, and the measurement temperature is 100 °C or higher, the measured ICTS signal could be used to assign the interface state levels. By calculating the values for each interface state level obtained by curve fitting using Eqs. 4.5 – 4.7, the existence of the interface state levels showed excellent agreement with the measured values. The interface state levels change with different additive materials. $E_C - E_{ISi}$, and σ_i were estimated from the slope of Arrhenius plots of $\tau_i T^2$ shown in Eq. 4.4.

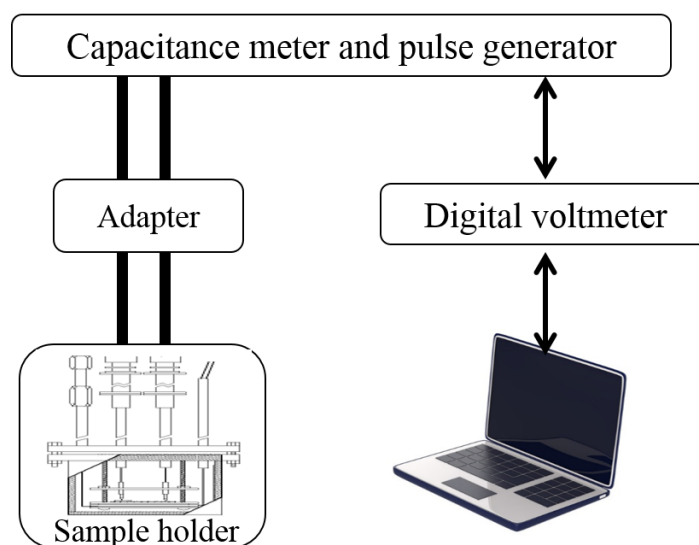


Figure 4.4 The schematic image for set up of ICTS measurement.

The equipment set-up image of ICTS measurement is shown in Fig.4.4. In order to inject electrons into interface state levels, a pulse bias V_{PHGB} was applied to the interface, and the time transient of the capacitance after removing the bias was measured. The pulse application time width was set to 0.1–400 s (depends on the additives and temperature) so that electrons might have sufficient time for capture by interface trap levels. The capacitance was measured using a capacitance meter (72B), pulse generator (1973, Leading and trailing edges of a pulse to prevent overshoot: 1 ms), power amplifier, and a digital voltmeter (34410A and 34411A). The pulse bias height V_{PHGB} was adjusted so that voltages of 0.5, 1, and 1.5 V were applied to a single grain boundary. The measurement time range was 2×10^{-4} –20000 s (this time will be changed by additives, as the response time change with additives). The measurements were performed over the temperature range from 100 to 200 °C, and the temperature was controlled to within 0.1°C.

4.5 Microstructure observation methods

4.5.1 Crystallographic evaluation with X-Ray diffraction

Phase formation in specimens was examined by X-ray diffraction (XRD). A set of atomic planes with indices $(h k l)$ with a distance between each plane of d_{hkl} . Atoms located on a plane act as sources of scattering. The X-ray beam will be scattered in all directions however it is

easier to consider only beam 1 and beam 2 whereby the beam is scattered at the same angle as the incident beam.

$$n\lambda = 2d \sin \theta , \quad (4.8)$$

The crystal structure was analyzed by X-ray diffraction (XRD; Cu $K_{\alpha 1}$, X'Pert, PANALYTICAL, the Netherlands). The relative integrated intensity was calculated by the equation followed:

$$S = \frac{\sum I_{\alpha} + \sum I_{\beta} + \dots + \sum I_{\omega}}{\sum I_i + \sum I_j + \dots + \sum I_m} \quad (4.9)$$

The lattice constants have been calculated using the following expression for hexagonal system: ^{7,8}

$$\frac{1}{d^2} = \frac{4}{3} \left(\frac{h^2 + hk + k^2}{a^2} \right) + \frac{l^2}{c^2} . \quad (4.10)$$

4.5.2 Scanning electron microscopy

Images of fractured surfaces were acquired using scanning electron microscopy (SEM, SU8020, Hitachi). Average value of ZnO grain size S_G was calculated by taking the grain size to be equal to the side length of a square with the same area for 100–200 grains per sample. Elemental compositions of the fractured surfaces were determined by backscattered electron analysis (BSE) and energy-dispersive spectroscopy (EDS) in conjunction with SEM.

4.5.3 Transmission electron microscopy

Grain boundaries were observed using field-emission transmission electron microscopy (FETEM, JEM-2100F, JEOL Co., Ltd.) with a 200 kV acceleration voltage. Elemental mapping was carried out based on EDS (JED-2300, JEOL Co. Ltd.) in association with FETEM. As shown in Fig. 4.5, in preparation for TEM observation, samples were cut into 2.1×2.1 mm squares and polished to a thickness of 0.08–0.1 μm , after which a 10 μm dimple was produced in the sample center using a dimple grinder (Model 656, Gatan Inc.). Finally, each specimen was thinned with an argon ion beam (Model 691, Gatan Inc.) at a gun voltage of 2–5 keV and a beam angle of 4° to ensure electron transparency. A beryllium sample holder was used while acquiring images.

Chapter 4 Experimental procedure

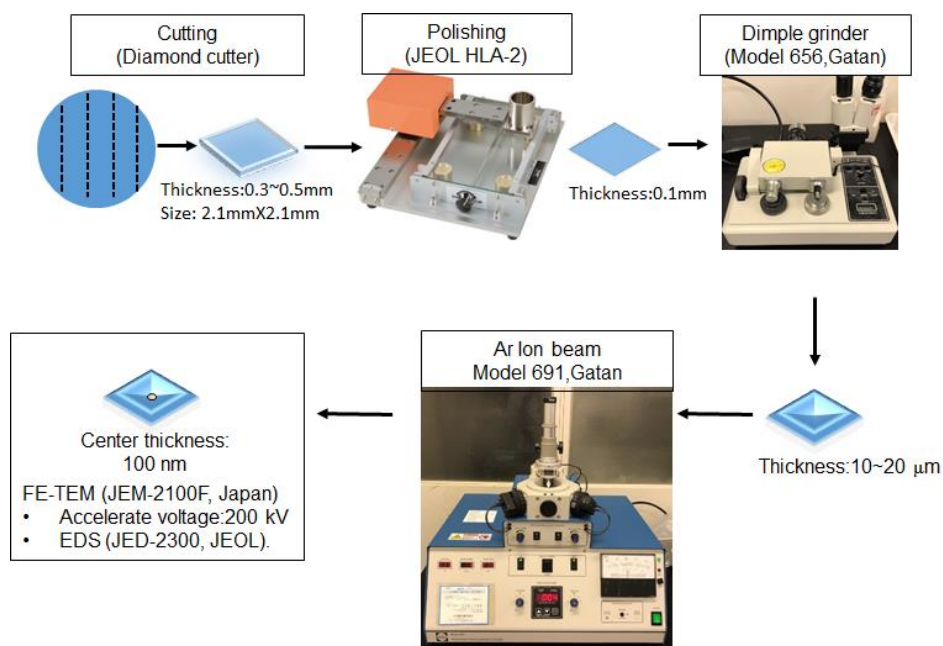


Figure 4.5 Preparation process for TEM sample.

4.5.4 Electron probe micro analyzer

The position of boron was observed using a field emission electron probe micro analyzer (EPMA, JXA 8530F Plus, JEOL Co. Ltd, Japan). Samples were dipped in melted resin in vacuum. After resin was fully diffused in samples, the surface was mirror polished for EPMA observation. In this study, the EPMA observation is consigned to the Kobelco Research Institute, Inc.

References

1. Takada M., Yoshikado S., Effect of thermal annealing on electrical degradation characteristics of Sb-Bi-Mn-Co-added ZnO varistors, *J. Eur. Ceram. Soc.* 30 (2010) 531–538.
2. Mukae K., Tsuda K., Nagasawa I., Capacitance-vs-voltage characteristics of ZnO varistors, *J. Appl. Phys.* 50 (1979) 4475–4476.
3. Kurokawa K., Sato Y., and Yoshikado S., Electrical characteristics of SrCoO₃ – added zinc oxide varistors, *J. Ceram. Soc. Jpn.*, 123 (2015) 583-588.
4. Mukae K. and Tsuda K., Effects of interface states on applied voltage dependence of double Schottky barrier (Part I), *J. Ceram. Soc. Japan*, 01 (1993) 1125-1130(in Japanese).

Chapter 4 Experimental procedure

5. Tanaka A. and Mukae K., ICTS Measurements of Single Grain Boundaries in ZnO:rare-earth Varistor, *J. Electroceram.*, (1999) 55-59.
6. Ohbuchi Y., Kawahara T., Okamoto Y., and Morimoto J., The Study of Interface States in ZnO Varistors by Injection Pulse Width Dependence of Transient Response, *Jpn. J. Appl. Phys.*, 39 (2000) 2665-2669.
7. B.D. Cullity, *Elements of X-ray Diffraction* (second ed.), Addison-Wesley, Reading, MA (1978) 102-110
8. D.S. Rickerby, A.M. Jones, B.A. Bellamy *Surf. Coat. Technol.*, 37 (1989) 111-137

Chapter 5

Effect of Cr₂O₃ and NiO on Y-doped high voltage ZnO varistors

5.1 Introduction

In 2001, Bernik et al.⁴ reported that by doping only a small amount of Y₂O₃ into Sb₂O₃ added Bi-based ZnO varistors, the varistor voltage increased obviously. The increase of voltage is because of a Y-containing phase, called Y-compound, consisting of Y, Sb, Bi, and Zn, formed at grain boundaries, that suppressed grain growth. The electrical properties of such devices are notably dependent on the amounts of both Y₂O₃ and Sb₂O₃⁵. Even so, these varistors exhibited an increase in leakage current with increasing varistor voltage, along with a substantial decrease in resistance to electrical degradation, because the precipitated phases at the grain boundaries formed by the addition of Y₂O₃ provided pathways for current flow⁶. Furthermore, the height of the Schottky barrier was changed due to an increase in the donor concentration by the dissolution of Y in the ZnO grains, which increased the migration of interstitial Zn ions.

Some researchers have attempted to reduce the leakage current of Y-doped varistors by the addition of new additives, such as indium⁷, gallium⁸, lanthanum⁹ and so on, and to understand the interaction between impurities and Y. The devices maintain the high voltage and low leakage current together have been achieved. However, there has been little progress in limiting electrical degradation. Furthermore, the open structure of Y-compounds leads to absorption of additives such as Bi, Sb, Co, Mn, Cr, Ni and others, which might change the effects of the additives and affect the overall electrical properties. It is important to investigate the correlation between resistance to electrical degradation and the distribution and crystal structure of sediments at the grain boundaries of the ZnO grains.

As is known, additives such as Cr₂O₃ and NiO (unless otherwise specified, Cr₂O₃ is written as Cr and NiO as Ni) improve the stability of Bi-based commercial ZnO varistors without the addition of Y. The addition of Cr to commercial varistors increases the varistor voltage by inhibiting ZnO grain growth and decreasing leakage current¹⁰⁻¹⁵. Kim et al.¹⁰ reported that the Schottky barrier height Φ_B became lower with increasing amounts of Cr; the donor density decreased in the depletion layer, and as a result the leakage current increased. Bai et al.¹¹ found that Cr acts as a donor and deteriorates the electrical properties at 0.2 to 0.4 mol% Cr₂O₃ due

to the formation of secondary phases, such as $\text{CrBi}_{18}\text{O}_{30}$ and $\text{Co}_2\text{Cr}_{0.5}\text{Sb}_{0.5}\text{O}_4$, but for 0.5 mol% addition the secondary phases transform into MnCr_2O_4 and Φ_B increases due to disappearance of the donor effect of Cr. Ruan et al.¹² reported that adding Cr_2O_3 and SiO_2 in an optimized ratio decreased the leakage current and improved the resistance to degradation. Xu et al.¹³ reported that the formation of Bi-Cr-O compounds when adding Cr_2O_3 to Bi-based varistors decreased the concentration of interstitial Cr^{3+} , reduced the amount of adsorbed oxygen at the grain boundaries, and raised the Schottky barrier height, and as a result the nonlinearity index of the $V-I$ relationship became larger. Kanai et al.¹⁴ reported that Cr plays a role in stabilizing $\delta\text{-Bi}_2\text{O}_3$ (a fast oxide ion conductor). Similarly, Kato et al.¹⁵ found that Ni was likely able to inhibit the absorption of Co by the spinel phase during sintering, decreasing the leakage current. Therefore, it is expected that rather than identifying new additives for Y-doped varistors, changing the amounts of Cr and/or Ni added may be effective in improving the resistance to degradation. The open crystal structure of the secondary phase Y-compound may also change the location and effect of other additives.

In this chapter, gradually increasing amounts of Cr_2O_3 or NiO were added to the basic composition of ZnO varistors (Zn, Bi, Mn, and Co) at fixed Y_2O_3 and Sb_2O_3 concentrations, and the effects of multiple dopants on the electrical properties, microstructure, interface states, and barrier parameters for Y-doped varistors were investigated in detail. In addition, samples without Y were also prepared to investigate the relationships among Y, Cr and Ni.

5.2 Utilization of Y_2O_3 and Sb_2O_3 amount

The electrical properties of Y-doped varistors were depended on the ratio of Y_2O_3 and Sb_2O_3 added. According to the former work done by Mr. Kojima¹⁶ in our lab, the dependence of Y amount and Sb amount was studied. Different amount of Y and Sb were added into Bi-Mn-Co-Cr-Ni-added ZnO (similar as a commercial ZnO varistor) varistor, and the electrical properties and microstructure were investigated. Figure 5.1 (a) shows the varistor voltage V_{NN} of samples varying the amount of Y_2O_3 and Sb_2O_3 . A clear dependence between Y_2O_3 and Sb_2O_3 amounts is demonstrated. The utilized amount of Y and Sb are 2 mol% which will receive a high varistor voltage around 1000 V/mm, it is chosen to be the basic composition in this study. It is found in Fig. 5.1(b), that samples with the utilized composition have large leakage current, as described in the introduction in this chapter. The amount of Y_2O_3 utilized, 2 mol% along with 2 mol% Sb_2O_3 .

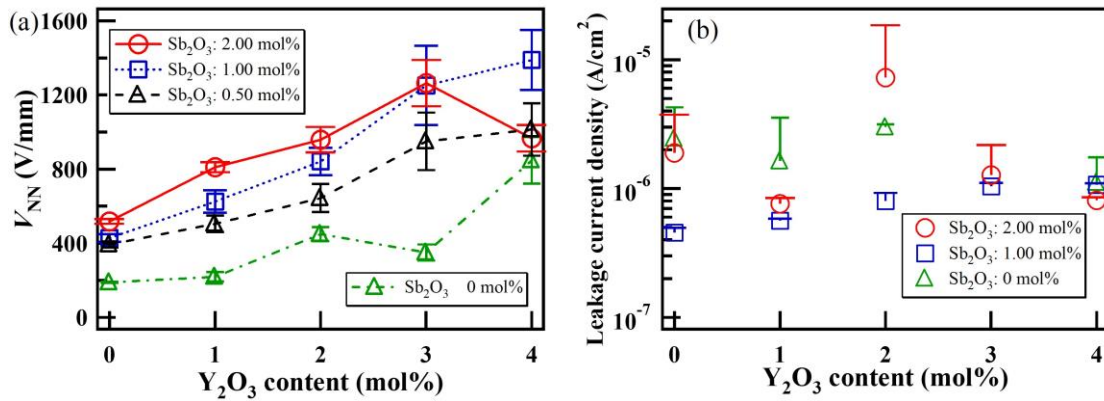


Figure 5.1 (a) Varistor voltage before electrical degradation for samples added 0-4.0 mol% Y_2O_3 and 0-2.0 mol% Sb_2O_3 . (b) Leakage current density before electrical degradation for samples added 0-4.0 mol% Y_2O_3 and 0-2.0 mol% Sb_2O_3 ¹⁶.

Table 5.1 Sample composition and additive amounts.

No.	Sample name	Sb_2O_3	Y_2O_3	Co_2O_3	NiO
1	Y2Cr0Ni0	2	2	0	0
2	Y2Cr0.175Ni0			0.175	
3	Y2Cr0.35Ni0			0.35	
4	Y2Cr0.7Ni0			0.7	
5	Y2Cr2Ni0			2	
6	Y2Cr0Ni0.3			0	0.3
7	Y2Cr0Ni0.6			0	0.6
8	Y2Cr0Ni1.2			0	1.2
9	Y2Cr0Ni4			0	4
10	Y2Cr0.35Ni0.6			0.35	0.6
11	Y0Cr0Ni0	2	0	0	0
12	Y0Cr0.35Ni0			0.35	0
13	Y0Cr0Ni0.6			0	0.6
14	Y0Cr0.35Ni0.6			0.35	0.6
15	ZBMC	0	0	0	0

5.3 Sample Preparation

ZnO varistor samples were fabricated by adjusting the amounts of Y_2O_3 (0, 2 mol%), Cr_2O_3 (0 – 2 mol%), and NiO (0 – 4 mol%) relative to those in a commercial varistor (ZnO 100 mol%, Bi_2O_3 0.6 mol%, MnO_2 0.55 mol%, Co_3O_4 0.63 mol%, Sb_2O_3 2 mol%, Cr_2O_3 0.35 mol%, NiO 0.6 mol%). Sample composition and additive amounts are listed in Table 5.1. Commonly, the

NiO amount in commercial varistors is 0.6 mol%, so here the doped amounts were half, the same, twice as much, and a high amount compared to the typical varistor recipe. Each sample is given a simplified designation herein according to its composition $Y_xCr_yNi_z$ (e.g., a sample with $x = 2$ mol% Y_2O_3 , $y = 0.35$ mol% Cr_2O_3 and $z = 0.6$ mol% NiO is referred to as $Y_2Cr_{0.35}Ni_{0.6}$). Electrical properties and microstructures were evaluated as described in chapter 4.

5.4 Microstructure and Crystal structure with Cr or Ni addition

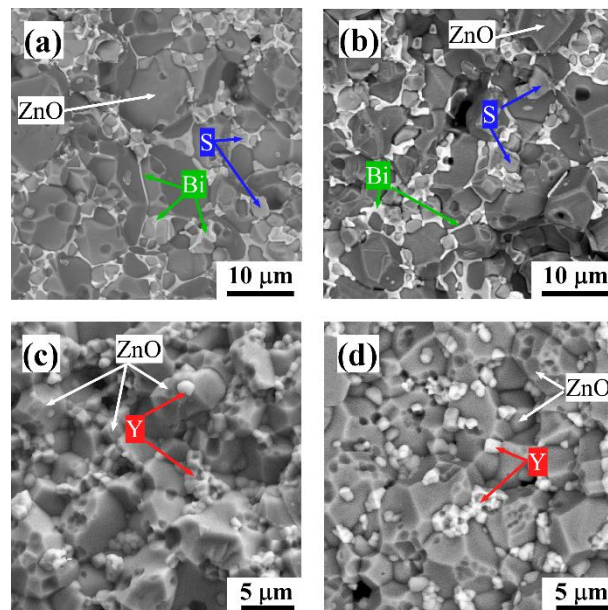


Figure 5.2 BSE images acquired by SEM of the microstructure at grain boundaries for (a) $Y_0Cr_{0.35}Ni_0$, (b) $Y_0Cr_0Ni_{0.6}$, (c) $Y_2Cr_0Ni_0$, (d) $Y_2Cr_{0.35}Ni_{0.6}$. Bi: Bi-rich layer, S: spinel, Y: Y-compound

Figure 5.2 shows the BSE images acquired by SEM of the microstructure for varistors doped with Y, Cr, Ni. The strong contrast of the BSE image revealed that the composition of the segregated particles differs from that of the ZnO particle. The elemental mapping using EDS revealed that the white color is mainly Bi and is observed at grain boundaries and triple points, the bright grey part contained large amounts of Sb is segregated spinel (S) particles, the dark grey part is ZnO. The small white segregated particles in Fig. 5.2 (c) and (d) contained Y-Sb-Bi-Zn is Y-compound, which uniformly located at grain boundaries and decreased the grain size from $6 \mu\text{m}$ to around $3 \mu\text{m}$. Different to the samples without Y, the interface between

ZnO/ZnO grains was modified in Y-doped varistors. Although a white layer mainly contained Bi was observed at grain boundaries and triple points for $Y_0Cr_YNi_z$, it disappeared, and Bi dissolved in the small white grains of Y-compound. The size and amount of spinel particles suddenly decreased due to the formation of Y-compound, which absorbed Sb. This was difficult to observe under SEM, and is instead shown in TEM images in Fig. 5.3.

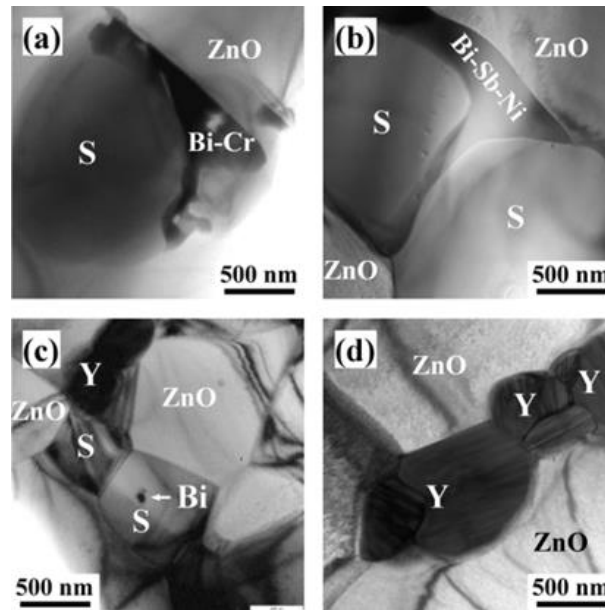


Figure 5.3 TEM images of the microstructure at grain boundaries for (a) $Y_0Cr_{0.35}Ni_0$, (b) $Y_0Cr_0Ni_{0.6}$, (c) $Y_2Cr_0Ni_0$, (d) $Y_2Cr_{0.35}Ni_{0.6}$. Y: Y-compound, S: spinel, Bi-Cr: $Bi_{16}CrO_{27}$.

The XRD patterns of the specimens with different amounts of Cr, Ni, Y are shown in Fig. 5.4. For samples without Y, the secondary phase at grain boundaries consisted of various spinels ($Zn_{2.33}Sb_{0.67}O_4$, $ZnCo_{1.33}Sb_{0.67}O_4$, and/or $Co_{2.33}Sb_{0.67}O_4$), $Zn_7Sb_2O_{12}$ ¹⁷, β - Bi_2O_3 , Co_3O_4 , and MnO_2 , and unknown diffraction peaks were observed. With the addition of Cr, the diffraction peak for $Bi_{16}CrO_{27}$ was observed, as indicated by Bi-rich (Bi-Cr) layer in Fig. 5.3 (a). $Bi_{16}CrO_{27}$ transformed to $Bi_{14}CrO_{24}$ in the $Y_0Cr_{0.35}Ni_{0.6}$ sample. The Bi layer in Fig. 5.3 (b) consisted of β - Bi_2O_3 and Sb and Ni, and the solid solution of Sb and Ni in Bi layer caused the different diffraction peaks of β - Bi_2O_3 for $Y_0Cr_0Ni_0$ and $Y_0Cr_0Ni_{0.6}$. For Y-doped samples, the main diffraction peaks were due to ZnO, Y-compound, and spinel particles, and other diffraction peaks disappeared. The disappearance of Bi-rich layer was confirmed in Fig. 5.3 (c) and (d), and a residual amount of Bi was distributed at the ZnO boundaries.

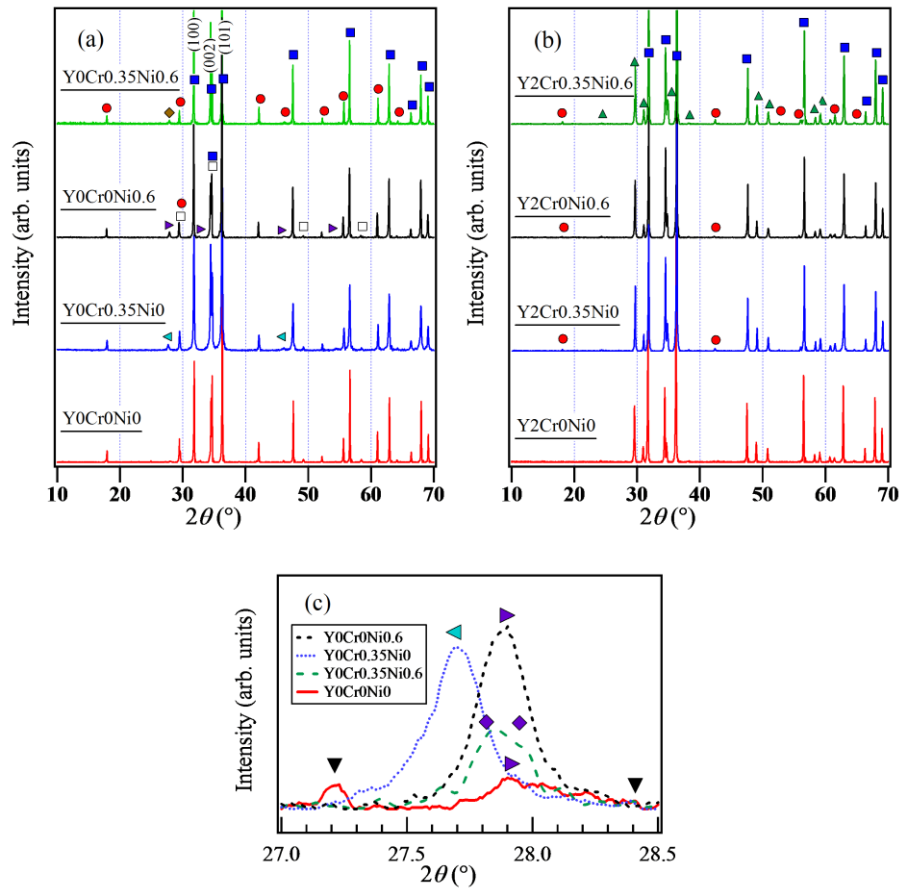


Figure 5.4 (a) XRD patterns for (a) Y0Cr0.35Ni0.6, Y0Cr0.35Ni0, Y0Cr0Ni0.6, and Y0Cr0Ni0; (b) XRD patterns for Y2Cr0.35Ni0.6, Y2Cr0.35Ni0, Y2Cr0Ni0.6, and Y2Cr0Ni0. (c) enlarged XRD pattern. ■ : ZnO, ● : spinel, ▲ : Y-compound, ▼ : Zn₇Sb₂O₁₂, ◀ : Bi₁₆CrO₂₇, ▶ : β-Bi₂O₃, □ : Zn_{0.92}Bi_{1.5}Sb_{1.5}O_{6.92}, ◆ : Bi₁₄CrO₂₄, ○ = unknown.

The microstructure did not change notably on adding Cr and/or Ni and increasing their amounts. Most of the Cr was found both in the spinel and Y-compound, while most of the Ni was mainly found in spinel, with a small amount found in the Y-compound, confirmed by EDS in Fig. 5.5. Furthermore, small amounts of both Cr and Ni were found at ZnO grains and increased with increasing additive amount, as listed in Table 5.2. The content ratios for Y, Sb, Bi, and Mn in the Y-compounds were 18–19, 14–15, 4.9–5.6, and 0.6–0.8 atom%, respectively, and were almost the same in each Y-doped sample. Since the content ratios for Y₂O₃ and Bi₂O₃ in the starting material were 2 and 0.6 mol%, respectively, and agreed with the ratios for Y and Bi in Y-compound, it was revealed that most of the Bi dissolved in the Y-compound for Y-doped samples.

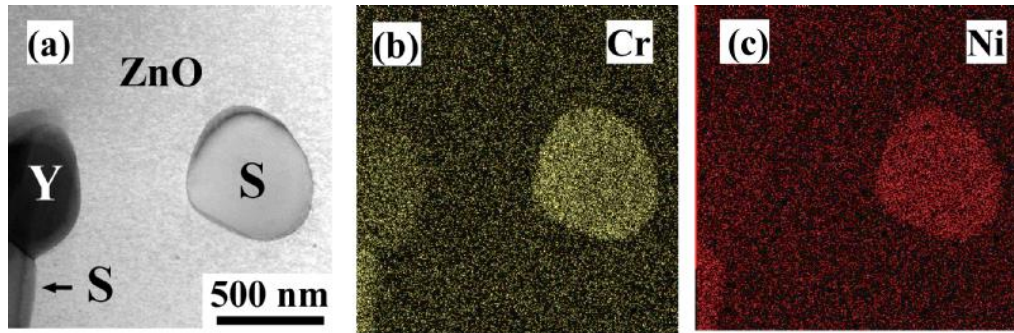


Figure 5.5 (a) TEM image and element mapping for (b) Cr and (c) Ni determined by EDS for $Y_2Cr_{0.35}Ni_{0.6}$

Table 5.2 Atomic ratio of various elements in ZnO grains to Zn (100.00 atom%) analyzed by TEM for each sample.

Composition	Element (Characteristic X-ray) (atom%)							
	Zn (K)	Cr (K)	Mn (K)	Co (K)	Ni (K)	Y (L)	Sb (L)	Bi (M)
$Y_2Cr_0Ni_0$	100.00	-	0.27	1.70	-	0.24	0.40	0.14
$Y_2Cr_{0.35}Ni_0$	100.00	0.13	0.38	1.64	-	0.01	0.15	0.01
$Y_2Cr_{0.7}Ni_0$	100.00	0.21	0.35	1.58	-	0.00	-	0.04
$Y_2Cr_0Ni_{0.3}$	100.00	-	0.42	1.85	0.50	-	0.04	0.04
$Y_2Cr_0Ni_{0.6}$	100.00	-	0.28	1.61	0.75	0.47	0.15	0.00
$Y_2Cr_0Ni_{1.2}$	100.00	-	0.24	1.67	1.12	-	0.16	0.05
$Y_2Cr_{0.35}Ni_{0.6}$	100.00	0.22	0.26	1.76	0.60	0.49	0.15	-

5.5 Electrical properties

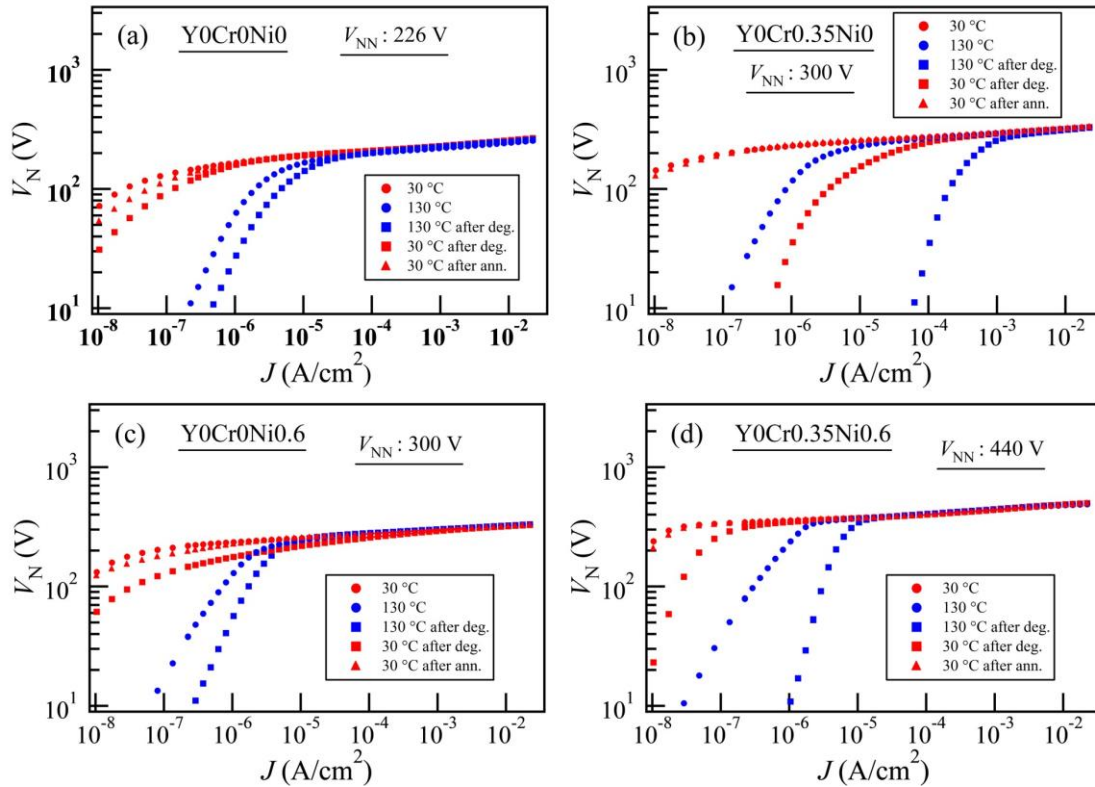


Figure 5.6 V_N - J relationships at 30 and 130 °C before and after electrical degradation and after thermal annealing at 200 °C for (a) Y0Cr0Ni0, (b) Y0Cr0.35Ni0, (c) Y0Cr0Ni0.6 and (d) Y0Cr0.35Ni0.6.

The V_N - J characteristics adding Cr and/or Ni for samples without Y are presented in Fig. 5.6, and that of Y-doped varistors are shown in Fig. 5.7. It can be observed that the pre-breakdown region of the V_N - J relationship at both 30 and 130 °C notably shifted to larger current density after degradation for Y2Cr0Ni0, as shown in Fig. 5.7 (a). However, the V_N - J curves remained stable when adding Cr or Ni, as shown in Fig. 5.7 (b), (c). It was found that the addition of Cr or Ni improved the resistance to electrical degradation for Y-doped samples. Electrical degradation refers to the deterioration of nonlinearity in the V_N - J relationship and the increase of leakage current. However, this improvement of electrical degradation by adding Cr or Ni was not found in samples without Y in Fig. 5.5. In addition, even the leakage current was decreased when Cr and Ni added to together, little improvement on degradation was observed in Fig. 5.7(d).

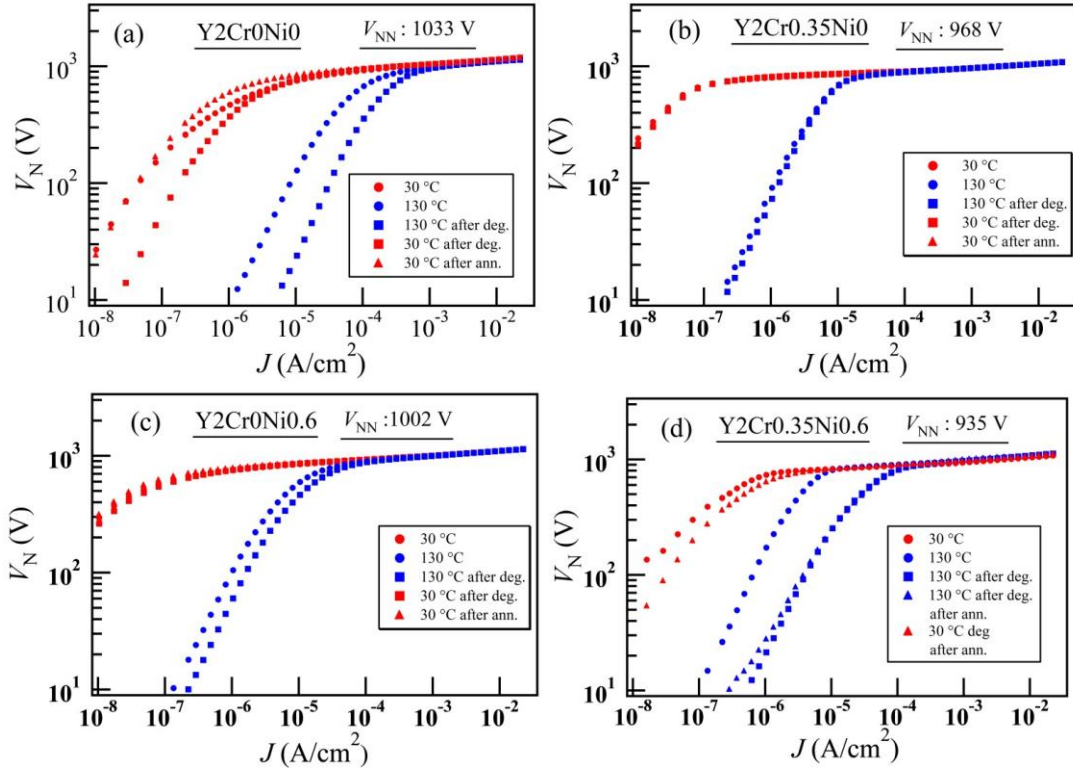


Figure 5.7 V_N - J relationships at 30 and 130 °C before and after electrical degradation and after thermal annealing at 200 °C for (a) Y2Cr0Ni0, (b) Y2Cr0.35Ni0, (c) Y2Cr0Ni0.6 and (d) Y2Cr0.35Ni0.6.

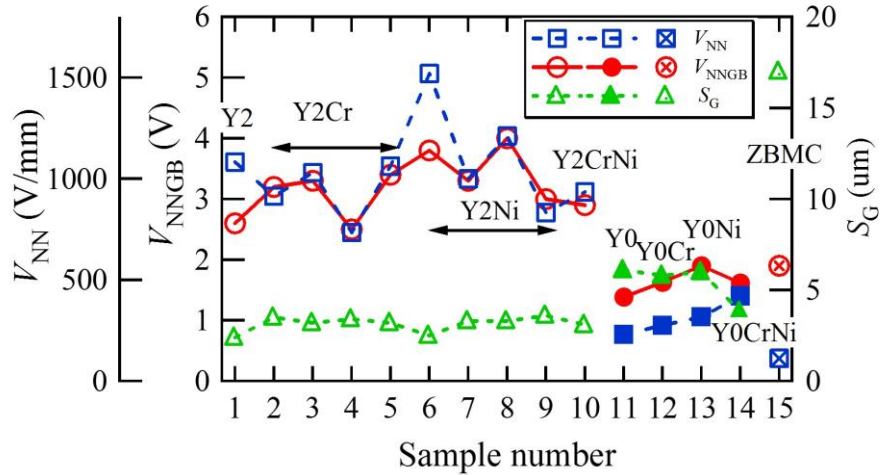


Figure 5.8 Values of V_{NN} , V_{NNGN} , and S_G for each sample.

Measured values for the varistor voltage V_{NN} , single grain boundary voltage V_{NNGN} , and grain size S_G of ZnO grains for all the samples are displayed in Fig. 5.8. The addition of Cr and/or Ni increased the V_{NN} for the samples without Y. The V_{NNGB} increased from 1.4 to 1.9 V on adding Ni to Y0Cr0Ni0 and from 1.4 to 1.6 V on adding Cr. The leakage current just after

the electrical degradation increased by a factor of ≈ 38 with addition of Cr. On the other hand, for Y0Cr0.35Ni0.6 with both Cr and Ni added, the V_{NNGB} decreased to 1.6 eV, the same as that for Y0Cr0.35Ni0. Since the S_G also decreased, the V_{NN} was the largest among the four samples. The above results suggest that the effects of the addition of Cr and/or Ni on the electrical properties are different in each case and depend on the amount. Furthermore, the resistance to degradation was not increased in these samples.

For Y-doped samples, the effects of both Cr and/or Ni on electrical properties differ from samples without Y. The S_G increased slightly on adding Cr and Ni, from 2.4 to 3.5 μm , and remained nearly constant around 3.5 μm with increasing amounts of Cr and Ni. As a result, V_{NN} increased in proportion to V_{NNGB} as well. The V_{NNGB} increased from 2.6 to 3.3 V on adding Cr_2O_3 up to 0.35 mol% (sample nos. 1, 2, and 3), then decreased to 2.5 V at 0.7 mol% (no. 4) and increased again to 3.4 V at 2 mol% (no. 5). The V_{NNGB} increased from 2.6 to 4.0 V after adding Ni in the range from 0 to 1.2 mol% (nos. 1, 6, 7, and 8) and decreased to 3.0 V at 4.0 mol% (no. 9). Figure 5.9 (a) shows the nonlinearity index α_{as} before degradation and the ratio of the nonlinearity index α_{deg} after degradation to α_{as} , $\alpha_{\text{deg}}/\alpha_{\text{as}}$. Figure 5.9 (b) shows the leakage current density before degradation $J_{\text{L } 30^\circ\text{Cas}}$ and the ratio after degradation $J_{\text{L } 30^\circ\text{Cdeg}}$ to the leakage current density before degradation $J_{\text{L } 30^\circ\text{Cas}}$, $J_{\text{L } 30^\circ\text{Cdeg}}/J_{\text{L } 30^\circ\text{Cas}}$. The value of α_{as} increased from 21 to 35 on adding Cr_2O_3 from 0 to 0.35 mol%, then remained around 32 at 0.7 and 2 mol% Cr. The $\alpha_{\text{deg}}/\alpha_{\text{as}}$ ratio was maintained around 1.0 on adding Cr_2O_3 from 0 to 0.7 mol%. This indicated that nonlinearity did not change after degradation. The value of α_{as} increased from 21 to 36 on adding NiO from 0 to 2 mol%. $J_{\text{L } 30^\circ\text{Cas}}$ decreased from 1.8×10^{-5} to around $4.8 \times 10^{-7} \text{ A/cm}^2$ after adding Cr and/or Ni to Y2Cr0Ni0. Furthermore, on adding Cr_2O_3 at 0.35 or Ni at 0.6 mol%, the ratio $J_{\text{L } 30^\circ\text{Cdeg}}/J_{\text{L } 30^\circ\text{Cas}}$ fell to 1; as a result, the resistance to degradation was notably improved. In particular, Y2Cr0.35Ni0 showed very high resistance to degradation, and the $V_{\text{N}} - J$ relationship was not changed from before to after degradation as shown in Fig. 5.6 (b). After adding Cr_2O_3 at 2.0 or Ni at 1.2 and 4.0 mol%, the $\alpha_{\text{deg}}/\alpha_{\text{as}}$ ratio decreased to less than 1 and the $J_{\text{L } 30^\circ\text{Cdeg}}/J_{\text{L } 30^\circ\text{Cas}}$ became much larger, and notable degradation was observed. This might be due to excess Cr or Ni leading to the formation of spinels containing Cr or Ni (according to XRD patterns in Fig. 5.10), causing degradation and decreasing V_{NNGB} , similar to the results with Y0Cr_yNi_z samples.

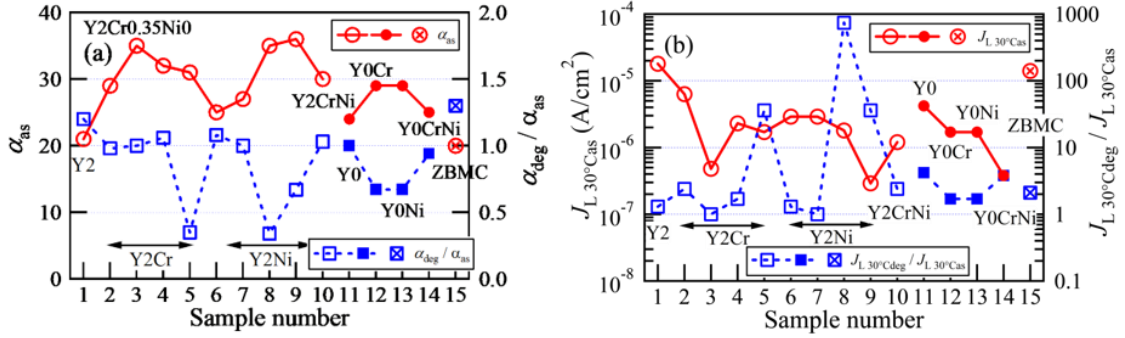


Figure 5.9 (a) α_{as} and ratio of α_{deg} to α_{as} for each sample at 30 °C. (b) $J_{L,30^\circ C,Cas}$ and ratio of $J_{L,30^\circ C,deg}$ to $J_{L,30^\circ C,Cas}$ for each sample.

Figure 5.10 shows XRD patterns for Y2CryNiz samples. The main peaks due to ZnO, spinel, and Y-compound for each sample are the same as those shown in Fig. 5.4(b). ZnCr₂O₄ and spinel peaks appeared with the addition of 0.7 mol% Cr₂O₃ and further increased with 2 mol% Cr₂O₃. The ZnNi_{1.33}Sb_{0.67}O₄ spinel structure and Zn_{0.3}Ni_{0.7}O appeared on adding 2 mol% NiO. The structural and electrical characteristics of ZnO varistors vary according to the chemical composition of the spinels in the samples¹⁸. Consequently, the formation of Y-compound decreased both the amount and the size of spinel particles and reduced the amount of Cr or Ni incorporated in the spinels, so the effects of Cr or Ni on the improvement of electrical degradation were apparent.

For electrical properties, the optimum amount of Cr₂O₃ was found to be 0.35 mol%, with V_{NN} of ≈ 1030 V, both α_{as} and α_{deg} of 35, low leakage current at 4.8×10^{-7} A/cm², and high resistance to electrical degradation. The highest V_{NN} , achieved by adding 0.3 mol% NiO, was 1520 V. In this case the leakage current density was 2.9×10^{-6} A/cm² and both α_{as} and α_{deg} were 25.

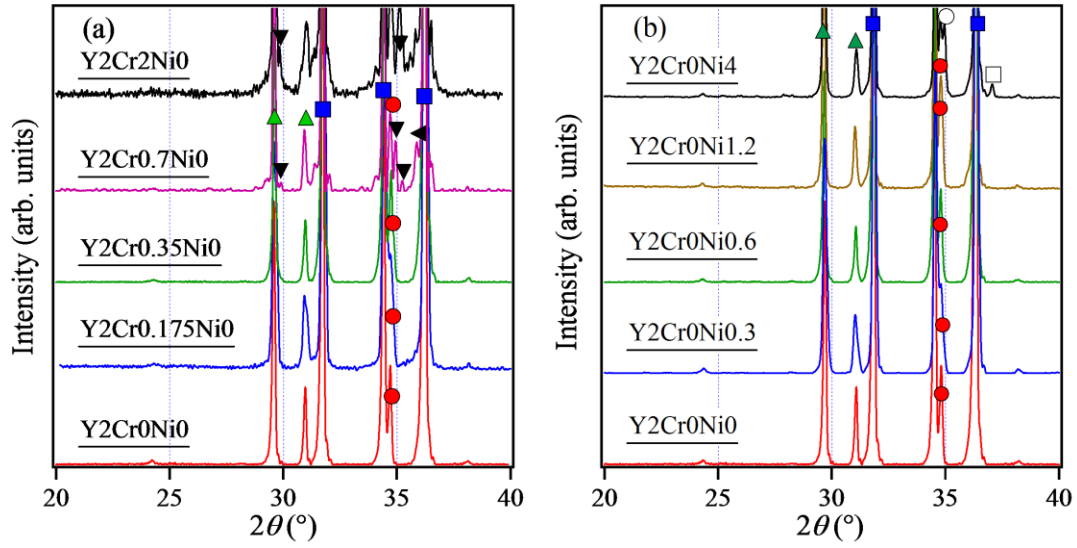


Figure 5.10 XRD patterns for (a) $Y_2Cr_yNi_0$ and (b) $Y_2Cr_0Ni_z$. ■ : ZnO, ● = spinel, ▲ : Y-compound, ▼ : $Zn_{1.82}Cr_{0.78}Sb_{0.41}O_4$, ◄ : $ZnCr_2O_4$, ◻ : $Zn_{0.3}Ni_{0.7}O$, ○ : $ZnNi_{1.33}Sb_{0.67}O_4$.

5.5.1 Electrical degradation under DC bias

Electrical degradation is caused by various mechanisms, such as irreversible electrical destruction of the grain boundary, diffusion of oxide ions and/or Zn^{2+} ions, and oxygen adsorption or desorption at the grain boundary¹⁹. It has been reported that when spot-like Bi_2O_3 at the grain boundaries transforms to a sheet-like Bi deposit, the resistance to degradation is increased, as the movement of oxide ions and/or Zn^{2+} is hindered²⁰. The structure of Bi_2O_3 and the evaporation of Bi are important factors influencing the leakage current and resistance to overload. In this study, the same sintering temperature was applied in all cases to maintain the same amount of Bi in all samples. In addition, we have found that when sintering at 1150 °C for 3 h, negligible Bi evaporation occurred. Ni and Cr did not form new compounds with Bi in Y-doped varistors according to XRD, and there was no change in the microstructure, which indicated that Ni and Cr do not affect Bi evaporation. Since the V_N - J relationship mostly recovered after annealing at 200 °C to that obtained before degradation for all the samples prepared in this research, it is likely that the main factor in degradation is diffusion of oxide ions and/or Zn^{2+} to and/or across grain boundaries under the application of a bias voltage. Furthermore, these results suggest that most of the Bi, except that necessary to create nonlinear V_N - J characteristics, was dissolved in the Y-compounds, such that a residual amount of Bi was

uniformly distributed at the boundaries between ZnO grains. This lack of Bi is probably the reason for the low nonlinearity of Y2Cr0Ni0 and Y2Cr0.35Ni0.6, as shown in Fig. 5.8(a). Nevertheless, the lack of a good oxide conductor Bi-layer may be the basis for the improvement in the resistance to degradation that occurs with addition of Cr or Ni.

5.5.2 Interface state levels at gran boundaries

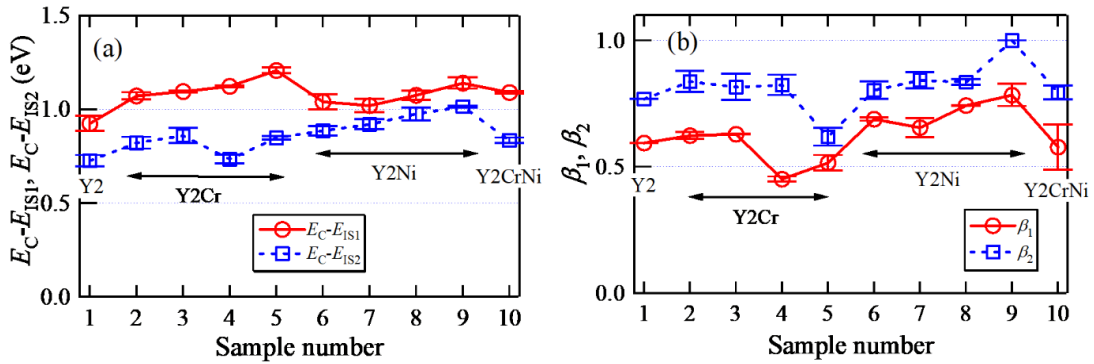


Figure 5.11 (a) $E_C - E_{IS1}$ and $E_C - E_{IS2}$ and (b) β_1 and β_2 for Y-doped samples.

Figure 5.11 (a) shows $E_C - E_{IS1}$ (referred to E_1) and $E_C - E_{IS2}$ (E_2) and Fig. 5.11 (b) shows β_1 and β_2 at 100 °C for Y-doped samples. The difference between E_1 and E_2 was small for samples containing Ni and relatively large for samples with Cr. The deeper interface level E_1 increased from 0.9 to 1.2 eV as the amount of Cr increased from 0 to 2 mol%. However, the shallower E_2 level for Cr addition increased from 0.73 eV and reached a maximum of 0.86 eV at 0.35 mol% before decreasing to 0.73 eV at 0.7 mol% and then increasing again at 2 mol%. Both E_1 and E_2 for Ni addition became monotonically deeper with increasing amounts of Ni from 0.9 to 1.14 eV and from 0.73 to 1.02 eV, respectively. The distribution for both levels did not change much on increasing Cr_2O_3 from 0 to 0.35 mol%. However, β_1 for Cr_2O_3 content of 0.7 and 2 mol% and β_2 for Cr_2O_3 content of 2 mol% decreased noticeably, when $\text{Zn}_{1.82}\text{Cr}_{0.78}\text{Sb}_{0.41}\text{O}_4$ spinel started to appear. The Fermi level became deeper on addition of Cr and/or Ni. Since both E_1 and E_2 changed notably with addition of Cr or Ni, one of the interface state levels may be related to oxide ions, as reported previously, and the other is related to the spinel-phase dissolution of Cr (i.e., ZnCr_2O_4 and $\text{Zn}_{1.82}\text{Cr}_{0.78}\text{Sb}_{0.41}\text{O}_4$) or Ni ($\text{ZnNi}_{1.33}\text{Sb}_{0.67}\text{O}_4$) rather than Co and Mn. It has been reported that the deeper interface state level with a slower electron emission process could be attributed to the existence of a Bi_2O_3 layer at the grain boundary ²¹.

Since the Bi-layer was absorbed in the Y-compound for Y-doped samples, and the deeper level is not generated from the Bi-rich layer, it is speculated that the origin of the deeper level is different from that for samples without Y. At this stage, however, the origin of the interface state levels is unknown for Y-doped samples.

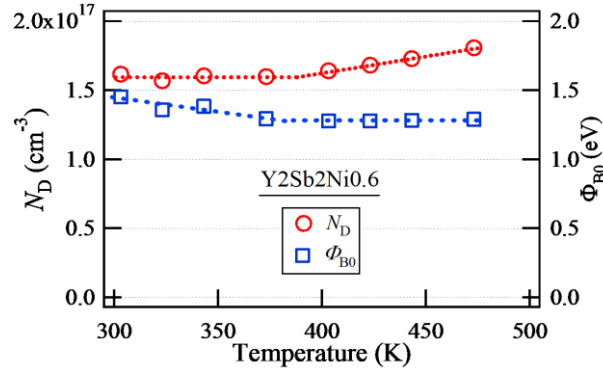


Figure 5.12 The values of Φ_{B0} and N_D with increasing temperature from 30 to 200 °C.

Φ_{B0} and N_D were not significantly affected by temperature as shown in Fig.5.12. The accuracy of the measured Φ_{B0} and N_D depends mainly on the validity of the pinning of the Fermi level. The values of N_D did increase slightly ($\approx 10\%$) above ≈ 100 °C, while the values of Φ_{B0} decreased slightly ($\approx 15\%$) with increasing temperature and became constant above ≈ 100 °C. It is conjectured that this result is due to the change in interface charge density Q_0 with changing temperature, since Φ_{B0} is proportional to Q_0^2/N_D . Because the shallower donor levels of ZnO grains were completely ionized, the charge distribution of ions did not change there. However, the deeper donor levels were not fully ionized below ≈ 100 °C, so temperatures above ≈ 100 °C may have resulted in minor increases in ionization.

A summary of Φ_{B0} , N_D , and N_{IS0} for all samples is displayed in Fig. 5.13. Due to the method used to study $C-V$ characteristics measurements below 100 °C were difficult to obtain, as they have large deviations in Φ_{B0} . Therefore, the data for Φ_{B0} , N_D and N_{IS0} at 100 °C were used. Though value of N_D was changed prominently by adding Cr or Ni for Y-doped samples, the change of Φ_{B0} was relatively small regardless of the amount of Cr or Ni added. The suppression of the change of Φ_{B0} is because the change of interface state density in proportion to N_D . This result suggests that the origin of donor and interface state levels is depended on addition of Cr and/or Ni. Such suppression was not observed for samples without Y. As important response to

the addition of Y, the value of Φ_{B0} became ≈ 1.5 times larger than those for the samples without Y.

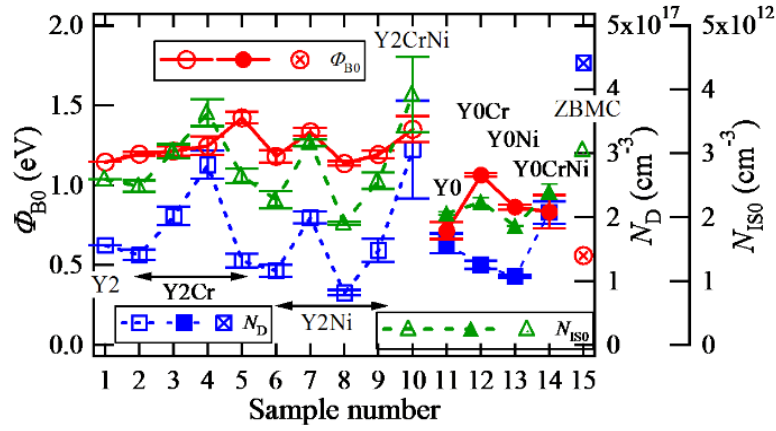


Figure 5.13 Φ_{B0} , N_D , and N_{IS0} for each sample.

The results for Φ_{B0} , N_D and N_{IS0} suggest that Cr and Ni exist both at grain boundaries and in ZnO grains, and Cr acts as a donor ion, as confirmed by EDS elemental analysis (see Table 5.2). Because Bi_2O_3 and spinel particles at grain boundaries and triple points were absorbed in Y compound, a modified ZnO/ZnO grain boundary structure enhances the effect of Cr or Ni additives on conductance processes and the electron absorption ability. Cr causes N_D to increase by dissolving in ZnO grains, substituting for a Zn^{2+} ion at a normal site and acting as a donor, or existing at an interstitial site and generating an oxide ion and a reduction in oxygen vacancies at the grain boundary due to its valence of +3 or higher. The presence of fewer oxygen vacancies will hinder the transport of oxide ions, so that adsorbed oxygen at grain boundaries will be decreased. Although part of Ni also dissolves in ZnO grains, substituting for a Zn^{2+} ion at normal sites, Ni^{2+} does not act as a donor due to its +2 valence state, and as a result does not increase N_D . Ni exists in ZnO grains and/or at grain boundaries as the compound $Zn_{0.7}Ni_{0.3}O$. With the decrease in adsorbed oxygen caused by adding Cr or Ni, high resistance to degradation is achieved. The addition of Ni has a weaker ability to restrain degradation compared with Cr, which matches the data shown in Fig. 5.7 (b), (c).

5.6 Simulation of electrical properties with thermionic mechanism model and comparison with experimental results

5.6.1 Simulation with thermionic mechanism model

A further step to understand the effects of Cr and/or Ni on the electrical properties is discussed below. A model of the Schottky barrier structure and interface state levels for ZnO varistors considering Fermi level pinning is proposed. The simulation values are compared with experimental values and the relation between factors, such as V_{NNGB} , $\Phi_{\text{B}}(V)$, N_{D} , N_{IS} , α , β and related factors, is discussed.

Fermi level pinning near the interface state level was previously confirmed. The barrier height on each side will be changed on applying a bias voltage. If the barrier height on the forward bias side is expressed as $\Phi_{\text{B}}(V_{\text{GB}})$, $\Phi_{\text{B}}(V_{\text{GB}})$ is given by ²²

$$\Phi_{\text{B}}(V_{\text{GB}}) = S(V_{\text{GB}})^2 \left(1 - \frac{eV_{\text{GB}}}{4S(V_{\text{GB}})^2 \Phi_{\text{B0}}} \right)^2 \Phi_{\text{B0}}, \quad (5.1)$$

where S is the increase rate for interface charges

$$S(V_{\text{GB}}) = \frac{N_{\text{ISO}} + \sum_{i=1}^2 N_{\text{IS}_i}(V_{\text{GB}})}{N_{\text{ISO}}}. \quad (5.2)$$

If the Fermi level is pinned at the interface state level,

$$S(V_{\text{GB}})^2 \left(1 - \frac{eV_{\text{GB}}}{4S(V_{\text{GB}})^2 \Phi_{\text{B0}}} \right)^2 \approx 1. \quad (5.3)$$

The width of the depletion layer w_{DL} is given by

$$w_{\text{DL}}(V_{\text{GB}}) = \frac{N_{\text{IS}}(V_{\text{GB}})}{N_{\text{D}}} = \frac{N_{\text{ISO}} + N_{\text{IS}_1}(V_{\text{GB}}) + N_{\text{IS}_2}(V_{\text{GB}})}{N_{\text{D}}} = \frac{N_{\text{ISO}}}{N_{\text{D}}} S(V_{\text{GB}}). \quad (5.4)$$

The following equation is obtained by solving Poisson's formula regarding the electric charge distribution near the grain boundary. The interface charge, which depends both on the applied bias voltage V_{GB} and the barrier height $\Phi_{\text{B}}(V_{\text{GB}})$, is given by ^{23,24}

$$\begin{aligned} & (2\varepsilon N_{\text{D}})^{\frac{1}{2}} \left[\Phi_{\text{B}}(V_{\text{GB}})^{\frac{1}{2}} + (\Phi_{\text{B}}(V_{\text{GB}}) + V_{\text{GB}})^{\frac{1}{2}} \right] \\ & = e \int_{E_{\text{V}}}^{E_{\text{C}}} N_{\text{IS}}(E) f(E, E_{\text{F}}) dE \equiv eN_{\text{ISMAX}}, \end{aligned} \quad (5.5)$$

where $N_{IS}(E)$ is the density of interface states, E_F is the quasi-Fermi level, E_V is the top edge of the valence band, $f(E, E_F)$ is the Fermi-Dirac energy distribution function, and N_{ISMAX} is the total density of interface states between E_V and E_C . E_F is given by

$$E_F = F_{FG} - \Phi_B(V_{GB}) - k_B T \ln \left[\frac{1 + \exp\left(-\frac{eV_{GB}}{k_B T}\right)}{2} \right], \quad (5.6)$$

where E_{FG} is the Fermi level for a ZnO grain and $E_C - E_{FG} \approx 0.034$ eV for a Bi-based varistor. Figure 5.13(a) shows the $\Phi_B(V_{GB}) - V_{GB}$ relationship simulated for various N_{ISMAX} , distribution parameters β , and E_{IS0} by solving self-consistent formula Eq. 5.5 of $\Phi_B(V_{GB})$ for $N_D = 1 \times 10^{18}$ cm⁻³ and considering the distribution of interface state levels, $N_{IS}(E)$ given by ²³

$$N_{IS}(E) = N_{ISMAX}(E) \frac{\rho(E)}{\int_{E_V}^{E_C} \rho(E) dE}, \quad (5.7)$$

where $\rho(E)$ is the energy density of the interface state levels. In the case of one interface state, $\rho(E)$ is given by ²⁵

$$\rho(E) = -\frac{e}{\pi k_B T} \sum_{n=0}^{\infty} \left(-\frac{1}{\mu(E)^\beta} \right)^n \sin(n\pi\beta) \frac{\Gamma(n\beta+1)}{\Gamma(n+1)}, \quad (5.8)$$

where $\Gamma(x)$ is Euler's gamma function for x , and from Eq. 4.4, $\mu(E)$ is given by

$$\mu(E) = \frac{\tau(E)}{\tau_0} = \exp\left(-\frac{E - E_{IS}}{k_B T}\right), \quad (5.9)$$

where E_{IS} is the energy of the interface state determined from ICTS measurements. Assuming that only the thermionic emission mechanism takes place, the current density $J(V_{GB})$ is given by

$$J(V_{GB}) = A^* T^2 \exp\left(-\frac{\Phi_B(V_{GB}) + E_C - E_{FG}}{k_B T}\right), \quad (5.10)$$

where A^* is the Richardson constant. $J(V_{GB})$ increases rapidly with decreasing $\Phi_B(V_{GB})$. Figure 5.14(b) shows the $V_{GB} - J(V_{GB})$ relationship calculated for various conditions, as listed in Fig. 5.14(a) with Eq. 5.10. The dotted line in Fig. 5.14(b) shows the $V_{GB} - J(V_{GB})$ relationship for a smaller N_{ISMAX} compared to others. V_{NNGB} is also small, while the others are the same.

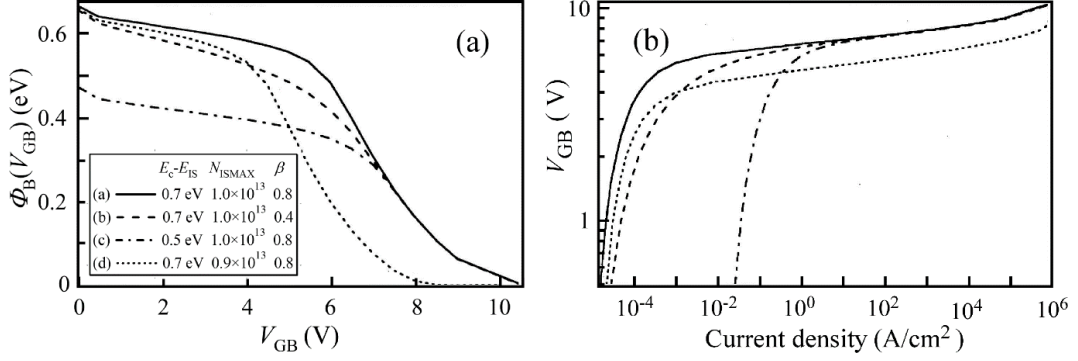
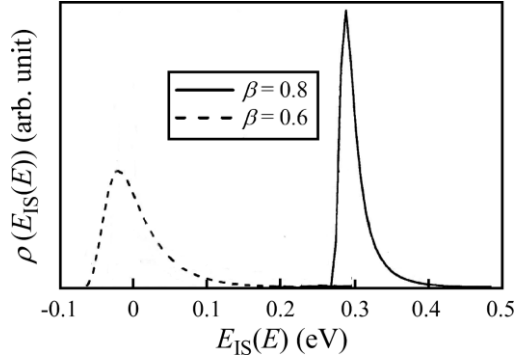
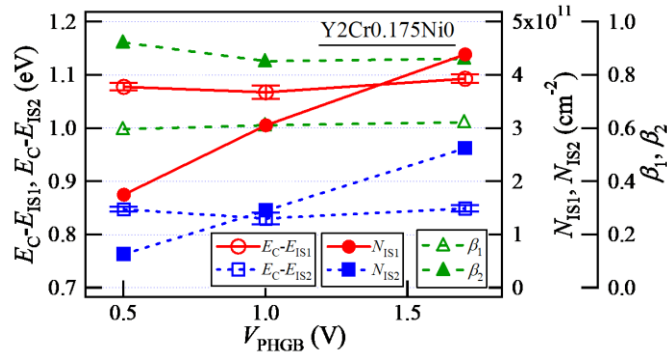


Figure 5.14 (a) $\Phi_B(V_{GB})-V_{GB}$ relationship for various N_{ISMAX} , β , and E_{IS0} solving the self-consistent formula of $\Phi_B(V_{GB})$ for $N_D=1 \times 10^{18} \text{ cm}^{-3}$, (b) V_{GB} -current density J relationship calculated for various conditions.

From the simulation for N_D , we obtain the following results:

1. The varistor voltage V_{NNGB} is determined by N_{ISMAX} and is not related to either the depth of the interface state level E_C-E_{IS} or the distribution parameter β .
2. The barrier height Φ_{B0} is determined by the depth of interface state level E_C-E_{IS} , and Φ_{B0} becomes large, so that the E_C-E_{IS} is deepened.
3. A broader distribution of energy for interface states leads to a rapid decrease in $\Phi_B(V_{GB})$ with increasing bias, resulting in a small nonlinearity and an increase in the leakage current, as the dashed line shows.
4. The nonlinearity index α at lower current densities in the breakdown region is determined by the distribution parameter β for the energy of interface state levels, and the value of α becomes large, so the distribution becomes narrower²⁶.
5. If the interface state level becomes shallower (the dot-dash line shown in Fig. 5.13(b)), the leakage current increases drastically²⁷.

Figure 5.15 shows the simulated values of $\rho(E_{IS})$ for two interface state levels. The parameters used are the same as those of Fig. 5.14. The energy distribution parameter for the deeper one β_1 is 0.6, the shallower one β_2 is 0.8, and the difference in energy for the two levels is 0.3 eV. There is almost no overlap region for the two levels. Therefore, electrons are captured in order by the interface state levels, starting with the deeper one and then proceeding to the shallower one. However, the experimental results shown in Fig. 5.16 are contradictory to the above simulation results.


 Figure 5.15 Simulated values of $\rho(E_{IS})$ for two interface state levels.

 Figure 5.16 $E_C - E_{IS1}$, $E_C - E_{IS2}$, N_{IS1} , N_{IS2} , β_1 , and β_2 for Y2Cr0.175Ni0.

The changes in both E_1 and E_2 were ≈ 0.02 eV between 0.5 and ≈ 1.7 V V_{PHGB} , as shown in Fig. 5.16 for Y2Cr0.175Ni0 as an example. It has been suggested that the Fermi level is pinned by the increase in interface charge if empty interface states are present and as a result, the barrier height on the forward biased side is almost fixed. Furthermore, since both N_{IS1} and N_{IS2} depend on V_{PHGB} and increase in proportion to V_{PHGB} , electrons are captured and emitted evenly by both interface state levels. Since both the distribution parameters β_1 and β_2 were ≈ 0.6 and ≈ 0.8 , respectively, and were independent of V_{PHGB} , it was found that the distributions of interface state levels were affected by the applied voltage. It is worth noting that since it is the general view that electrons are captured in order by interface state levels from deeper ones to shallower ones, our result that electrons are captured and emitted evenly by both interface state levels is surprising.

5.6.2 Relationship between Electrical properties and interface states

Because it was confirmed that the Fermi level is pinned at the interface state level by application of V_{GB} ($< V_{NNGB}$), $\Phi_B(V_{GB})$ is nearly equal to Φ_{B0} at $V_{GB} \leq V_{NNGB}$. Equation (5.5) was modified at $V_{GB} \approx V_{NNGB}$ as^{22,26}

$$V_{\text{NNGB}} \approx 4\Phi_{\text{B0}}S_{\text{MAX}}(S_{\text{MAX}} - 1). \quad (5.11)$$

V_{NNGB} is simply given by the product of Φ_{B0} and $S_{\text{MAX}}(S_{\text{MAX}} - 1)$. Therefore, it is found that the main factor causing the increase in V_{NNGB} due to Y doping in addition to the reduction in ZnO grain size S_{G} is the increase in Φ_{B0} , as shown in **Fig. 5.13**. Because the values of V_{NNGB} and Φ_{B0} are known, S_{MAX} can be estimated using **Eq. (5.11)**. The change in V_{NNGB} was almost the same as the change in the product of S_{MAX} and $(S_{\text{MAX}} - 1)$, as shown in **Fig. 5.17**, as the amounts of Cr or Ni were varied. It is revealed that the addition of Cr and/or Ni does not change Φ_{B0} but changes S_{MAX} prominently. As a result, the change in V_{NNGB} was related mainly to the ratio of empty interface state to N_{IS0} under no bias for Y-doped samples. On the other hand, no apparent correlation between V_{NNGB} and S_{MAX} or between V_{NNGB} and Φ_{B0} was observed for the samples without Y, as shown in **Fig. 5.17**.

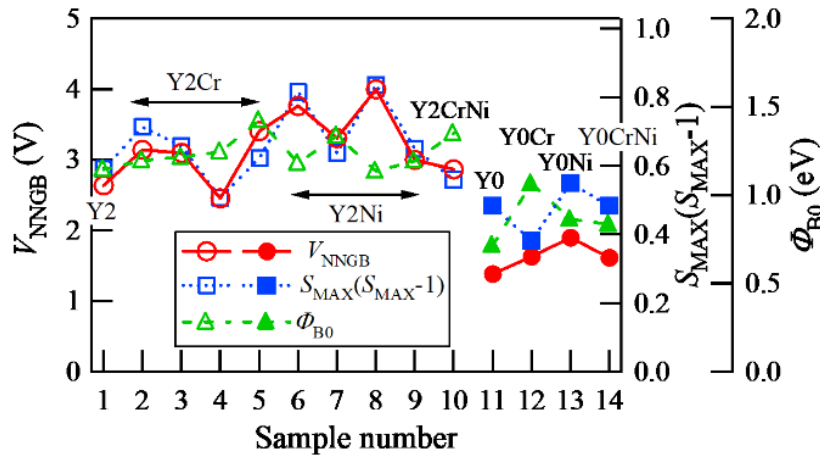


Figure 5.17 Relations between V_{NNGB} , $S_{\text{MAX}}(S_{\text{MAX}} - 1)$, and Φ_{B0} for all samples.

Assuming that only thermionic emission takes place, the theoretical maximum value of the nonlinearity index α_{MAX} before electrical degradation is given by ^{22,26}

$$\alpha_{\text{MAX}} = \text{MAX} \left[\frac{d \ln J_{\text{N}}}{d \ln V_{\text{N}}} \right] \approx \frac{\Phi_{\text{B0}} S_{\text{MAX}}^2}{2k_{\text{B}}T}, \quad (5.12)$$

in the breakdown region. The experimental maximum point for the nonlinearity index α_{asMAX} is derived from $d \ln(J)/d \ln(V_{\text{N}})$. Figure 5.18 (a) shows the $d \ln(J)/d \ln(V_{\text{N}})$ – J relationship and the measured V_{N} – J relationship for Y2Cr0.35Ni0 as an example. $d \ln(J)/d \ln(V_{\text{N}})$ reaches the maximum α_{asMAX} at $\approx 10^{-5}$ A/cm² in the small-current part of the breakdown region around room temperature. The value of α_{asMAX} is not the same as that of α_{as} in the larger-current part of the breakdown region shown in Fig. 5.9, since they are measured in different current density regions. The V_{N} – J relationship for the first measurement is shown in the same Figure. The apparent maximum does not appear due to the decrease in electrical resistance in the range of

the pre-breakdown region at high temperatures. Figure 5.18 (b) shows the measured values of the maximum nonlinearity index α_{asMAX} before electrical degradation at 30°C, α_{MAX} , S_{MAX}^2 , and Φ_{B0} for Y-doped samples. The values of α_{asMAX} agreed well with α_{MAX} for Y-doped samples. For Y2Cr, the change in the value of α_{asMAX} was correlated with S_{MAX}^2 strongly and was similar to the change in the values of J_{Ldeg}/J_{Lbef} . It shows the increase of S_{MAX}^2 leads to the increase of resistance to degradation.

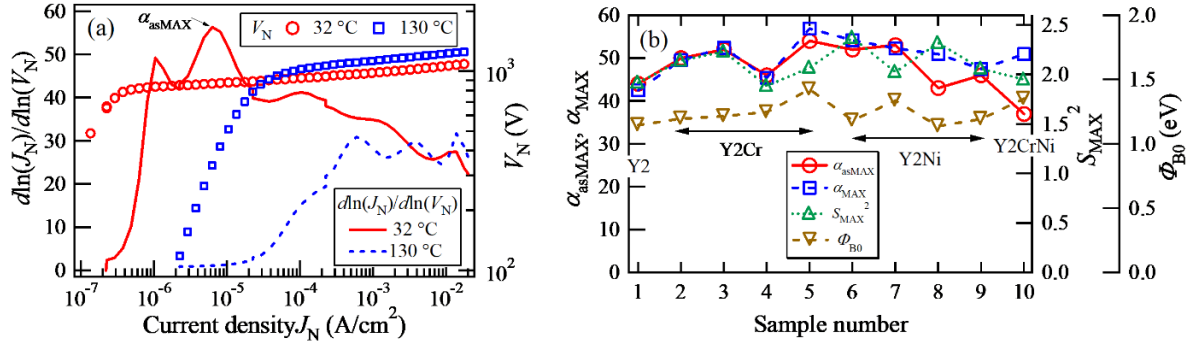


Figure 5.18 (a) $d\ln(J)/d\ln(V_N)$ - J relationship and measured V_N - J relationship for Y2Cr0.35Ni0 at 32 and 130 °C, (b) Measured values of nonlinearity index α_{asMAX} before electrical degradation, α_{MAX} , and S_{MAX}^2 for each sample.

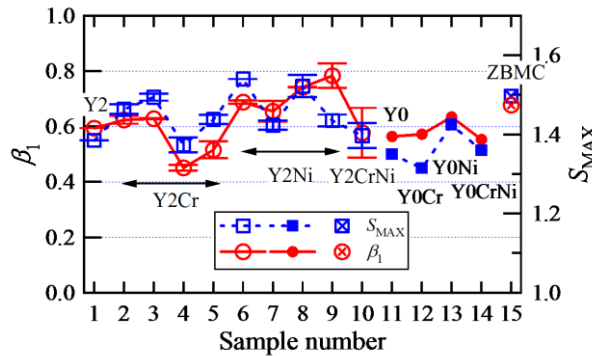


Figure 5.19 Relation between β_1 and S_{MAX} for each sample.

If thermionic emission is dominated, the α_{asMAX} becomes large so that the distribution of the energy for an interface state level becomes narrower as shown in Fig. 5.14 (b) in the simulation section above. When S_{MAX} decreased, α_{asMAX} decreased. Therefore, it is expected that S_{MAX} correlates with the distribution parameters β_1 and/or β_2 . It was found that β_1 for the deeper interface state level is correlated with S_{MAX} strongly, as shown in Fig. 5.19. This result indicates

that the available relative density of empty interface states becomes large as the distribution parameter becomes large, and as a result the distribution becomes narrower.

5.7 Conclusion

The effects of adding Cr and/or Ni to Y-doped Bi-based ZnO varistors were investigated with regards to the microstructure at grain boundaries, the electrical properties, and the interface states.

1. V_{NNGB} increased from 2.6 to 3.3 V when increasing the amount of Cr_2O_3 to 0.35 mol% and increased to 4 V for 1.2 mol% NiO. The optimum amount of Cr_2O_3 was found to be 0.35 mol%, with V_{NN} of ≈ 1030 V, nonlinear index α_{as} and α_{deg} of 35, very low leakage current at $\approx 5 \times 10^{-7}$ A/cm², and excellent resistance to electrical degradation. In addition, two interface state levels were confirmed. One was related to the spinel phase dissolving Cr or Ni, which lead to a reduction in the resistance to degradation. The highest varistor voltage was ≈ 1500 V for 0.3 mol% NiO.
2. The dissolved Cr in ZnO increased N_{D} due to acting as a donor and reduced the number of oxygen vacancies at grain boundaries. It is considered that reduction of oxygen vacancies improved the resistance to electrical degradation and decreased J_{L} by inhibiting oxide ion transport. This occurs with the cooperation of Y, which modified the ZnO/ZnO interface microstructure by forming Y-compound and decreases the good oxide conductor Bi_2O_3 and spinel particles, and enhances the effects of Cr and Ni.
3. Though value of N_{D} was changed prominently by adding Cr or Ni for Y-doped samples, the change of Φ_{B0} was relatively small regardless of the amount of Cr or Ni added. The suppression of the change of Φ_{B0} is due to the change of interface state density in proportion to N_{D} . It is suggested that the origin of donor and interface state levels is the same. Such suppression was not observed for samples without Y.
4. The change of V_{NNGB} was related mainly to the relative empty interface state density to N_{IS0} under no bias for Y-doped samples.
5. The maximum nonlinearity index α_{asMAX} is dominated by S_{MAX} and increases so that the distribution of the energy for an interface state level narrows.
6. The optimum amount of Cr or Ni additive decreases the distribution of interface state levels and increased the empty interface states, as a result, leads to the increase in the resistance to electrical degradation and the decrease in leakage current density.

References

1. J. He, Metal oxide varistors: From microstructure to macro-characteristics, Wiley Online Library 2019, 1–279.
2. T. Takemura, M. Kobayashi, Y. Takada, K. Sato, Effect of antimony oxide on the characteristics of ZnO varistors, *J. Am. Ceram. Soc.* 70 (1987) 237–241.
3. N. Daneu, A. Rečnik, S. Bernik, Grain growth control in Sb₂O₃-doped zinc oxide, 2003.
4. S. Bernik, S. Macek, B. Ai, Microstructural and electrical characteristics of Y₂O₃-doped ZnO-Bi₂O₃-based varistor ceramics, *J. Eur. Ceram. Soc.* 21 (2001) 1875–1878.
5. S. Bernik, S. Macek, A. Bui, The characteristics of ZnO-Bi₂O₃-based varistor ceramics doped with Y₂O₃ and varying amounts of Sb₂O₃, *J. Eur. Ceram. Soc.* 24 (2004) 1195–1198.
6. Y. Akiyama, M. Takada, A. Fukumori, Y. Sato, S. Yoshikado, Effects of Zr and Y addition on the electrical degradation characteristics of ZnO varistors, *Key Eng. Mater.* 445 (2010) 237–240.
7. P. Meng, S. Lyu, J. Hu, J. He, Indium tailors the leakage current and voltage gradient of multiple dopant-based ZnO varistors, *Ceram. Int.* 43 (2017) 4127–4130.
8. P. Meng, J. Wu, X. Yang, J. Hu, J. He, Electrical properties of ZnO varistor ceramics modified by rare earth-yttrium and gallium dopants, *Mater. Lett.* 233 (2018) 20–23.
9. S. Yang, D. Zhu, Effect of co-doping Y₂O₃-La₂O₃ on microstructure and electrical properties of ZnO-based varistor ceramics prepared from nanosize ZnO powder, *J. Mater. Sci.: Mater. Electron* 29 (2018) 3104–3109.
10. Y. H. Kim, H. Kawamura, M. Nawata, The effect of Cr₂O₃ additive on the electrical properties of ZnO varistor. *J. Mater. Sci.* 32 (1997) 1665–1670.
11. H. Bai, S. Li, Y. Zhao, Z. Xu, R. Chu, J. Hao, C. Chen, H. Li, Y. Gong, G. Li, Influence of Cr₂O₃ on highly nonlinear properties and low leakage current of ZnO–Bi₂O₃ varistor ceramics, *Ceram. Int.* 42 (2016) 10547–10550.
12. X. Ruan, X. Ren, W. Zhou, X. Xu, X. Wang, M. Wang, Y. Yan, Z. Yao, W. Shi, W. Yu, Effects of SiO₂/Cr₂O₃ ratios on microstructures and electrical properties of high voltage gradient ZnO varistors., *J. Mater. Sci.: Mater. Electron* 30 (2019) 12113–12121.
13. Z. Xu, H. Bai, S. Ma, R. Chu, J. Hao, C. Chen, Effect of a Bi–Cr–O synthetic multi-phase on the microstructure and electrical properties of ZnO–Bi₂O₃ varistor ceramics, *Ceram. Int.* 42 (2016) 14350–14354.

14. H. Kanai, M. Imai, Effects of SiO₂ and Cr₂O₃ on the formation process of ZnO varistors, *J. Mater. Sci.* 23 (1988) 4379–4382.
15. T. Kato, I. Kawamata, A. Yamada, S. Ishibe, Effect of Ni and Cr on the stability of leakage current for spinel-reduced ZnO varistor ceramics, *J. Ceram. Soc. Jpn.* 119 (2011) 234–237.
16. Y. Kojima, Study on Effects of Simultaneous Addition of Antimony, Yttrium and Silicon Oxides to Bi-based Zinc Oxide Varistors on the Electrical Characteristics, Master thesis, Doshisha University, 2014.(in Japanese)
17. M. A. Nobre, S. Lanfredi, Electrical characterization by impedance spectroscopy of Zn₇Sb₂O₁₂ ceramic, *Mat. Res.* 6 (2003) 151–155.
18. Z. Brankovic, G. Brankovic, D. Poteli, J. A. Varela, Structural and electrical properties of ZnO varistors containing different spinel phases, *Ceram. Int.* 27 (2001) 115–122.
19. T. K. Gupta, W.G. Carlson, A grain-boundary defect model for instability/stability of a ZnO varistor, *J. Mater. Sci.* 20 (1985) 3487–3500.
20. M. Takada, Y. Sato, S. Yoshikado, Relation between grain boundary structure and electrical degradation in zinc oxide varistors, *J. Am. Ceram. Soc.* 95 (2012) 2579–2586.
21. Y. Sato, S. Yoshikado, Effects of addition of Al on electrical degradation of ZnO varistors, *IEEJ Trans. FM* 123 (2003) 139–145.
22. A. Tanaka, K. Mukae, ICTS measurements of single grain boundaries in ZnO: rare-earth varistor, *J. Electroceram.* 4; S1 (1999) 55–59.
23. G. Blatter, F. Greuter, Carrier transport through grain boundaries in semiconductors, *Phys. Rev. B*, 33(6) (1986) 3952–3966.
24. F. Greuter, G. Blatter, Electrical properties of grain boundaries in polycrystalline compound semiconductors, *Semiconductor Sci. Technol.* 5(2) (1990) 111–137.
25. P. Q. Mantas, J. L. Baptista, The barrier height formation in ZnO varistors, *J. Eur. Ceram. Soc.* 15 (1995) 605–615.
26. J. Bernasconi, H. P. Klein, B. Knecht, S. Strässler, Investigation of various models for metal oxide varistors, *J. Electronic Materials*, 5 (1976) 473–494.
27. J. Bernasconi, S. Strässler, B. Knecht, H. P. Klein, A. J. Menth, Zinc oxide based varistors: A possible mechanism, *Solid State Commun.* 20 (1976) 1053–1056.

Chapter 6

Effect of B₂O₃ on Y-doped high voltage ZnO varistors

As mentioned in chapter 5, the previous study revealed that Y-doped varistors exhibited a very high varistor voltage of up to 1000 V/mm. However, leakage current was increased, and severe electrical degradation occurred. Electrical degradation occurs during or after application of a high voltage, especially under a high DC voltage: electrical properties such as the varistor voltage, nonlinearity index, and leakage current deteriorate, which shortens the device lifespan and causes power loss and device failure. The cause of this phenomenon is complicated¹, and includes ion migration^{2,3}, thermionic emission⁴, Schottky barrier distortion under bias^{1,5,6}, oxygen desorption⁷, loss of Bi₂O₃⁸⁻¹⁰ and others¹¹⁻¹³. Methods to improve electrical degradation are a common topic of study. Thermal annealing^{14,15} is an industrial method used to recover intergranular defects to reduce interstitial ions. Additives such as SiO₂¹⁶ and B₂O₃¹⁷⁻²⁰ can reduce the leakage current. Liu¹⁷ reported that 0–3.5 mol B₂O₃ decreased the grain size and varistor voltage. They also reported that a Bi-B glass existed within the samples. Cheng *et al.*¹⁸ reported that B addition increased V_N by increasing the barrier height and width. These controversial results drew attention to the relation between B₂O₃ and other impurities in Bi-based varistors. Effects of addition of Bi-B frit¹⁹ into Bi-based ZnO varistors also have been reported. Hao *et al.*²⁰ reported that ZnO varistor ceramics doped with an optimal amount of B₂O₃ and Al₂O₃ showed excellent electrical properties. Due to the complicated composition of ZnO varistors, the mechanism for changing electrical degradation by B-doping is unclear. Furthermore, the precise location and form of the B ions are also unknown.

We speculated that B₂O₃ may have the ability to change the electrical properties because boron ions have a very small radius, which may allow them to move easily into ZnO grains and grain boundaries, and have a strong covalent energy that may block interstitial ions, such as oxide ions and Zn²⁺ in ZnO grains. The B₂O₃ also may affect other additives inside and outside of ZnO grains by occupying their positions and changing the microstructure of the Y-compound, which improves the electrical properties. In this study, B₂O₃ was added to Y-doped varistors and the intergranular microstructure, interface states, Schottky barrier structure, and conduction processes through a double Schottky barrier were examined in detail to provide insights into the electrical properties. The correlation between B and other additives, especially Bi and Co, was also investigated.

6.1 Experimental procedures

Varistor samples were fabricated from ZnO 100 mol%, with the addition of Bi₂O₃ (0.6 mol%), MnO₂ (0.55 mol%), Co₃O₄ (0.63 mol%), Cr₂O₃ (0.35 mol%), NiO (0.6 mol%), or Sb₂O₃ (2 mol%) as basic composites, and additive Y₂O₃ (0 or 2 mol%), or B₂O₃ ($X=0-2$ mol%). Samples names were based on mol% amount of additives, *e.g.*, Y2B1 represents 2 mol% Y₂O₃ and 1 mol% B₂O₃ doped samples. Varistor samples were prepared by the same method described in chapter 4. In addition, to determine the reason for degradation, thermal annealing treatment at 700°C in air were applied to some samples. Electrical properties were evaluated as described in chapter 4. Cross-sectional morphology was analyzed using SEM, element locations were determined by EDS. Crystal structure was identified by XRD. The microstructure of grain boundaries was observed by TEM under 200 kV acceleration voltage. Chemical compositions were determined by EDS. The position of boron was observed using a field emission electron probe micro analyzer (EPMA, JXA 8530F Plus, Jeol Co. Ltd).

6.2 Microstructure and the location of boron

Figure 6.1(a) shows XRD diffraction patterns for Y2BX samples ($X = 0-2$ mol%). The main diffraction peaks were from wurtzite ZnO (JCPDS 89-0510). The secondary diffraction peaks were due to Y-compounds in Y-doped samples and spinel particles Zn_{2.33}Sb_{0.67}O₄ (JCPDS 15-0687). No diffraction peaks for compounds related to B were observed, which indicates B may be dissolved in other compounds such as ZnO or secondary phases. Cobalt and Ni also dissolved in ZnO, so no related diffraction peaks were found. The relative intensity *RII* calculated from the area of the diffraction peaks for ZnO (100), (002), and (101) planes, spinel, and Y-compound are shown in Fig. 6.1(b). The *RII* value for spinel decreased upon addition of B and did not change with increasing amounts of B. The *RII* value for the Y-compound increased at 0.75 mol% B₂O₃. Figure 6.1(c) shows XRD diffraction patterns for Y2BX samples ($X = 0-2$ mol%) in the narrower 2θ range around the (002) plane diffraction peak for ZnO. A minute structural change was observed due to the secondary phase. For Y2BX with 0 and 0.25 mol% added B₂O₃, two diffraction peaks appeared at 34.7–34.8°, associated with a spinel structure that contained Co (Co-spinel), Co_{1.73}O₄Sb_{0.67}Zn_{0.6} (JCPDS 089-6005) at 34.7°, and another related to Y-compound near 34.8°. When the B₂O₃ content was increased to 0.5 mol%, these two peaks merged into one around 34.76°, which indicates the Co-spinel decreased with increasing amount of B₂O₃. Note that no Bi₂O₃ peak was found in Y2BX, which is different

from the common Bi-based ZnO varistors^{9,10}, because the Bi was completely absorbed by the Y-compound according to the additive amount. The Y0BX samples with a basic composition showed nearly the same XRD diffraction peaks as those from other reports⁹⁻¹¹, as shown in Appendix Fig. A2. The results for the Y0BX samples are available in Fig. S6.1 in the Supplemental Information. In those samples, a peak due to another Co-spinel compound, $\text{Co}_{1.33}\text{O}_4\text{Sb}_{0.67}\text{Zn}$ (pdf no. 89-6004), was found near 34.6° , and its intensity decreased with

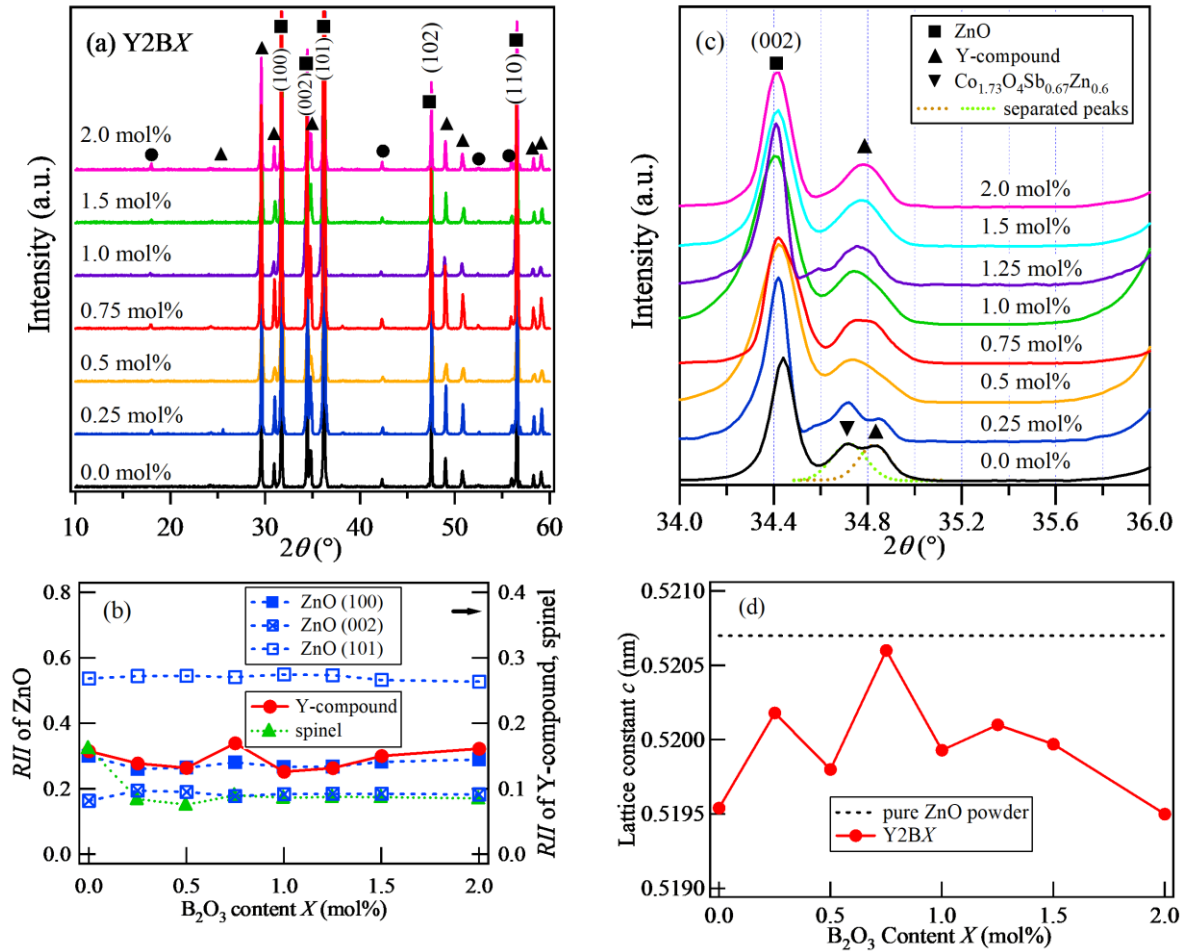


Figure 6.1 (a) XRD patterns for Y2BX ($X=0-2$ mol%), ●: spinel, ▲: Y-compound, ▼: Co-containing spinel, ▶: $\beta\text{-Bi}_2\text{O}_3$, (b) relation between relative intensity RII of (100), (002), (101) planes for ZnO, spinel, and Y-compound and B_2O_3 content, (c) enlarged XRD pattern at 2θ at $34.7-34.8^\circ$, (d) relation between lattice constant c of ZnO grains and B_2O_3 content.

increasing amount of B_2O_3 . The addition of B reduced the number of spinel particles and affected the location of Co. Figure 6.1(d) shows the lattice constant c for a ZnO grain. The c value showed a complicated dependence on the amount of B_2O_3 and achieved a maximum at

0.75 mol%, decreased suddenly at 1 mol%, and then remained stable. The lattice constant $a = b$ showed the same tendency as c . The volume of the ZnO unit cell changed with addition of B_2O_3 , and this was thought to be caused by the substitution of Zn with other atoms, such as Co, Mn, Cr, and Ni, during sintering, with the greatest decrease in content of other atoms at 0.75 mol% B_2O_3 .

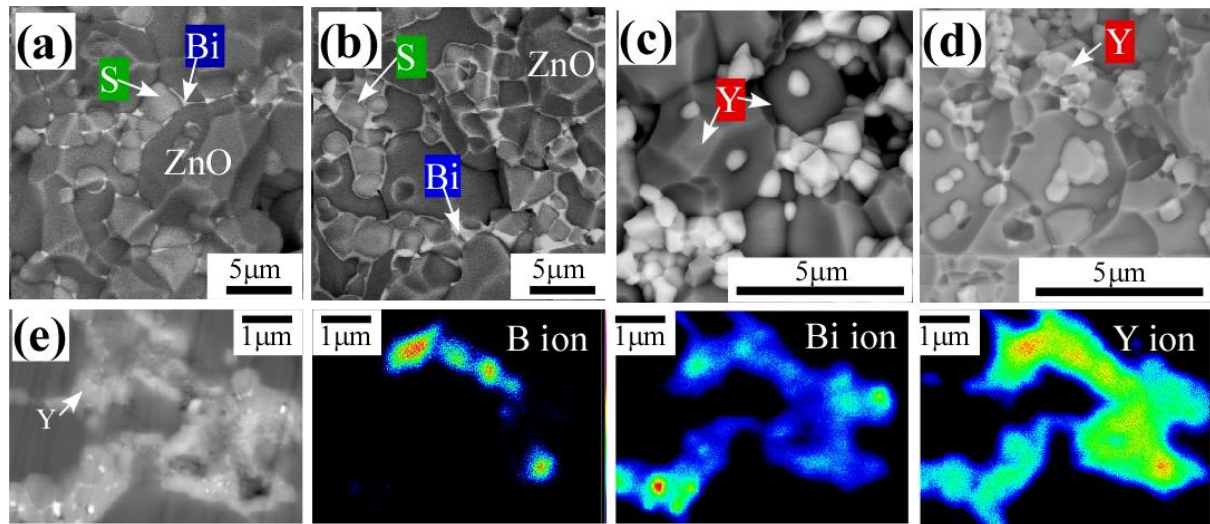


Figure 6.2 BSE images of microstructures changed by addition of B_2O_3 for: (a) Y0B0, (b) Y0B2.0, (c) Y2B0, (d) Y2B0.75, and (e) BSE with EPMA element mapping images of Y2B2.0. Bi: Bi_2O_3 , S: Spinel, Y: Y-compound.

Figure 6.2 shows BSE images for typical samples. Dark grey grains are ZnO, light grey grains are spinel particles, cubic white grains in Y2BX samples represent Y-compound, and the white layer at grain boundaries represents Bi_2O_3 . Figure 6.2(e) shows BSE images and elemental maps of Y2B2.0 obtained by EPMA. The white intergranular layer in samples without Y is the Bi_2O_3 layer, which was enriched and homogenized by adding B_2O_3 . For Y2BX samples, no obvious change in ZnO grain size was observed with increasing B_2O_3 content. However, a Bi-rich layer appeared in samples with a greater B_2O_3 content, shown as white dots at the boundaries of the Y-compound in the BSE image in Fig. 6.2(e), which were not β - Bi_2O_3 according to the XRD pattern. The EPMA results confirmed that most B was located in the Y-compound and partially located with Bi in the center of the Y-compound.

The microstructure at grain boundaries for samples with different amounts of Y or B were investigated by TEM combined with EDS, and the results are shown in Fig. 6.3. In general, the

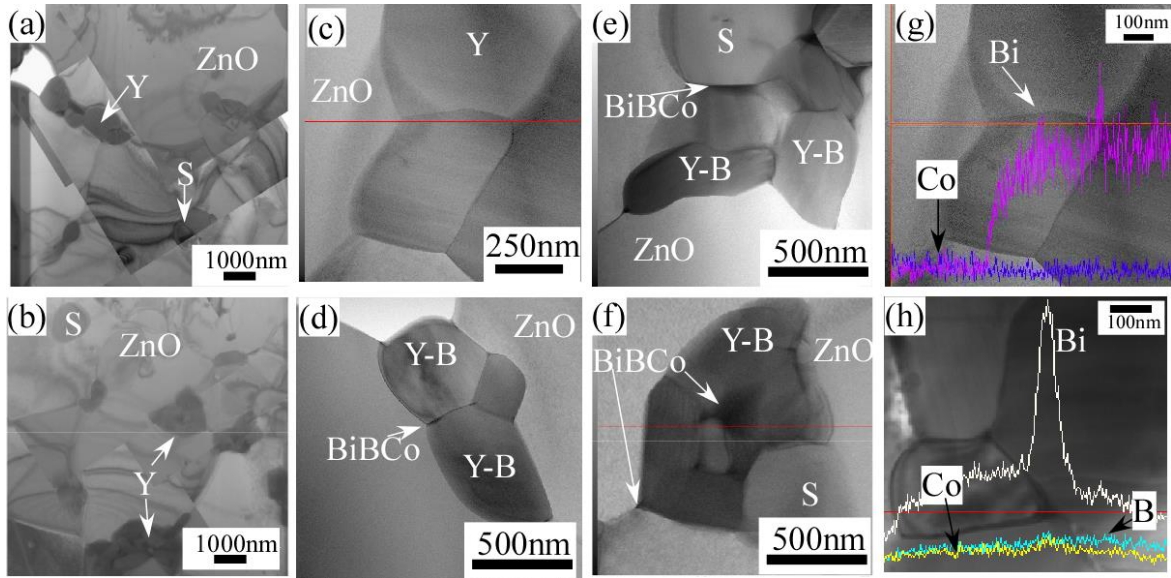


Figure 6.3 TEM images showing changes in microstructure with increasing B_2O_3 amount in Y_2BX samples, general images for (a) Y_2B_0 , and (b) $Y_2B_{2.0}$, grain boundary structure (c) Y_2B_0 , (d) $Y_2B_{0.75}$, (e) $Y_2B_{1.5}$, (f) $Y_2B_{2.0}$, and EDS line analysis of (g) Y_2B_0 , (h) $Y_2B_{1.0}$. Y: Y-compound, S: Spinel particles, Y-B: Y-compound containing B. BiBCo: amorphous Bi phase containing B and Co.

shape of the Y-compound changed from aligned to twinned with increasing X , as shown in Figs. 6.3(a) and (b). The results showed that no Bi-layer existed at grain boundaries in Y_2B_0 . The Bi existed in the Y-compound and its concentration increased towards the center. The microstructure changed when the amount of B_2O_3 was greater than 0.75 mol%, as shown in Figs. 6.3(d)–(f), and a very thin Bi-rich layer was observed at the ZnO/Y boundary. The amount of the Bi-rich phase increased with increasing B_2O_3 content, while the shape of the Y-compound became twinned and encircled the Bi-rich compound in the center. This Bi-rich layer was not Bi_2O_3 , but a glass phase contained B and Co, as shown in Fig. 6.3(h). The results showed that the Co in ZnO grains moved to the Y-compound and Bi-rich phase with increasing X . No change in the concentration of Mn and Cr in ZnO grains was observed, and Ni concentrations in the Y-compound and ZnO were similar upon adding B_2O_3 . For Y_2B_0 , as shown in Fig. 6.3(g), the Co concentration decreased in the order: $Co_{in\ spinel} > Co_{in\ ZnO} > Co_{in\ Y}$. However, for Y_2B_1 , as shown in Fig. 6.3(h), the Co and B concentration increased in the Bi-rich phase at the center of the Y-compound or at the Zn/Y boundary.

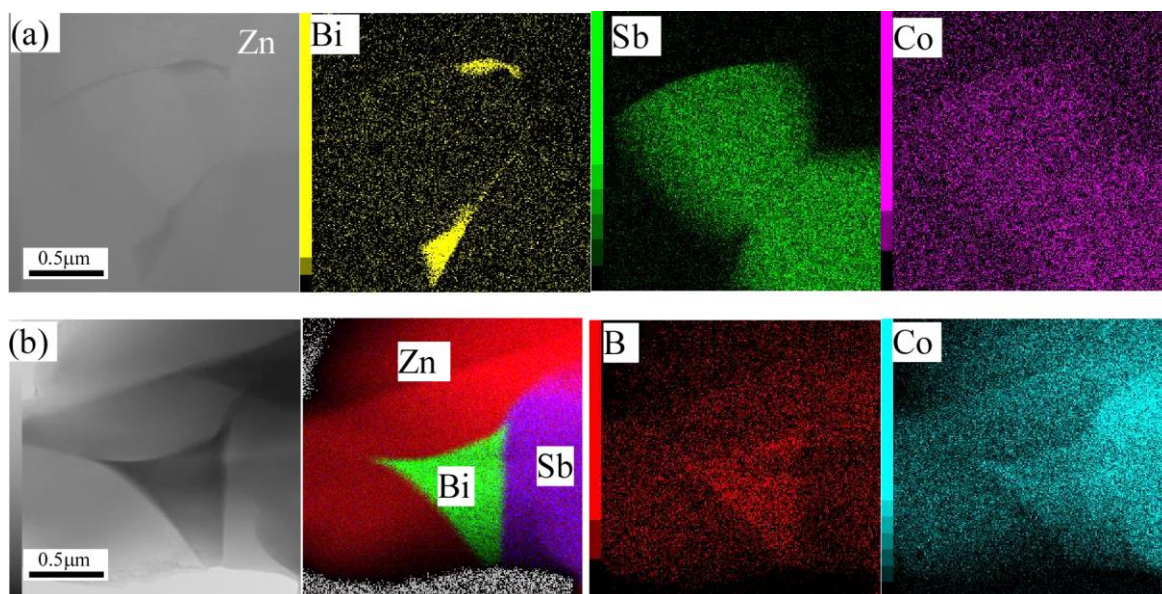


Figure 6.4 TEM images of (a) Y0B0 and (b) Y0B2.0, with EDS element mapping for Zn, Bi, Sb, Co, and B.

Figure 6.4 shows typical EDS element mapping results combined with TEM images of Y0B0 and Y0B2. Comparison of these two samples indicated that the B existed mainly in the Bi-rich phase at the triple point in Y0BX samples. For Y0B0, Co existed in the spinel, but no Co was found in the Bi-rich phase. However, for Y0B2, Co was observed in the Bi-rich phase at the triple point. The results of XRD and microstructure analyses indicate that, upon adding 0.75 mol% B₂O₃, the microstructure at grain boundaries changed dramatically, possibly because of a decrease in the melting point of the Bi-B-O glass phase compared to the melting point of Bi₂O₃^{19,20}. The decrease in Co concentration in ZnO caused an increase in the lattice constant in the ZnO grains, because the ionic radius of Co (≈ 0.061 nm) is smaller than that of Zn (≈ 0.074 nm), and the Co ions in ZnO moved to grain boundaries upon addition of B when no Bi-layer existed at the grain boundaries. Above 0.75 mol%, a Bi-B-O layer formed at grain boundaries and the movement of Co was likely blocked by this layer, so the lattice constant decreased again with increasing B₂O₃ content. In this case, excess B (ionic radius ≈ 0.027 nm) may then dissolve in the ZnO grains. The location of Co for different B₂O₃ contents may affect the donor density, Schottky barrier height, and electric properties, because Co acts as donor in the ZnO grains.

The grain size S_G was not significantly affected by increasing the amount of B₂O₃. The S_G value increased from 2.9 μm to 3.5 μm with an increase in X from 0 to 2 mol% for Y2BX

Chapter 6 Effects of B on Y-doped ZnO varistors

samples (see Table 6.1). For Y0BX samples, S_G increased from 3.9 to 4.8 μm with increasing X from 0 to 2 mol%, was shown in Table 6.2.

Table 6.1 Electrical properties of Y-doped varistors with various amounts of added B_2O_3 .

B_2O_3 X (mol%)	V_{NN} (V/mm)	S_G (μm)	α_{as}	α_{asMAX}	$J_{\text{L}30^\circ\text{C}}$ ($\mu\text{A}/\text{cm}^2$)	Φ_{B} (eV)	N_{D} (10^{17} cm^{-3})	N_{is0} (10^{12} cm^{-2})
0	1.05×10^3	2.9	29	34	1.7	1.27	2.00	3.08
0.25	0.82×10^3	3.9	25	28	3.7	1.17	1.79	2.80
0.5	0.81×10^3	3.3	28	30	3.7	1.33	1.42	2.66
0.75	0.90×10^3	3.5	28	39	0.8	1.15	1.59	2.63
1.0	0.90×10^3	3.3	26	30	10.4	1.35	1.24	2.51
1.25	0.84×10^3	3.4	30	35	1.2	1.40	1.42	2.73
1.5	0.81×10^3	3.2	32	42	1.0	1.57	1.82	3.27
2.0	1.00×10^3	3.4	31	34	0.3	1.48	2.01	3.34

Table 6.2 Electrical properties for Y0BX samples.

B_2O_3 X (mol%)	V_{NN} (V/mm)	S_G (μm)	α_{as}	$J_{\text{L}30^\circ\text{C}}$ ($\mu\text{A}/\text{cm}^2$)	Φ_{B} (eV)	N_{D} (10^{17} cm^{-3})	N_{is0} (10^{12} cm^{-2})
0	0.45×10^3	3.9	31	1.7	0.82	1.01	2.43
0.5	0.47×10^3	4.6	36	0.2	0.90	1.22	2.03
1.0	0.44×10^3	4.8	35	0.4	1.01	1.44	2.34
2.0	0.42×10^3	4.7	38	0.1	0.88	1.66	2.30

6.3 Effect of B₂O₃ additives on electrical properties

The $V_N - J$ characteristics before and after electrical degradation at 30°C and 130°C for some samples are shown in Fig. 6.5. The $V_N - J$ relation changed more sharply from the pre-breakdown to the breakdown region by addition of 0.75 mol% B₂O₃, as shown in Fig. 6.5(c), compared with the gradual rise shown in Figs. 6.5(a), (b), and (d). A similar tendency was observed for Y0BX samples as shown in Fig.6.6.

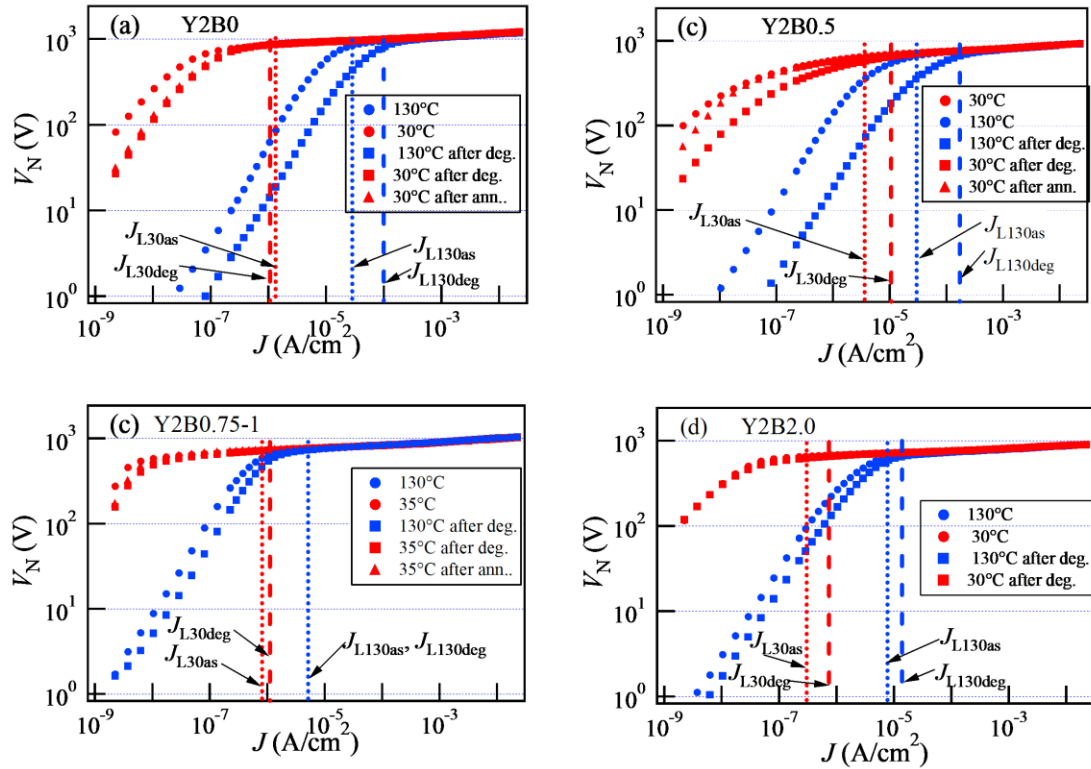


Figure 6.5 The $V_N - J$ characteristics before and after electrical degradation at 30°C and 130°C, after annealing at 200°C for Y2BX samples. (a) Y2B0, (b) Y2B0, (c) Y2B0.75, and (d) Y2B2.0.

The $V_N - J$ curves before and after degradation shifted to higher current density as shown in Figs. 6.5 (a) and (b), and $J_{L,deg}$ (both at 30°C and 130°C) increased after degradation. However, when the B₂O₃ content was greater than 0.75 mol%, this deterioration phenomenon suddenly disappeared, as shown in Fig. 6.5(c), which indicates that addition of the proper amount of B greatly increased the resistance to degradation in Y-doped varistors. Especially, Y2B0.75 samples showed excellent electrical properties compared to the others. This improvement in the electrical degradation resistance of B₂O₃ was not found for Y0BX samples or other Bi-based ZnO varistors without Y¹⁷ (Fig. 6.6).

Table 6.1 lists grain size S_G and electrical properties for all Y2BX samples with variable amounts of B_2O_3 ($0 \leq X \leq 2.0$ mol%). No apparent change in grain size was seen. Varistor voltage per 1 mm V_{NN} decreased abruptly from 1.05×10^3 to 0.82×10^3 V/mm at 0.5 mol% B_2O_3 , then increased to 0.90×10^3 V/mm as B_2O_3 amount was increased to 0.75 mol%, decreased to $0.81\text{--}0.84 \times 10^3$ V/mm at 1.25–1.5 mol% and then increased to 1.00×10^3 V/mm. This change in V_{NN} was attributed to the varistor voltage of single grain boundary V_{NNGB} and was considered $V_{NN} = V_{NNGB}/S_G$, because S_G was nearly constant. The nonlinear index values α_{as} near V_{NN} before degradation estimated in the breakdown region of current from 0.1 to 1 mA/cm² were nearly the same, and no apparent effects of addition of B_2O_3 were observed. In contrast, the maximum nonlinear index α_{asMAX} , which was estimated from $d \ln J / d \ln V_N$ over the entire range of the current density J , showed significant dependence on the amount of B_2O_3 . Though the leakage current density at 30°C $J_{L30^\circ C}$ showed small value at 0.75 and 2.0 mol% and a maximum at 1.0 mol%, no significant improvement upon addition of B_2O_3 was observed. However, leakage current density at 130°C $J_{L130^\circ C}$ for the Y2B0.75-1 sample decreased more than 6-fold before degradation, and more than 15-fold after degradation compared with those for the Y2B0 sample, as shown in Fig. 6.5.

Figure 6.7(a) shows the leakage current density – time ($J_{LD130^\circ C}(t) - t$) relation for Y2BX samples at 130°C. Starting value $J_{LD130^\circ C}(0)$ was minimum at $X = 0.75$ mol%. The $J_{LD130^\circ C}(t)$

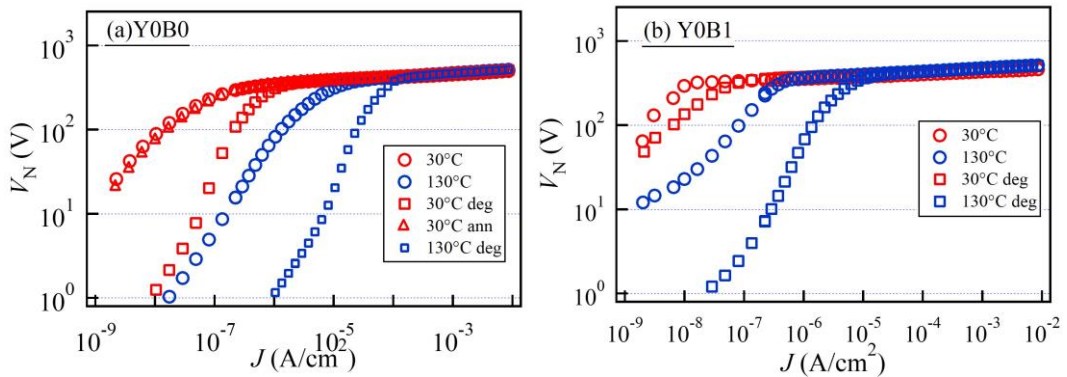


Figure 6.6 (a) The V – J characteristics before and after electrical degradation at 30°C and 130°C, after annealing at 200°C for (a) Y0B0 and (b) Y0B1.

– t relation for $X = 0.75, 1.5,$ and 2 mol% were flat, while the others increased with time. Among Y2BX samples, Y2B0.75 samples had the lowest leakage current density and the highest resistance of electrical degradation, *i.e.*, excellent long-term stability at 130°C. This result was reliable, because the $J_{LD130^\circ C}(t) - t$ relation for four samples was almost the same, as shown in Fig. 6.7(b).

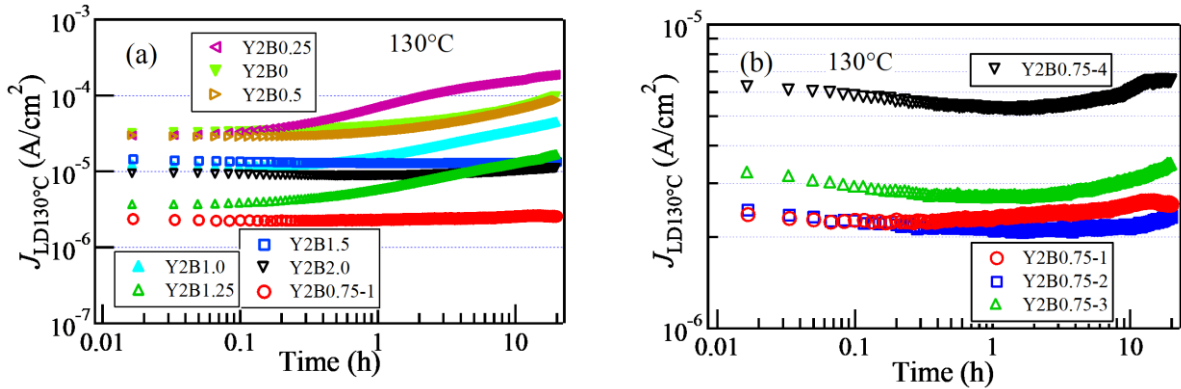


Figure 6.7 The $J_{LD130^\circ\text{C}}(t) - t$ relations for (a) Y2BX and (b) Y2B0.75.

Since the $V_N - J$ relationship after degradation was mostly recovered by annealing at 200 °C for all the samples prepared in this research in Fig. 6.5, it is suggested that the main factor for degradation is the migration of oxide and/or Zn^{2+} ions through the grain boundaries under the application of bias voltage. As discussed above, the change of microstructure at grain boundaries and improvement of degradation began at adding 0.75mol% B_2O_3 . Therefore, it is conjectured that the main reason for the improvement of electrical degradation by B_2O_3 addition is the blocking effect on ion migration of the Bi-rich phase containing B and Co (BiBO glass phase) at grain boundaries. Additionally, since the large amount of Bi_2O_3 layer in Y0BX samples prevented the formation of BiBO glass phase at grain boundaries, this blocking effect of B^{3+} was not observed. Therefore, adding B_2O_3 to the sample without Y did increase its resistance to degradation.

6.4 Thermal annealing effects

To understand how B_2O_3 improved electrical degradation, Y2BX was thermally annealed at 700°C for an hour in air. After electrical degradation, the $V - J$ curves in Figure 6.8 remain stable, which implies that the Y2B0 samples were significantly more resistant to degradation after annealing (compared to samples without annealing in Fig.6.5 (a)). During thermal annealing, crystal defects are reduced, which decreases interstitial ions¹⁴⁻¹⁶. Figure 6.9 shows that long-term stability of Y2BX was much improved by annealing treatment, since $J_{LD130^\circ\text{C}}(t)$ kept stable as the time increased. Starting value $J_{LD130^\circ\text{C}}(0)$ was the same as that of samples without

annealing treatment. Thermal annealing inhibits degradation but does not affect other properties, which supports the hypothesis that B^{3+} blocks ion migration.

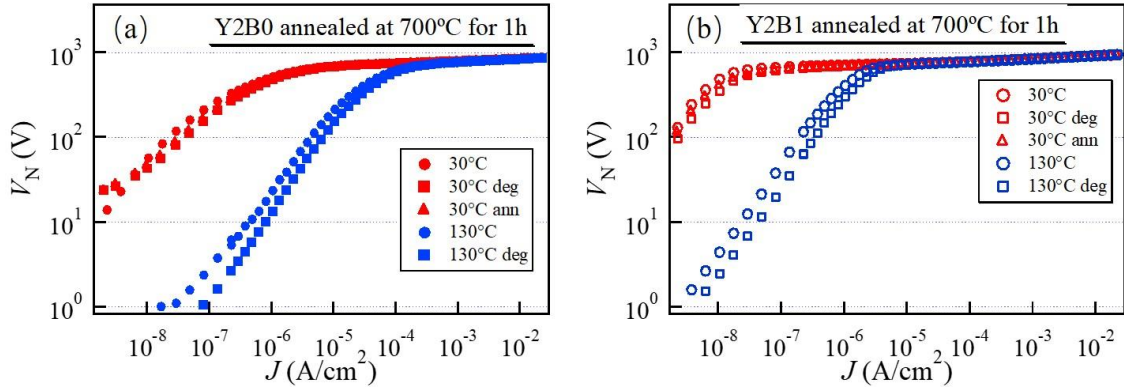


Figure 6.8 The $V_N - J$ characteristics before and after electrical degradation for Y2BX samples annealed at 700°C for 1 h. (a) Y2B0, (b) Y2B1.

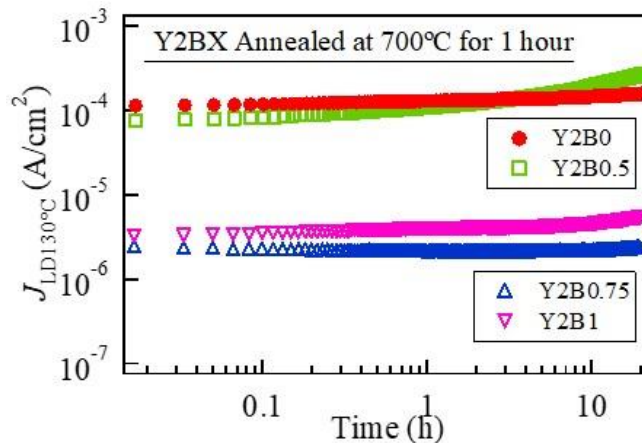


Figure 6.9 The $J_{LD130^\circ C}(t) - t$ relations for Y2BX annealed at 700°C for 1 h.

6.5 Analysis of interface states and double Schottky barriers

ICTS measurement were applied to the samples. The calculated values for each interface state level obtained by curve fitting using Eq. 4.7 in chapter 4 and assuming the existence of two types of interface state levels E_{IS1} and E_{IS2} , showed excellent agreement with the measured values for every Y2BX sample. The depth of each interface state level from E_C (the bottom of conduction band) $E_C - E_{IS1}$, $E_C - E_{IS2}$, and the distribution parameters β_1 and β_2 were estimated.

Pinning of Fermi level below $V_{GB} \leq V_{NNGB}$ was confirmed and valid values of Φ_{B0} , N_D , and N_{IS0} were obtained⁴, as discussed in chapter 5.

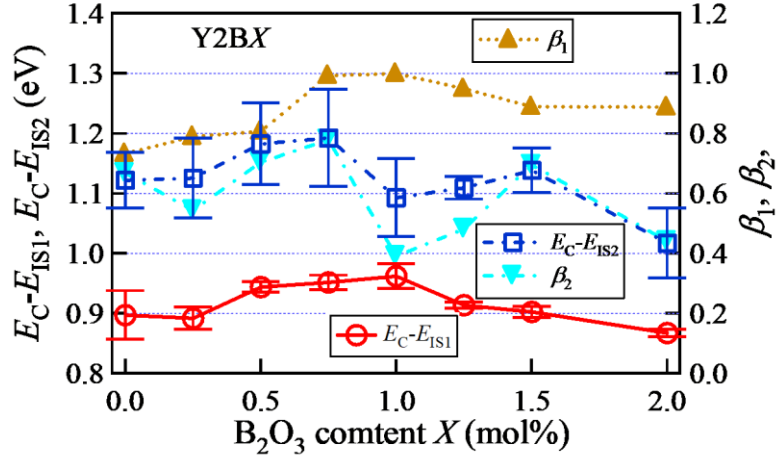


Figure 6.10 $E_C - E_{IS1}$ and $E_C - E_{IS2}$, β_1 and β_2 for Y2BX samples.

Figure 6.10 shows $E_C - E_{IS1}$, $E_C - E_{IS2}$, β_1 , and β_2 at 100°C for Y2BX samples. Results showed that $E_C - E_{IS1}$, β_1 for the interface state 1 (shallower level), and $E_C - E_{IS2}$, β_2 for 2 (deeper level), had significant correlativity for all samples. The results also suggested that the long-term stability of the leakage current at 130°C was high (Fig. 6.7) when the depth and values of both $E_C - E_{IS2}$ and β_2 were deep and large, respectively, for the samples with $X \leq 1.5$. For Y2BX samples, EPMA revealed that B was located mainly in the Y-compound, and the glass phase for BiBO appeared at ZnO grain boundaries with increasing amounts of B_2O_3 . Upon addition of an optimal amount of B_2O_3 , formation of glass phase BiBO at grain boundaries changed the interface structure, narrowed the distribution of shallower interface state, increased the rate of change of current density around the region between the pre-breakdown and breakdown regions in $V_N - J$ relation (sharper curve), and decreased leakage current due to an increase in captured electrons. However, excessive formation of BiBO at the center of the Y-compound may have had negative effects on electrical properties.

We have proposed a simulation on ZnO varistors' electrical properties according to thermionic emission mechanism in chapter 5. The relation between applied bias voltage V_{GB} and barrier height $\Phi_B(V_{GB})$ under bias voltage V_{GB} is given by Eq. 6.1^{21, 26}:

$$\left(\frac{\varepsilon\varepsilon_0 N_D}{2}\right)^{\frac{1}{2}} \left[\left(\Phi_B(V_{GB})\right)^{\frac{1}{2}} + \left(\Phi_B(V_{GB}) + eV_{GB}\right)^{\frac{1}{2}} \right] = eN_{IS}(V_{GB}) \equiv eN_{IS0}S(V_{GB}) \quad (6.1)$$

where $S(V_{GB})$ is the increase in the ratio of interface state density occupied by electrons under bias V_{GB} and $S(V_{GB})$ represents maximum S_{MAX} at $V_{GB} \approx V_{NNGB}$ due to filling of the interface states. The ICTS results confirm that the Fermi level is pinned at the interface state level by application of V_{GB} ($< V_{NNGB}$), since $\Phi_B(V_{GB})$ is nearly equal to Φ_{B0} at $V_{GB} \leq V_{NNGB}$ ²⁰. As discussed in chapter 5, equation 6.1 was modified at $V_{GB} \approx V_{NNGB}$ as²¹ to:

$$V_{NNGB} \approx 4\Phi_{B0} S_{MAX} (S_{MAX} - 1) \quad (6.2)$$

where V_{NNGB} is the product of Φ_{B0} and $S_{MAX}(S_{MAX}-1)$. Because the values of V_{NNGB} and Φ_{B0} are known, S_{MAX} can be estimated using Eq. 6.1.

Figure 6.11(a) shows N_D and N_{IS0}^2 at 100°C for Y2BX and Y0BX samples with various B₂O₃ contents. The N_D and N_{IS0} values were not affected significantly by temperature. Therefore, the data for N_D and N_{IS0} at 100°C were used, because it was the lowest temperature at which stable measurements could be obtained. Although the values of N_D for the Y2BX and Y0BX samples were nearly the same for different X values, the values of N_{IS0} for Y2BX were larger than those for Y0BX. The N_D value strongly correlated with N_{IS0}^2 . When X increased, both N_D and N_{IS0}^2 decreased to a minimum, and then monotonically increased. Both samples with or without Y showed the same N_D and N_{IS0}^2 dependence on X . However, the minimum value of X for N_D and N_{IS0}^2 for Y2BX was ≈ 1 mol%, which was larger than that for Y0BX. Both N_D and N_{IS0}^2 for Y2BX after the minimum increased more rapidly compared with that for Y0BX.

Figure 6.11 (b) shows the relations between N_D , Φ_B , lattice constant c of ZnO grains, and B₂O₃ content. Both the N_D and Φ_B values correlated strongly with the c value for all B₂O₃ contents. When a small X that did not exceed the Bi₂O₃ content was added, the Co, which acts as a donor in ZnO grains, moved from ZnO grains to the Y-compound and Bi-rich phase with increasing X , as described in section 6.2. As a result, N_D decreased and c increased. When a larger X that exceeded the Bi₂O₃ content was added, some Co remained in ZnO grains, causing an increase in N_D and a decrease in c . In this case, excess B ions may dissolve in the ZnO grains and act as donors there.

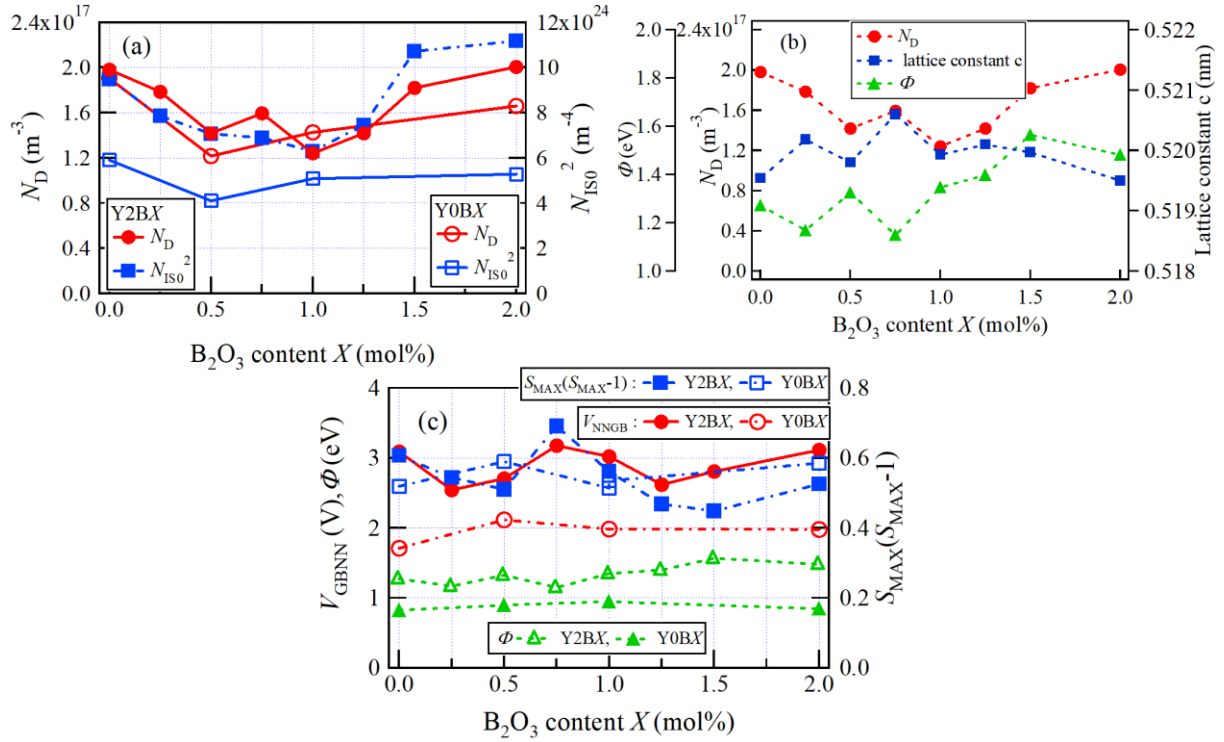


Figure 6.11 Relation between B_2O_3 content and (a) N_D and N_{IS0}^2 , (b) N_D , Φ_B , and lattice constant c of ZnO grain for Y2BX samples, (c) V_{NNGB} , Φ_B , and $S_{MAX}(S_{MAX}-1)$ for Y2BX and Y0BX samples.

Figure 6.11 (c) shows values of Φ_{B0} , V_{NNGB} , and $S_{MAX}(1-S_{MAX})$ at $100^\circ C$ for Y2BX and Y0BX samples for various X values. Although Φ_{B0} for Y0BX samples was nearly constant at ≈ 0.9 eV from 0 to 2 mol% X , Φ_{B0} for Y2BX samples was ≈ 1.5 times greater than that for the Y0BX sample, showed a minimum at ≈ 0.75 mol%, and then increased slightly with X . This suggests that the increase in Φ_{B0} is related to the deeper interface state levels and larger capture cross-sections due to changes in the microstructure at the grain boundaries. The main factor causing the increase in V_{NNGB} due to Y doping and a reduction in ZnO grain size S_G has been discussed to be the increase in S_{MAX} in chapter 5. The change in V_{NNGB} was similar to the change in the product of S_{MAX} and $(S_{MAX}-1)$, when X was varied. The results revealed that addition of B_2O_3 did not change Φ_{B0} , but did change S_{MAX} significantly, which indicates that V_{NNGB} was related mainly to the ratio of empty interface states to N_{IS0} under zero bias for Y-doped samples. However, no apparent correlation between V_{NNGB} and S_{MAX} , or between V_{NNGB} and Φ_{B0} , was observed for samples without Y.

6.6 An analytical method for conducting processes of ZnO varistors

The nonlinear $V_N - J$ relation for the samples prepared in this study were modified notably by addition of B_2O_3 , as shown in Fig. 6.5. A detailed analysis of the nonlinear $V_N - J$ relation

was performed to investigate the effects of addition of B₂O₃. The nonlinear $V_N - J$ relation is considered to be divided into three regions: pre-breakdown, nonlinear, and upturn. Although in the small current density region, where upturn regions disappeared, the $V_N - J$ relation resembled the $p-n$ junction diode given by ²⁵:

$$J = J_0 \left[\exp\left(\frac{eV_N}{n_N k_B T}\right) - 1 \right], \quad (6.3)$$

where J_0 is saturation current density, n_N is a constant, k_B is the Boltzmann constant, and T is absolute temperature. The $V_N - J$ relation of ZnO varistors disagrees with Eq. 6.3 due to the existence of the interface states at ZnO grain boundaries. There are two effective junctions $/_1$ and $/_2$ for the ZnO $/_1$ interface of the region $/_2$ ZnO. At a grain boundary, two back-to-back Schottky barriers formed. The energy band near a grain boundary under bias can be divided roughly into three regions: I, II, and III ²⁶. The forward-biased Schottky barrier is assumed to form in region I and the reverse-biased one in region III. Region II is the interface between I and III where the interface states are formed. Therefore, because current must pass through the resistance of a ZnO grain, total resistance is the series connection of the resistance corresponding to each region. The most curious point about the $V_N - J$ relation is that the $V_N - J$ relation at the high current side in the breakdown region barely changed before and after electrical degradation or upon changing sample temperature (Fig. 6.5), although the sum of the voltage drop of each region corresponded to V_N . The reason for this was not clarified. However, the sum of the voltage drop of each region corresponded to V_N . Thus, in this study, separation of the $V_N - J$ relation of ZnO varistors was attempted by analyzing the J -dependent differential resistivity $R_D(J) = dV_N / dJ$ to investigate the effects of B₂O₃, because the $R_D(J) - J$ relation can be used to evaluate the effects of B₂O₃ addition more sensitively compared with the $V_N - J$ relation (Fig. 6.5).

The conduction process for ZnO varistors has been reported to consist of thermionic emission, thermally assisted field emission, and field emission in regions I and III, Frenkel Poole emission, tunneling, and thermally activated hopping in region II ²⁶. However, separating each conduction process from the $V_N - J$ relation is difficult.

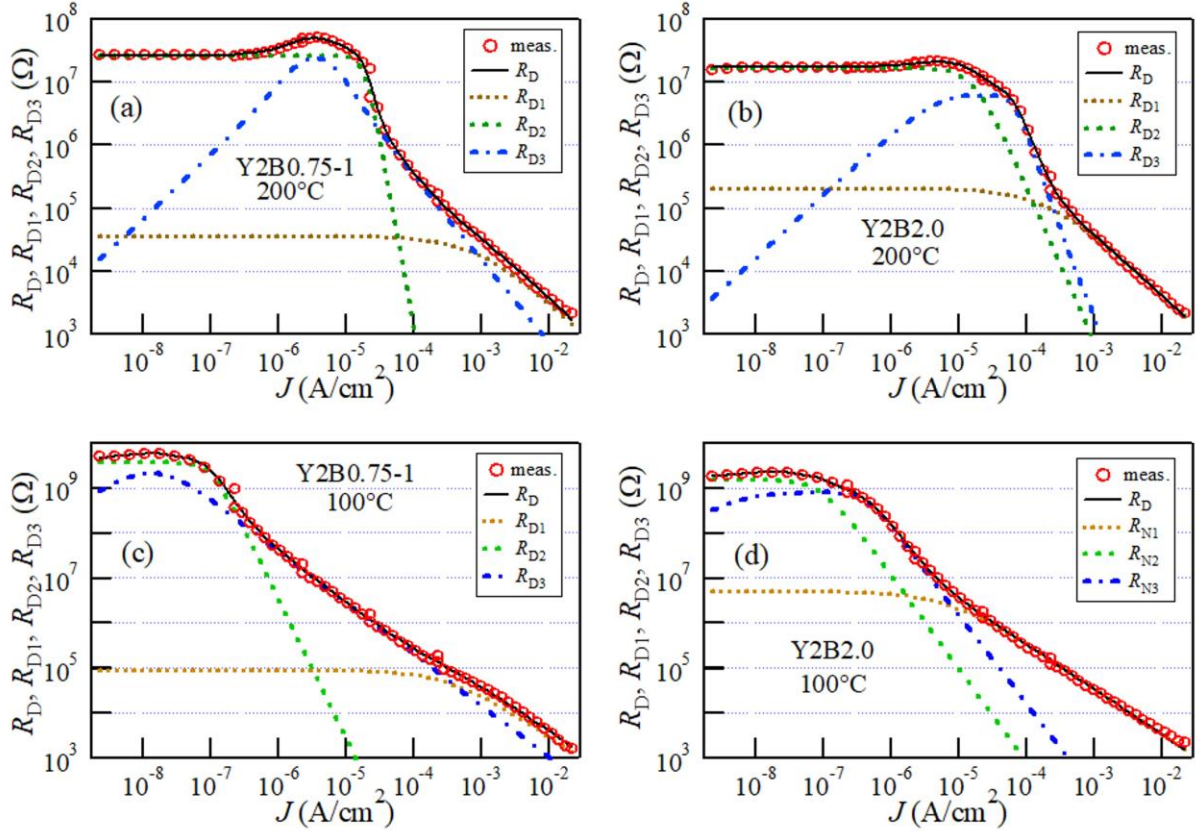


Figure 6.12 Measured and fitted R_D , R_{D1} , R_{D2} , and R_{D3} for Y2B0.75 and Y2B2.0 at 200 and 100°C.

Plots in Fig. 6.12 (a)-(d) show experimental R_D for Y2B0.75 and Y2B2.0 samples at 200 and 100°C. Figure 6.12 (a) and (b) show that, for the $R_D - J$ relation, R_D is constant in the low J region, increases suddenly at a certain current density, and decreases rapidly after reaching the maximum. Such a prominent maximum was not seen at temperatures lower than $\approx 100^\circ\text{C}$, as shown in Fig. 6.12 (c) and (d).

The prominent difference in the two $R_D - J$ relations is the shape around the maximum. The $R_D - J$ relation fit Eq. 6.4 using the sum of three differential resistance R_{D1} , R_{D2} , and R_{D3} .

$$R_D = \frac{dV_N}{dJ} = \frac{d}{dJ}(V_{N1} + V_{N2} + V_{N3}) = R_{D1} + R_{D2} + R_{D3} \quad (6.4)$$

where V_{N1} , V_{N2} , and V_{N3} are the voltages corresponding to R_{D1} , R_{D2} , and R_{D3} , respectively, as represented by the following:

$$R_{D1} = \frac{A_1}{1 + (B_1 J)^i} \quad (6.5)$$

$$R_{D2} = \frac{A_2}{1 + (B_2 J)^i} \quad (6.6)$$

$$R_{D3} = \frac{A_3}{1 + \frac{[B_3(J - C_3)]^{i_3}}{J}} \quad (6.7)$$

where parameters $A_1, B_1, A_2, B_2, A_3, B_3,$ and C_3 (fitting parameters) are constants dependent on T . Indexes $i_1, i_2,$ and i_3 also are dependent on T . The R_{D1} and R_{D2} values were constant in the low J region and decreased suddenly near $J = \approx B_1^{-1}$ and $\approx B_2^{-1}$ (A/cm^2), respectively. The R_{D3} value reached a maximum sharply near $J = C_3$ (A/cm^2). Solid and dashed lines in Fig. 6.12 (a) and (b) represent the fitted curves calculated using Eqs. 6.4–7 for Y2B0.75 and Y2B2.0 samples, respectively, at 200°C. The fitted curve agreed well with R_D calculated from the measured $V_N - J$ relation for all samples.

Two types of contributions of R_{D2} and R_{D3} to R_D were observed and differed prominently around the maximum R_D . The shape of the tip of the peak of R_{D3} for Y2B2.0 [Fig. 6.12 (b)] is more gently sloping and the J values giving the maximum of R_D and R_{D3} are not the same as those for Y2B0.75 [Fig. 6.12 (a)]. All fitting parameters were determined uniquely at temperatures above $\approx 100^\circ C$ where the effective contribution of $R_{D1}, R_{D2},$ and R_{D3} to R_D appeared. Values of $A_1, B_1, A_2,$ and B_2 were determined at temperatures below $\approx 100^\circ C$.

Both R_{D1} and R_{D2} were bent at $J = J_{b1}$ and J_{b2} (A/cm^2), respectively, as shown in Fig. 6.12. Therefore, rough values of fitting parameters B_1 and A_1 for R_{D1} were estimated to be $\approx J_{b1}^{-1}$ and $R_{D1}(J_{b1})$, respectively [e.g., $J_{b1} \approx 2 \times 10^{-4} A/cm^2$ and $R_{D1}(J_b) \approx 4 \times 10^5 \Omega$, below J_b for the Y2B2.0 sample, as shown in Fig. 6.12 (b)]. Similarly, values of B_2 and A_2 for R_{D2} were estimated to be $\approx J_{b2}^{-1}$, where R_D is bent in the middle J region, and be $\approx R_{D2}(J_{b2})$ [e.g., $J_{b2} \approx 2 \times 10^{-5} A/cm^2$ and $R_{D2}(J_{b2}) \approx 2.5 \times 10^7 \Omega$ below J_{b2} for the Y2B0.75 sample, as shown in Fig. 6.12 (a)]. Values of parameters B_2 and A_2 could be determined uniquely when J independent of R_{D2} was observed in the lower J region. Index i_1 was fixed at 1 over the entire measuring temperature region between 30–200°C, because the fitted value was $\approx 0.93 - \approx 1$. Furthermore, because the value of R_{D1} was relatively small in the low J region, but was larger than those of R_{D2} and R_{D3} in the high J region after the breakdown over all measuring temperatures, the value of R_{D1} represents differential resistance in forward region I and may be dominated by the thermionic emission mechanism.

Determining values of the parameters $A_3, B_3,$ and C_3 at low temperatures was difficult because the R_{D3} peak was not observed there. And because C_3 corresponded to J near the R_{D3} peak and was less than the lower limit of measuring current density at low temperatures,

determining the value of C_3 there was impossible. However, because $A_2 -$, $B_2 -$, $A_3 -$, $B_3 -$, and $C_3 - 1 / T$ relations obeyed the Arrhenius equation at temperatures above 130°C , the value of C_3 was fixed to the value estimated from the Arrhenius equation at lower temperatures. Finally, fitting parameters A_2 , B_2 , A_3 , B_3 , and C_3 obeyed the Arrhenius equation at temperatures below 130°C , as shown in Fig. 6.13. In contrast, $A_1 -$ and $B_1 - 1 / T$ relations for samples did not obey the Arrhenius equation, except for those of Y2B2.0. Activation energies for $A_2 -$, $B_2 -$, $A_3 -$, $B_3 -$, and $C_3 - 1 / T$ relations were ≈ 0.7 eV, nearly the same as shown in Fig. 6.13(a). As a result, the ratios of A_1 to B_1 , A_2 to B_2 , and A_3 to B_3 were very similar.

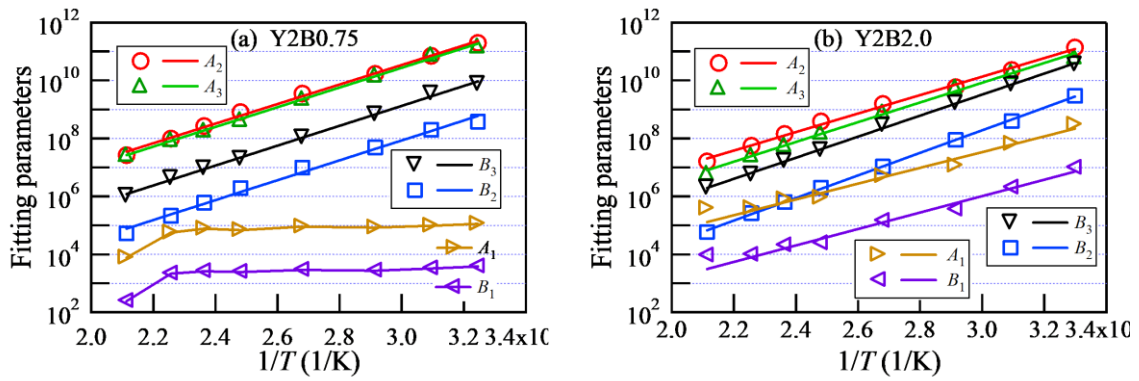


Figure 6.13 Arrhenius plots of fitting parameters for R_{N1-} , R_{N2-} and $R_{N3} - J$ relations for (a) Y2B0.75-1 and (b) Y2B2.0 at $30-200^\circ\text{C}$.

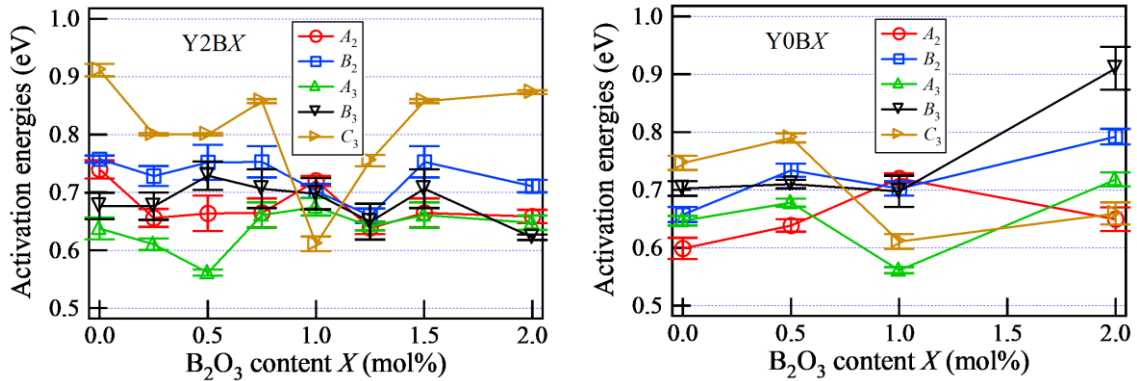


Figure 6.14 Activation energies for $A_2 -$, $B_2 -$, $A_3 -$, $B_3 -$, and $C_3 - 1 / T$ relations for Y2BX and Y0BX.

Furthermore, because those activation energies were nearly the same as those for Y0BX [Fig. 6.14 (b)], the activation energy for fitting parameters was not related to addition of Y.

Plots and lines shown in Fig. 6.15(a) and (b) represent measured and calculated curves of V_N , V_{N1-} , V_{N2} , and V_{N3} obtained by numerically integrating $R_D -$, R_{D1-} , R_{D2-} , and $R_{D3} - J$ for the Y2B0.75 and Y2B2.0 samples, respectively. The constant of integration, which is equal to the

difference between the measured and calculated values of V_N , was added to V_{N2} . The calculated values of V_N agreed with the measured values at all temperatures. The ratios of the contribution of V_{N1} , V_{N2} , and V_{N3} to V_N were nearly the same, except for the Y2B2.0 sample in the large J region, because the V_{N1-} , V_{N2-} , or V_{N3-} relations at all measuring temperatures were similar there. For Y2B2.0 sample, although V_{N1} and V_{N2} was varied especially when the temperature was changed, the sum of V_{N1} and V_{N2} was almost the same. The mechanism of this result is not yet understood. Because the fitting parameters were determined from the $V_N - J$ relation, including a pre-breakdown region, and the V_{N1} , V_{N2} , and V_{N3} in the high J breakdown region at all measured temperatures didn't show a large deviation, dividing V_N into V_{N1} , V_{N2} , and V_{N3} is meaningful.

The R_{D1} value provided by

$$R_{D1} = \frac{A_1}{1 + B_1 J} = \frac{dV_{N1}}{dJ} \quad (6.8)$$

leads to

$$J = \frac{1}{B_1} \left[\exp\left(\frac{B_1}{A_1} V_{N1}\right) - 1 \right] = \frac{1}{B_1} \left[\exp\left(\frac{B_1}{A_1} N_{GB} V_{GBI}\right) - 1 \right], \quad (6.9)$$

where V_{GBI} is bias voltage per grain boundary applied to region I. Because Eq. 6.9 has the same form as diode current equation Eq. 6.3, A_1 and B_1 were attributed to $A_1 = nk_B T / (J_0 e)$ and $B_1 = 1/J_0$. In this case, Eq. 6.9 is expressed as

$$J = J_0 \left[\exp\left(\frac{eV_N}{n k_B T}\right) - 1 \right] = J_0 \left[\exp\left(\frac{eN_{GB} V_{GB}}{N_{GB} n k_B T}\right) - 1 \right] = J_0 \left[\exp\left(\frac{eV_{GB}}{n k_B T}\right) - 1 \right], \quad (6.10)$$

where n corresponds to the ideality coefficient and lies between 1 and 2 for the general p-n junction and Schottky diodes. The equation that applies for R_{D1} corresponding to the thermionic emission mechanism in region I under forward-bias is represented by:

$$J_0 = A^* T^2 \exp\left(-\frac{E_B}{k_B T}\right) \quad (6.11)$$

where A^* is Richardson constant and E_B is the energy with respect to the Fermi level E_{FG} for ZnO grain in region II and expressed as $E_B = \Phi_{B0} + E_c - E_{FG}$ for $V_{GB} \leq V_{NNGB}$ ⁹. The A_1- and $B_1- 1/T$ relations did not obey the Arrhenius equation for any samples except those of the Y2B2.0 sample. However, the relation for the Y2B2.0 sample did obey the Arrhenius equation, with an activation energy E_B for the Y2B2.0 sample of ≈ 0.6 eV. The E_B was near the value

reported for the sample without Y²⁷. However, for Y2BX samples, E_B was larger than $\Phi_{B0} \geq 1.16$ eV, as shown in Table 6.1. These results are not yet understood.

Figure 6.16 shows the temperature dependence of coefficient n for Y2BX ($X=0-2$) samples. Values of n were nearly the same for all samples, although they were larger than that for the p-n junction and Schottky diodes ($1 \leq n \leq 2$). In contrast, values of n were $1 \leq n \leq 2$ for some Y0BX samples. Therefore, coefficient n has significant meaning in region I.

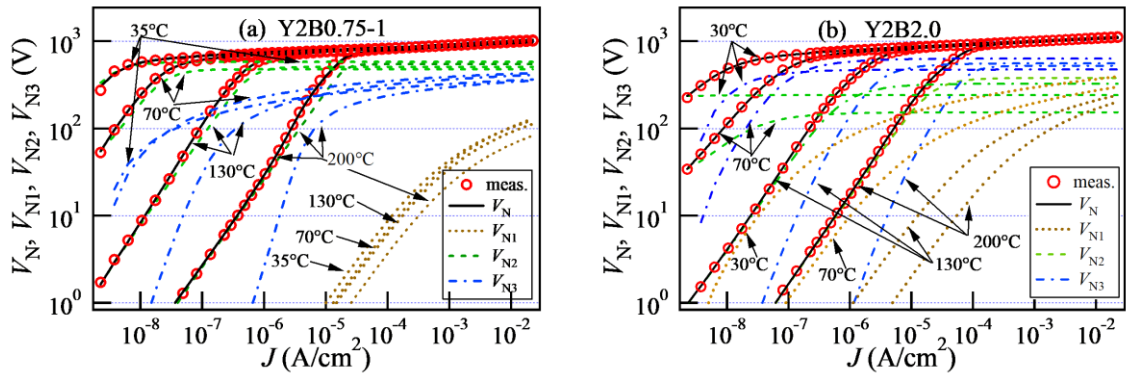


Figure 6.15 V_{N-} , V_{N1-} , V_{N2-} and $V_{N3-} - J$ relations obtained by numerical integration of R_{DN-} , R_{D1-} , R_{D2-} and $R_{D3-} - J$ relations for Y2B0.75-1 and Y2B2.0 at 30–200°C.

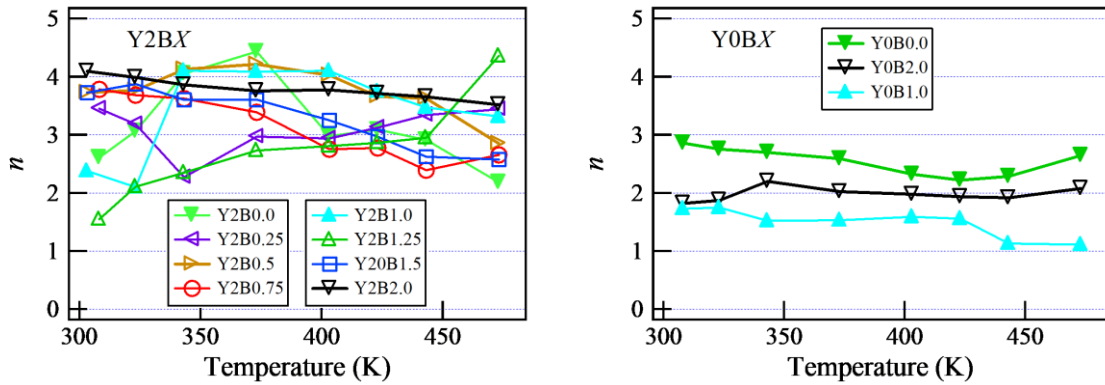


Figure 6.16 Temperature dependence of coefficient n for Y2BX ($X=0-2$) samples.

Obtaining the analytical formulae of V_{N2-} and $V_{N3-} - J$ relations for arbitrary values of indexes i_2 and i_3 was not possible. However, the analytical formulae of the $V_{N2-} - J$ relation could be obtained for $i_2 = 1, 2$, and 4. The analytical formulae of V_{N2} for $i_2=1$ is represented by Eq. 6.9. For $i_2 = 2$,

$$V_{N2} = \frac{A_2}{B_2} \tan^{-1}(B_2 J) \quad (6.12)$$

and V_{N2} becomes almost constant when $V_{N2} B_2/A_2 \approx \pi/2$. The analytical formulae of $V_{N3} - J$ relation can be obtained for $i_3 = 1, 2, 3, \dots$. The analytical formula for $i_3 = 1$ is

$$V_{N3} = \frac{A_3}{2B_3} \left\{ \ln \left[B_3 J^2 + aJ + B_3 C_3^2 \right] - 2 \frac{a}{b} \tan^{-1} \left[\frac{a + 2B_3 J}{b} \right] \right\} - \frac{A_3}{2B_3} \left[\ln(B_3 C_3^2) - 2 \frac{a}{b} \tan^{-1} \left(\frac{a}{b} \right) \right], \quad (6.13)$$

where $a = 1 - 2B_3 C_3$ and $b = (4B_3 C_3 - 1)^{0.5}$. Lines in Fig. 6.17 (a) and (b) represent examples of $V_{N2} - J$ and $V_{N3} - J$ relations obtained by numerical integration of $R_{D2} - J$ and $R_{D3} - J$ relations using fitting parameters $A_2, B_2, A_3, B_3,$ and C_3 and $0.5 \leq i_2, i_3 \leq 5$ for Y2B0.75 at 35°C, respectively. The $V_{N2} - J$ and $V_{N3} - J$ relations became flat for $i_2 \geq \approx 1.5$ and $i_3 \geq \approx 1.25$ above $J \approx 1 \times 10^{-7} \text{ A/cm}^2$, respectively, and as a result, nonlinearity index α_{as} increased for small V_{N1} . Behavior of the $V_{N2} - J$ relations was similar to that of the Zener breakdown in the reverse biased region.

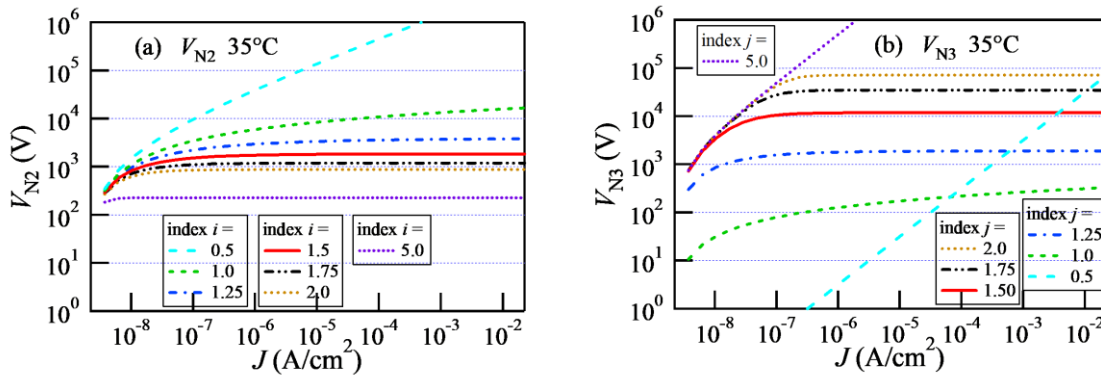


Figure 6.17 $V_{N2} - J$ and $V_{N3} - J$ relations obtained by numerical integration of (a) $R_{D2} - J$, and (b) $R_{D3} - J$ relations calculated fitting parameters for Y2B0.75 at 35°C.

Figure 6.18 shows the fitted values of i_2 and i_3 for each Y2BX sample at 30–200°C. Only Y2B2.0 had values of i_2 and i_3 that satisfied the conditions of both $i_2 \geq \approx 1.5$ and $i_3 \geq \approx 1.25$ near room temperature. However, because both R_{D1} and V_{N1} for the Y2B2.0 sample were large in Fig. 6.12(b), V_N is strongly dependent on J in the high J breakdown region, and the value of α_{as} becomes small.

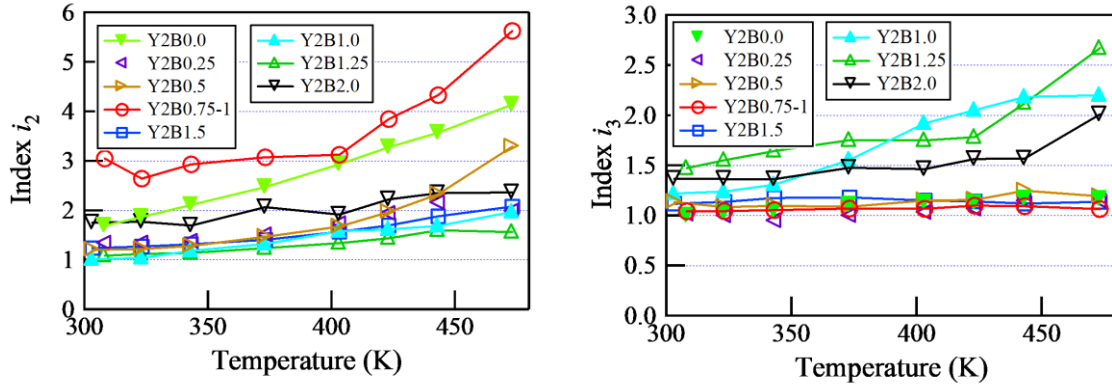


Figure 6.18 Temperature dependence of indexes (a) i_2 and (b) i_3 for Y2BX ($X = 0-2$) samples.

Figure 6.19 shows the relation between measured values of α_{asMAX} and indexes i_2 and i_3 for each Y2BX sample at 30 – 35°C. Results revealed that i_2 was strongly correlated with α_{asMAX} . Because the value of i_2 at $\approx 30^\circ\text{C}$ for the Y2B1.0 sample was ≈ 1 , V_2 it could be estimated by a formula similar to Eq. 6.9. The value of $eS_{GA_2} / B_2 / k_B / T$ corresponding to n was ≈ 4.6 (see Fig. 6.16) and the activation energy was ≈ 0.70 eV, as shown in Fig. 6.14. The value of V_N in the pre-breakdown region fit well using V_{N2} , as shown in Fig. 6.15. If V_{N2} originated from the thermionic emission mechanism, E_B is equal to the activation energy ≈ 0.7 eV for A_2 , as shown in Fig. 6.14 (a). However, this value is smaller than Φ_{B0} . If this is ignored, the conduction process corresponding to V_2 includes the thermionic emission process.

Among Y2BX samples, Y2B0.75 had the lowest leakage current density and excellent long-term stability; a result that was robust. Figure 6.20(a) and (b) show the temperature dependence of indexes i_2 and i_3 for the four Y2B0.75 samples corresponding to the $J_{LD130^\circ\text{C}}(t) - t$ relations shown in Fig. 6.7(b). The value of i_3 for the Y2B0.75-1, 2, 3 samples was ≈ 1 and was independent of temperature; while that for the Y2B0.75-4 sample was a little larger than 1 at temperatures above 100°C. The value of i_2 for the Y2B0.75-2 sample was largest, which had the smallest leakage current density and excellent long-term stability; and for the Y2B0.75-4 sample was smallest, which had the largest leakage current density. These results suggest that the index i_2 is correlated significantly with deeper interface state level 2. Confirmation of this result requires additional research.

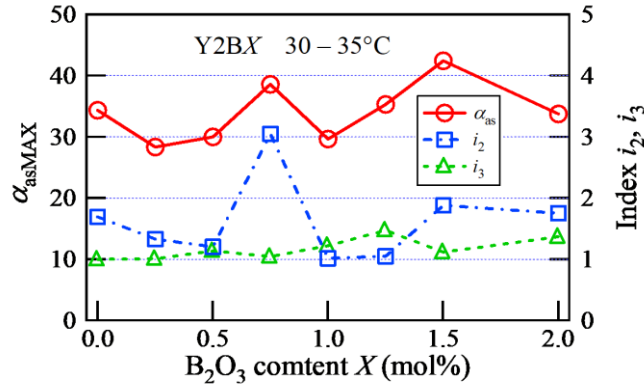


Figure 6.19 Relation between α_{asMAX} and i_2, i_3 at 30–35°C for Y2BX ($X=0-2$) samples.

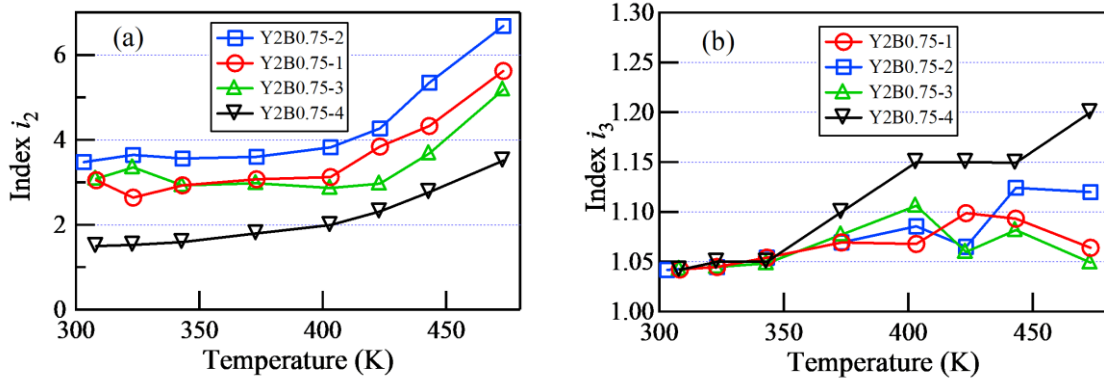


Figure 6.20 Temperature dependence of indexes i_2 and i_3 for four Y2B0.75 samples.

Figure 6.21(a) shows the relation between varistor voltage per on grain V_{NNGB} and V_{1GB} , V_{2GB} , and V_{3GB} per on grain for Y2BX samples. Results revealed that V_{NNGB} correlated strongly with V_{3GB} . The values shifted V_{3GB} by +2V and roughly agreed with V_{NNGB} , which suggests that V_{NNGB} is the value by which V_{3GB} was added to the base voltage of ≈ 2 V. The Y0BX samples showed the same tendency and the base voltage was ≈ 1.4 V. The difference in the base voltages for Y2BX and Y0BX samples was ≈ 0.6 V, caused mainly by the difference in the barrier height, as shown in Fig. 6.11. Total voltage drops V_N can be divided into the voltage drop caused by three conduction processes, although it seems that V_{N3} is artificial. However, V_{N3} is necessary to completely explain the differential resistance. At the present stage, V_{N1} and V_{N2} are not declared to correspond to the voltage drop due to the conduction process of thermionic emission mechanism in region I forward biased and region III reverse-biased, respectively. However, the conduction process corresponding to V_{N3} is indefinite. This analysis is suggested for devices such as other types of ZnO varistors, TiO_2 varistors, and SnO_2 varistors, and may also be suitable for avalanche diodes or heterojunctions, especially because the equation for

R_{D3} may result from the tunneling effect. Future studies will be conducted to investigate applications of the analytical equations.

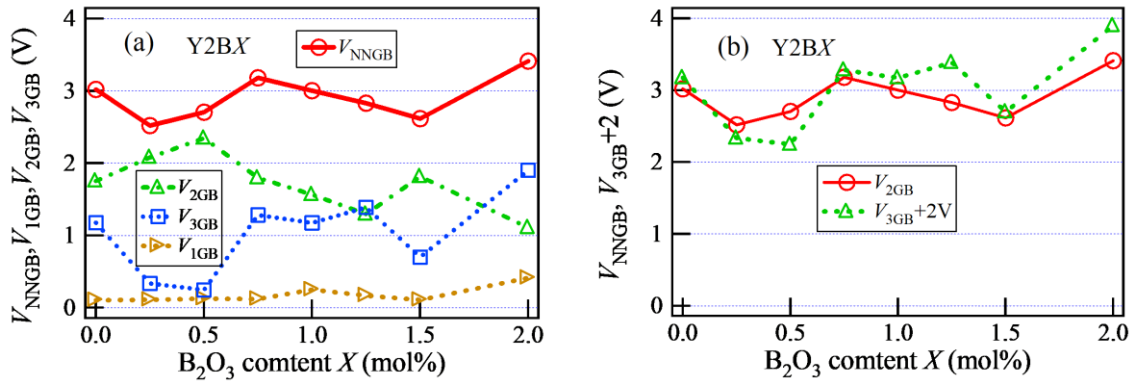


Figure 6.21 (a) V_{NNGB} , V_{1GB} , V_{2GB} , and V_{3GB} per grain boundary for Y2BX at 130°C and (b) correlation of V_{3GB} and V_{NNGB} .

6.7 Relationship between B_2O_3 and SiO_2 additives

6.7.1 Microstructure and crystal structure when B_2O_3 and SiO_2 were added together

SiO_2 is a common additive in commercial varistors. SiO_2 was added by 2.65, 5mol% with varying B_2O_3 concentrations from 0-2mol% in this study to investigate whether B_2O_3 will interact with SiO_2 or not (other materials were the same). The XRD diffraction patterns for Y0 ceramics with different compositions of added Y_2O_3 , SiO_2 , B_2O_3 are demonstrated in Fig. 6.22. It shows the main diffraction peaks in Y0 ceramics are wurtzite ZnO, and secondary phases as spinel particle $Zn_{2.33}Sb_{0.67}O_4$, β - Bi_2O_3 . The Y-Sb-Bi-Zn oxide is found in Y-doped samples. The β - Bi_2O_3 peaks disappeared in Y-doped samples because the Bi was fully absorbed in compound Y. However, the β - Bi_2O_3 appeared in Y2Si2.65B0 when SiO_2 was doped, as Si replaces small amounts of Bi in compound Y led to the Bi_2O_3 layer at grain boundaries in Fig. 6.23. These Bi_2O_3 peaks decreased and finally disappeared when B_2O_3 was added. Willemite Zn_2SiO_4 is found in Si-added samples. Although diffraction peaks directly related to B are not detected, the willemite peaks show an obvious shrinkage with addition of B_2O_3 . Hence, B ions would preferentially react with Si first, and then with Bi, resulting in amorphous phases such as glass phase BiBO or BSiO.

Figure 6.23 demonstrates the microstructure at grain boundaries and EDS element mapping under TEM of Si-added samples. Except for the willemite, small amount of Si is also found in

compound Y, referred to as YSi. It may explain how the β -Bi₂O₃ appeared in Y2Si2.65B0, because the solubilized Si substitutes few Bi in compound Y. SiO₂ reacted with B₂O₃ that resulted in a Si-B-O glass phase, located in compound Y. While increasing the B₂O₃ amount, a Bi-Si-B-O amorphous phase (BiBSi) appeared at grain boundaries, shown in Fig. 6.23 (b). S_G for Y2Si2.65BX is around to 2.4-2.5um (Table 6.2).

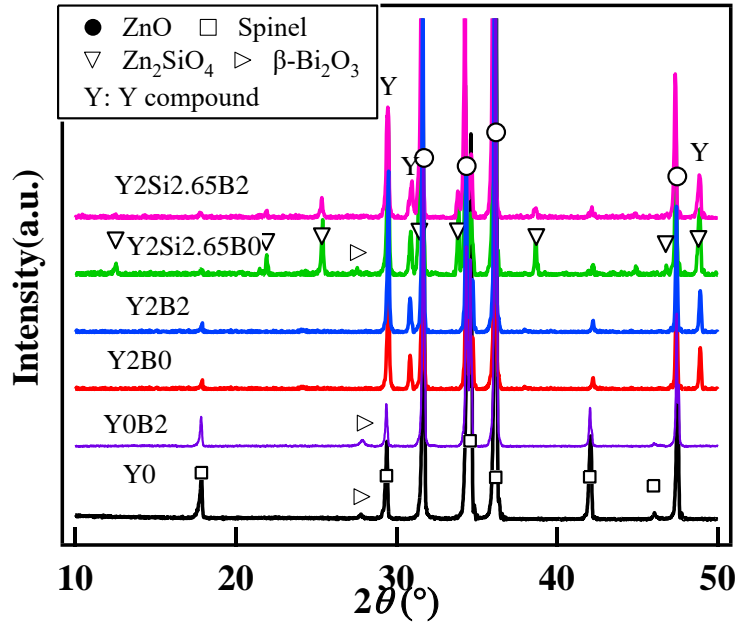


Figure 6.22 XRD patterns for different type of samples adding B₂O₃, SiO₂, Y₂O₃.

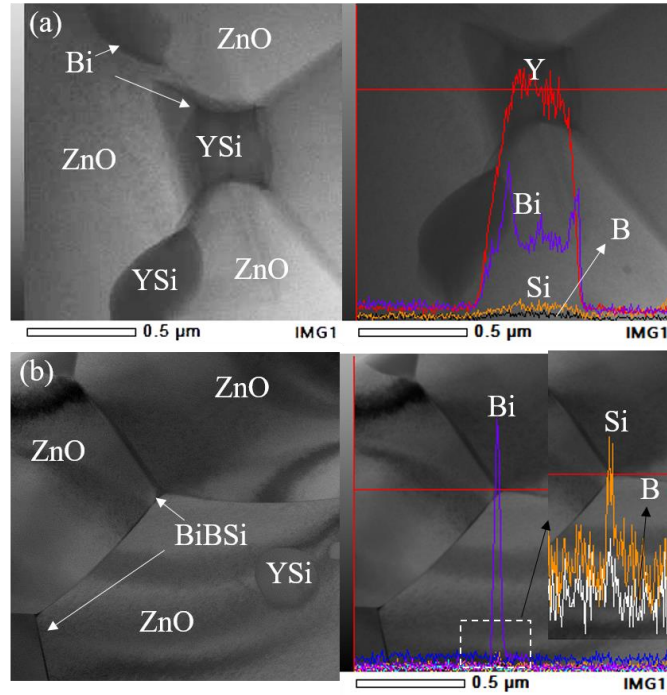


Figure 6.23 Microstructure at grain boundaries and element line mapping under TEM of (a) Y₂Si_{2.65}B₁ sample; (b) Y₂Si_{2.65}B₂.

Table 6.3 Electrical properties for Y-doped samples with SiO₂ 2.65mol% and B₂O₃ amount from 0 to 2mol%.

B ₂ O ₃ (mol%)	V _{NN} (V/mm)	S _G (μm)	α _a _s	J _L (μA/cm ²)	Φ (eV)	N _D (10 ¹⁶ cm ⁻³)	N _{iso} (10 ¹² cm ⁻³)	W _{DL} (nm)
0	996	2.4	49	0.29	1.07	22.1	2.98	135
0.5	944	2.5	47	0.28	1.10	19.0	2.79	148
1	1036	2.4	49	0.55	1.05	24.7	3.12	127
1.5	966	2.5	50	0.63	1.04	25.1	3.14	125
2	917	2.6	38	0.51	1.19	25.9	3.41	132

6.7.2 Electrical properties when B₂O₃ and SiO₂ added together

Electrical properties of Si-added Y-doped segments with varying amounts of B₂O₃ are shown in Table 6.2. The increase of V_{NN} when Si was added is due to the decrease of grain size S_G by the formation of willemite. Grain size did not appear to change when increasing B₂O₃ from 0 to 2mol%. Little difference of V_{NN} was found with increasing B₂O₃ until 2mol% in SiO₂

added samples. Similarly, with α , which was almost constant close to 50, but decreased to 38 with 2mol% B_2O_3 .

The relationship of $J_D(t)-t$ for Y-doped varistors with various amounts of SiO_2 and B_2O_3 were presented in Fig. 6.24. Firstly, the J_0 decreased by adding B_2O_3 until around 1mol%, and then increased with further increasing B_2O_3 . The decrease of J_0 was related to the decrease of N_D , as shown in Table 6.1 and 6.2. It was observed that the increasing of J_D along the degradation time t was suppressed by adding B_2O_3 but accelerated by adding SiO_2 . The change rate of J_D , J_{20}/J_0 was calculated and drawn in Fig. 6.24 (d). When SiO_2 amount was increased from 0 to 5mol%, the smallest value shifted to larger B_2O_3 content region, because the formation of glass phase BSiO reduced the efficiency B ions in ZnO. B_2O_3 additives increase α , the degradation resistance, and V_{NN} , while inhibiting J_L . Although excess B_2O_3 (2mol%) leads to slightly degradation and decrease of V_{NN} .

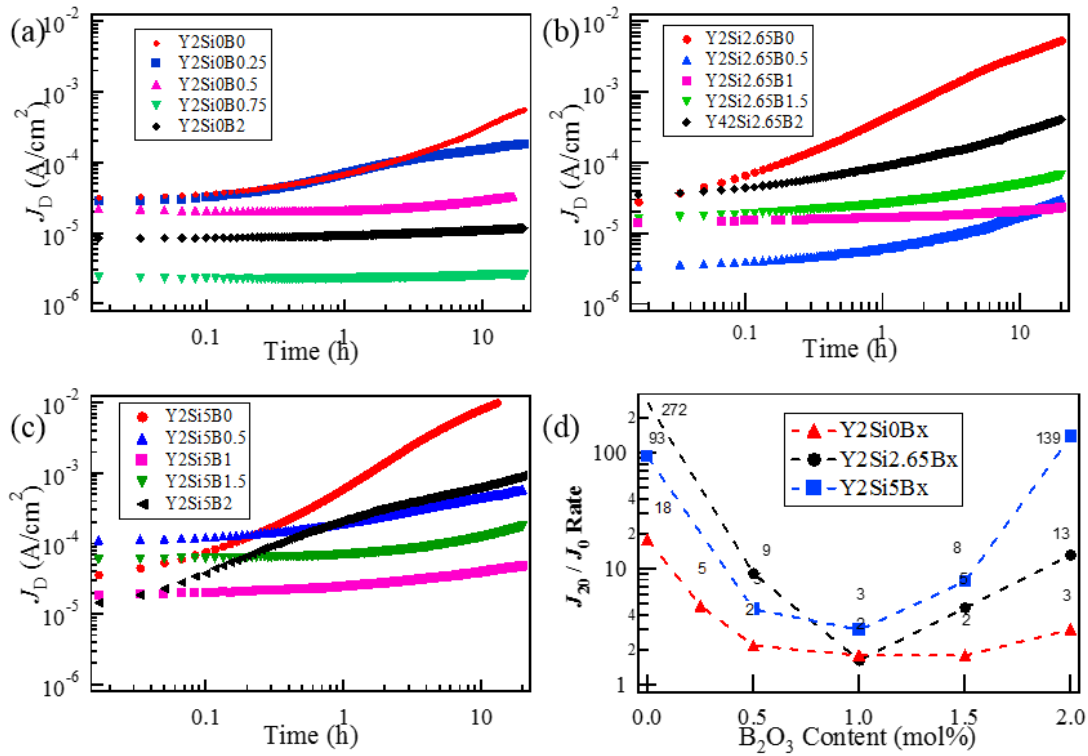


Figure 6.24 The J_D-t characteristics for (a)Y2Si0BX, (b)Y2Si2.65BX, (c)Y2Si5BX adding various amount of B_2O_3 , and (d) change rate of J_D , J_{20}/J_0 with different amount of SiO_2 and B_2O_3 .

It is suspected that Si reacts with B to form glass phase BSiO, which melted during the sintering process. This glass melting point decreased with increasing B amount¹⁹, and the surface tension decreased with higher B that let the liquid cover whole grain surface, shown in

Fig. 6.23. However, this BSiO glass may lead to an increase of current paths under bias that decreases the degradation resistance of samples. When extra B_2O_3 (2mol%) was added, glass phase BiBSi formed that reduced Bi_2O_3 and decreased nonlinearity. Therefore, if SiO_2 is added into samples, the effect of B_2O_3 on the electrical properties will be weaker due to the formation of BSiO which absorb efficient B ions that affect Schottky barriers and interface states. What is more, the improvement of electrical degradation is depended on B ions alone.

6.8 Conclusions

1. Boron (B) ions are found in Y-compounds together with Bi ions for Y-doped varistors. When the amount of B_2O_3 was greater than 0.75 mol%, a Bi-rich glass phase containing B began to grow at the grain boundaries, twinning the shape of the Y-compound as the B_2O_3 concentration increased. Formation of this Bi-rich phase first reduced the Co concentration in the ZnO grain that also decreased donor density N_D . However, when the B_2O_3 amount was greater than 1 mol%, excessive B ions contributed as donors in ZnO grain and therefore increased N_D .
2. Barrier height Φ_{B0} under no bias showed a minimum at ≈ 1.0 mol%; after that, it increased slightly with B_2O_3 . The addition of B_2O_3 did not change Φ_{B0} , but did change S_{MAX} significantly, indicating that V_{NNGB} was related mainly to the ratio of empty interface state to N_{IS0} under no bias for Y-doped samples.
3. The optimal amount of B_2O_3 of 0.75 mol% drastically improved the electrical properties and resistance to degradation of Y-doped varistors. These samples exhibited an exceptionally high long-term stability to DC electrical degradation. A sharp bending of $V_N - J$ relation near J region between pre-breakdown and breakdown regions was observed by adding optimum amount of B_2O_3 .
4. A method was developed to analyze conduction processes of the $V_N - J$ relation of ZnO varistors. The differential resistance R_D was effective for evaluating the effects of B_2O_3 addition on the $V_N - J$ relation. Results showed that the $V_N - J$ relation could be attributed to three conduction processes located separately in the forward-biased region I, the reverse-biased region III, and the interface region II of the energy band. Each voltage drop V_{Ni} ($i = 1, 2, 3$) could be calculated from R_{Di} . The R_{D1} and R_{D2} values exhibited a junction diode-like property in regions I and III. Both corresponded to the voltage drop that may be dominated by a conduction process similar to the thermionic emission mechanism. The R_{D2} value showed a significant correlation with the maximum value of nonlinearity index

α_{asMAX} . The R_{D3} value may be related to region II close to reverse-biased side, which affects electrical degradation together with R_{D2} . Excellent long-term stability was achieved with the largest index i_2 .

5. When SiO_2 was added into samples, the effect of B_2O_3 on interface states and Schottky barrier vanished because of the reaction between SiO_2 and B_2O_3 that formed BSiO glass, reducing the efficiency of B_2O_3 . Electrical degradation was inhibited by adding B_2O_3 , with around 1mol% no matter the amount of SiO_2 .

References

1. J. He, C. Cheng, J. Hu, Electrical degradation of double-Schottky barrier in ZnO varistors, *AIP Adv.* 6 (2016) 030701.
2. J. Lin, S. Li, J. He, L. Zhang, W. Liu, J. Li, Zinc interstitial as a universal microscopic origin for the electrical degradation of ZnO-based varistors under the combined DC and temperature condition, *J. Eur. Ceram. Soc.* 37 (2017) 3535-3540.
3. T. Asokan, R. Freer, Grain and grain boundary conduction in zinc oxide varistors before and after DC degradation, *J. Eur. Ceram. Soc.* 11 (1993) 545-550.
4. P. Q. Mantas, J.L. Baptista, The barrier height formation in ZnO varistors, *J. Eur. Ceram. Soc.* 15 (1995) 605-615.
5. S. Hirose, H. Niimi, K. Kageyama, et al., Degradation of potential barriers in ZnO-based chip varistors due to electrostatic discharge, *J. Appl. Phys.* 112 (2012) 033707.
6. M. S. Castro, C. M. Aldao, Different degradation processes in ZnO varistors, *Ceram. Int.* 22 (1996) 39-43.
7. A.V. Ivanchenko, A.S. Tonkoshkur, V.O. Makarov, Desorption thermal degradation model of zinc oxide ceramics, *J. Eur. Ceram. Soc.* 24 (2004) 3709-3712.
8. K. Eda, Destruction mechanism of ZnO varistors due to high currents, *J. Appl. Phys.* 56 (1984) 2948-2955.
9. W. Mielcarek, A. Gubański, G. Paściak, K. Prociów, J. Warycha, J. M. Wrobel, The effect of bismuth oxide polymorph forms on degradation processes in ZnO varistors, *Ceram. Int.* 39 (2013) 8219-8226.
10. J. P. Gambino, W.D. Kingery, G.E. Pike, L.M. Levinson, H.R. Philipp, Effect of Heat Treatments on the Wetting Behavior of Bismuth-Rich Intergranular Phases in ZnO:Bi:Co Varistors, *J. Am. Ceram. Soc.* (1989) 642-645
11. M. A. Ponce, C. Macchi, F. Schipani, C.M. Aldao, A. Somoza, Mild degradation processes in ZnO-based varistors: The role of Zn vacancies, *Philos. Mag.* (2015) 1-14.
12. M. Takada, Y. Sato, S. Yoshikado, Relation between grain boundary structure and electrical degradation in zinc oxide varistors, *J. Am. Ceram. Soc.* 95 (2012) 2579-2586.
13. M. A. Alim, S. Li, F. Liu, P. Cheng, Electrical barriers in the ZnO varistor grain boundaries, *Phys. Status Solidi Appl. Mater. Sci.* 203 (2006) 410-427.
14. M. Takada, S. Yoshikado, Effect of thermal annealing on electrical degradation characteristics of Sb-Bi-Mn-Co-added ZnO varistors, *J. Eur. Ceram. Soc.* 30 (2010) 531-538.

15. E. D. Kim, M. H. Oh, C.H. Kim, Effects of annealing on the grain boundary potential barrier of ZnO varistor, *J. Mater. Sci.* (1986) 3491-3496.
16. L. Meng, G. Li, L. Zheng, L. Cheng, J. Zeng, H. Huang, The effect of Bi₂O₃/SiO₂ molar ratio and annealing on the dc degradation of ZnO varistors, *J. Am. Ceram. Soc.* (2011) 2300-2303.
17. F. Liu, G. Xu, L. Duan, Y. Li, Y. Li, P. Cui, Influence of B₂O₃ additives on microstructure and electrical properties of ZnO-Bi₂O₃-Sb₂O₃-based varistors, *J. Alloys Compd.* 509 (2011) L56-L58.
18. L. Cheng, G. Li, K. Yuan, L. Meng, L. Zheng, Improvement in nonlinear properties and electrical stability of ZnO varistors with B₂O₃ additives by nano-coating method, *J. Am. Ceram. Soc.* 95 (2012) 1004-1010.
19. S. Wan, W. Lu, X. Wang, Low-temperature sintering and electrical properties of ZnO-Bi₂O₃-TiO₂-Co₂O₃-MnCO₃-based varistor with Bi₂O₃-B₂O₃ frit for multilayer chip varistor applications, *J. Am. Ceram. Soc.* 93 (2010) 3319-3323.
20. W. Hao, Z. Hongfeng, K. Jiashuang, Z. Yuanxiang, X. Qingyun, Properties of ZnO varistor ceramics co-doped with B₂O₃ and Al₂O₃, *Chinese J. Mater. Res.* 35 (2021) 110-114.
21. K. Tsuda, K. Mukae, Characterization of Interface States in ZnO Varistors using Isothermal Capacitance Transient Spectroscopy, *J. Ceram. Soc. Japan* 100 (1992) 1239-1244.
22. Y. Yamashita, S. Yoshikado, Evaluation of factors in the degradation of ZnO varistor, *IEEJ Trans. Power Energy* 119 (1999) 652-657.
23. K. Mukae, K. Tsuda, I. Nagasawa, Capacitance-vs-voltage characteristics of ZnO varistors, *J. Appl. Phys.* 50 (1979) 4475-4476.
24. G. Blatter, F. Greuter, Carrier transport through grain boundaries in semiconductors, *Phys. Rev. B*, 33(6) (1986) 3952-3966.
25. W. Shockley, The theory of p-n junctions in semiconductors and p-n junction transistors, *Bell Syst. Tech. J.* 28 (1949) 435-489.
26. K. Eda, Conduction mechanism of non-Ohmic zinc oxide ceramics, *J. Appl. Phys.* 49(5) (1978) 2964-2972.

Chapter 7

High voltage Bi-based ZnO varistors adding with SiO₂

7.1 Introduction

The high voltage varistors doped with Y₂O₃ and their additive effects have been studied in detail in chapters 5 and 6. In this way, it is possible to make varistors with double the voltage of commercial varistors and keep the same device for UHV application. The Electrical properties of this type of material are remarkably dependent upon the ratio of Sb₂O₃ and Y₂O₃, and additives such as Cr, Ni or B are required to inhibit the electrical degradation. Due to the lack of rare earth metal Y and the toxic nature of Sb, however, people are now seeking substitutes that use clean and cheap materials.

Varistor voltage for ZnO varistors can be controlled by adding small amount of SiO₂¹⁻⁵. When SiO₂ is added to ZnO particles, Willemite particles (Zn₂SiO₄) are formed at the grain boundaries which inhibit the growth of ZnO grains, thus reducing ZnO grain size. The effect of SiO₂ added heavily to 6 wt% in Bi₂O₃-Co₂O₃-MnO₂-TiO₂ based ZnO varistors sintered at low temperature on electrical characteristics was investigated by Zhao and his team³. They reported that average grain size decreased by adding SiO₂ and the varistor voltage increased with increasing the amount of SiO₂ and reached to 1300 V/mm for 6 wt% SiO₂ addition. However, the electrical degradation is not discussed. In chapter 6, we found that adding a small amount of SiO₂ (i.e., 2.65, 5mol%) increased the varistor voltage and nonlinear index of Y-doped varistor, but the electrical degradation became much worse and leakage current increased by more than 100 times after degradation test. Thus, we attempted in this chapter to fabricate and evaluate ZnO varistors using Bi₂O₃-Co₂O₃-MnO₂-based ZnO varistors without adding Y₂O₃ or Sb₂O₃, for the high varistor voltage and good stability.

Furthermore, the effects of the addition of B₂O₃ on the resistance of electrical degradation was investigated. The melting and boiling points of B₂O₃ are ≈ 450 and >1500°C, respectively and in sintering, it does not evaporate. Around 450 °C, B₂O₃ melts completely and fills in the interspaces among other compounds. It is expected that B₂O₃ in liquid state at calcined temperature promotes the sintering of ZnO. The ionic radius of B₂O₃ is ≈ 0.02 nm and it exists in ZnO grain, grain boundaries and secondary phases. As boron has a strong covalency, it is expected to exist at interstitial sites in ZnO and preventing ion drift that causing the electrical degradation. This effect is found in Y-doped varistors and discussed in chapter 6. However, the

reaction between B_2O_3 and SiO_2 affects the electrical properties. In this study, the influence of the addition of B_2O_3 to Si-doped varistors is also investigated.

The effects of SiO_2 and B_2O_3 addition to Bi-Mn-Co-based ZnO varistors samples were fabricated and evaluated in this chapter. These samples are expected to obtain varistor voltage more than twice as much as the commercial varistor. The electrical properties, microstructures and interface states were investigated in detail.

7.2 Experiments

7.2.1 Sample preparation

ZnO varistors were fabricated from ZnO (99.9999 purity, Meidensha, Japan), Bi_2O_3 (0.25 mol%), MnO_2 (0.55 mol%), Co_3O_4 (0.0, 0.2 mol%) as basic additives (hereafter denoted ZBMC) and added with SiO_2 (0–55 mol%) and B_2O_3 (0–10 mol%). Each component was determined to contain 100 mol% ZnO. The molar ratio of Bi_2O_3 , MnO_2 and Co_3O_4 to ZnO was the same in each sample. The preparation method is described in Chapter 4. Hereafter, each sample is given a simplified sample name according to its composition. For example, the sample consisting of basic additives (ZBMC), 0–55 mol% SiO_2 , and 1.00 mol% B_2O_3 is denoted ZBMCSi0–55B1 or Si0–55B1.

In addition, ZBMCSi16B0 and ZBMCSi16B1 samples varying the Bi_2O_3 amount (0, 0.125, 0.250, 0.375, 0.50, 0.75 mol%) was prepared to evaluate the relationship between Bi, Si and B.

7.2.2 Sample Evaluation

The V – J characteristic was measured using the method described in Chapter 4. Electrical degradation was tested on each sample. The average ZnO grain size was estimated from micrographs obtained by an optical microscope (Eclipse ME600, Nikon, Tokyo, Japan) by taking the grain size to be equal to the side length of a square with the same area. The surface observation and elemental compositions of the samples were analyzed by SEM (JSM-7500FA, JEOL, Tokyo, Japan). EDS, (EX-64195JMU, JEO, Tokyo, Japan), and the BSE (SM-34110; JEOL, Tokyo, Japan) modes were used in the SEM to analyze the composition on the surface of the grain boundaries. The crystal structure was analyzed by XRD. Interface traps were investigated by ICTS at constant temperature. The measurements were conducted using a

capacitance meter (72B (Option 05A), Boonton, USA; test frequency: 1 MHz), pulse generator (8110A, Keysight Tech., Santa Rosa, CA, 1973, NF corp. Tokyo, Japan, Leading and trail edges of a pulse to prevent overshoot: 100 μ s) and a digital voltmeter (34410A and 34411A, Keysight Tech., Santa Rosa, CA). The AC test bias voltage was 100 mVrms, pulse width was 20 ms, pulse amplitude was set to 1/6, 1/3, or 2/3 of varistor voltage (high level) and 0 V [low level (base line)], and measurement time range was 2×10^{-4} – 9000 s. The measurements were performed over the temperature range from 40 to 200°C, and the temperature was controlled to within 0.1°C.

7.3 Microstructure and Crystallographic properties

7.3.1 Microstructure

When SiO₂ is added to a ZnO varistor, willemite particles are formed¹. Therefore, EDS, BSE, and XRD were used to examine the compounds formed at the ZnO grain boundaries. Samples were fractured and the shapes and element distributions of the grain boundary fracture surfaces were analyzed by SEM and BSE, respectively. This provided observations of the boundaries between two ZnO grains.

The compositional images in the BSE mode and elemental mapping for ZBMCSi25B0 are shown in Fig. 7.1 (a). The strong contrast of the BSE revealed a different composition for the segregated particles and ZnO particles. The elemental mapping revealed that the large bright gray part contained large amounts of Zn, the large dark gray part contained large amounts of both Zn and Si, and the small bright gray part contained large amounts of Bi. It appears that ZnO and willemite particles form a larger cluster. Grain sizes for ZnO and willemite were comparable. A similar result was obtained for ZBMCSi25B1, as shown in Fig. 7.1(b). Microstructure and grain size of Si25B0 and Si25B1 samples did not appear to differ significantly in SEM images.

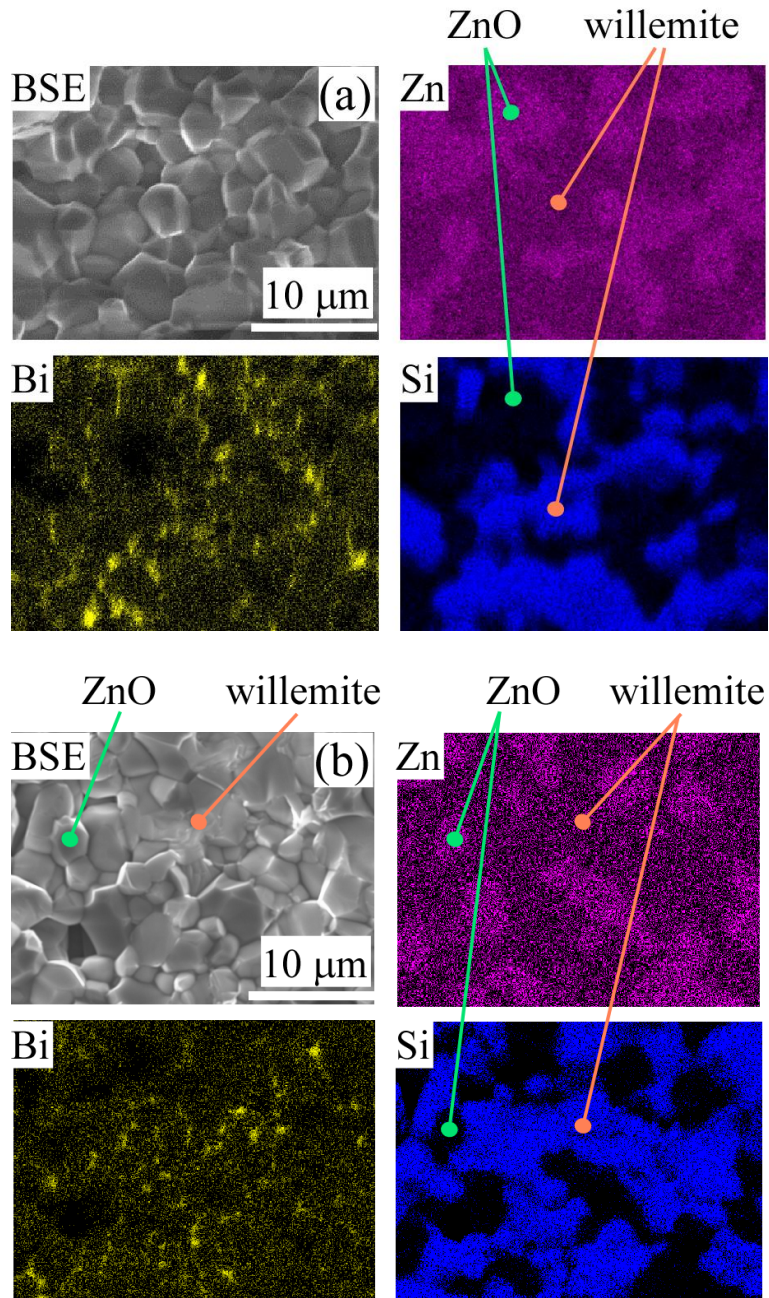


Figure 7.1 Compositional image in BSE mode and elemental mappings of Zn ($K\alpha$), Bi ($M\alpha$), Si ($K\alpha$) on fractured surface for (a) ZBMCSi25B0, (b) ZBMCSi25B1.

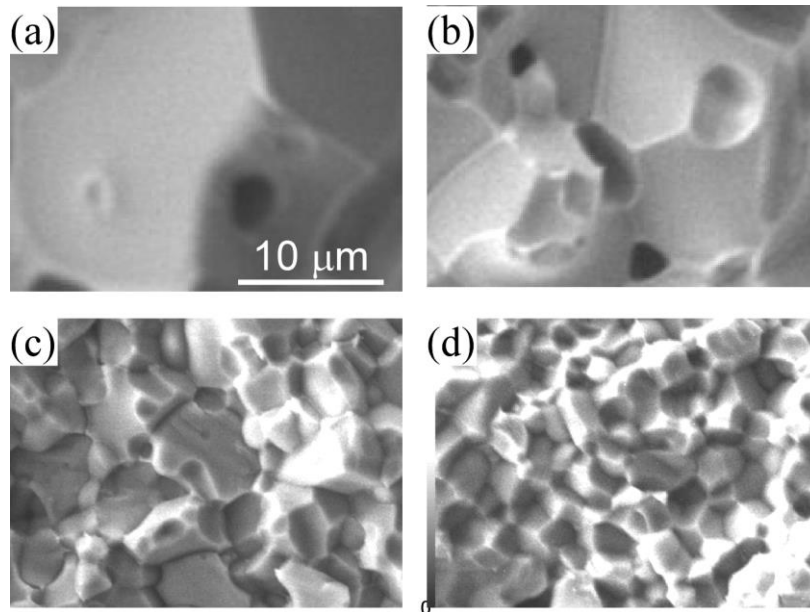


Figure 7.2 Microstructures on fractured surfaces of the sintered (a) ZBMCSi0B1, (b) ZBMCSi2B1, (c) ZBMCSi16B1, and (d) ZBMCSi25B1.

Microstructures on fractured surfaces of the sintered (a) ZBMCSi0B1, (b) ZBMCSi2B1, (c) ZBMCSi16B1, and (d) ZBMCSi25B1 are shown in Fig. 7.2. As SiO₂ increased, grains grew smaller. Since the perfect cleavage plane of ZnO is the (0001) plane and the secondary cleavage plane of ZnO is the (1010) plane, a ZnO grain should be fractured by cleavage as shown in Figure 7.2 (a) and (b).

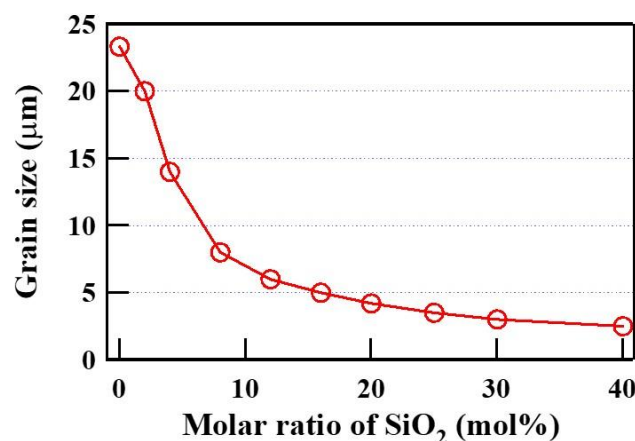


Figure 7.3 Relation between the averaged grain size and the molar ration of added SiO₂.

Association between the averaged grain size for both ZnO and willemite particles and the molar ration of added SiO₂ is shown in Figure 7.3. The average grain size decreased in inverse

proportion to the amount of SiO₂ added. With comparable particle size was observed in the sample without Co₃O₄, it was suggested that willemite was acting as a grain growth inhibitor other than reported (Zn,Co)₂SiO₄³. A macroscopic pore without facets was observed when the amount of SiO₂ was small, but it decreased as the SiO₂ amount increased.

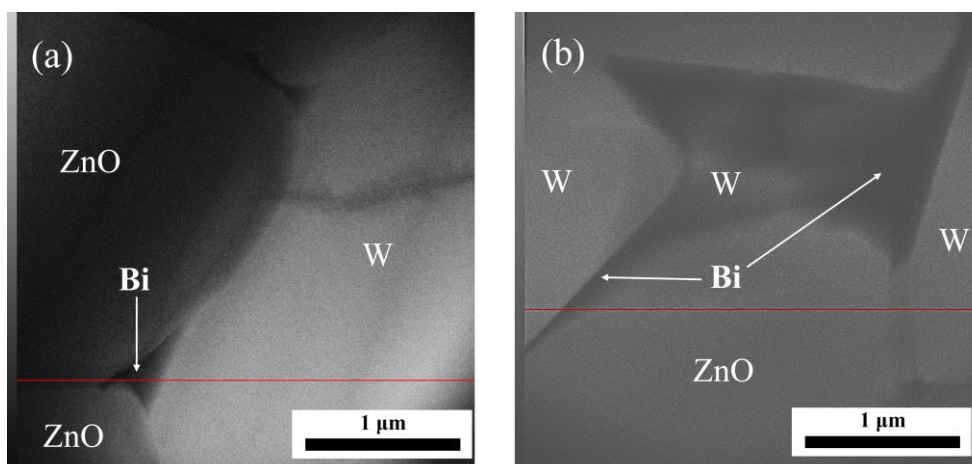


Figure 7.4 EDS images observed under TEM for the microstructure at grain boundaries (a) ZBMCSi25B0, (b) ZBMCSi25B1.

In conjunction with the element mapping, TEM was used to observe the microstructure at grain boundaries, shown in Fig. 7.4 (a) ZBMCSi25, and (b) ZBMCSi25B1. Fig. 7.4 (a) shows that the Bi₂O₃ existed at the triple points at ZnO/willemite grain boundaries. The Bi-layer was more homogenous with the addition of B₂O₃, generated at both triple points and the grain boundaries, shown in Fig.7.4(b).

7.3.2 Crystal structure

XRD patterns from the pressurized surfaces at diffraction angles of $2\theta = 3 - 90^\circ$ for ZBMCSi0B0 and ZBMCSi25B0 samples are shown in Figure 7.5 for example. In the same Figure, XRD patterns for willemite is shown. It is confirmed that most of XRD patterns for ZBMCSi25B0 samples agreed with wurtzite-type ZnO (JCPDS No. 89-0510) or willemite (JCPDS No. 37-1485)³³. Therefore, the large bright and dark gray parts in BSE images are identified with wurtzite-type ZnO and willemite particles, respectively. The other broad diffraction peaks of compounds were observed at $2\theta \approx 27.5-28.5, 32.5, 46.5, \text{ and } 55^\circ$ for the samples to which B₂O₃ was not added, tough in the figure, it is not clear. Similar XRD patterns for ZBMCSi0-40B0 and ZBMCSi0-55B1 were obtained. The intensity of diffraction peaks for

ZnO particles decreased and those for willemite particles increased with increasing the amount of SiO₂.

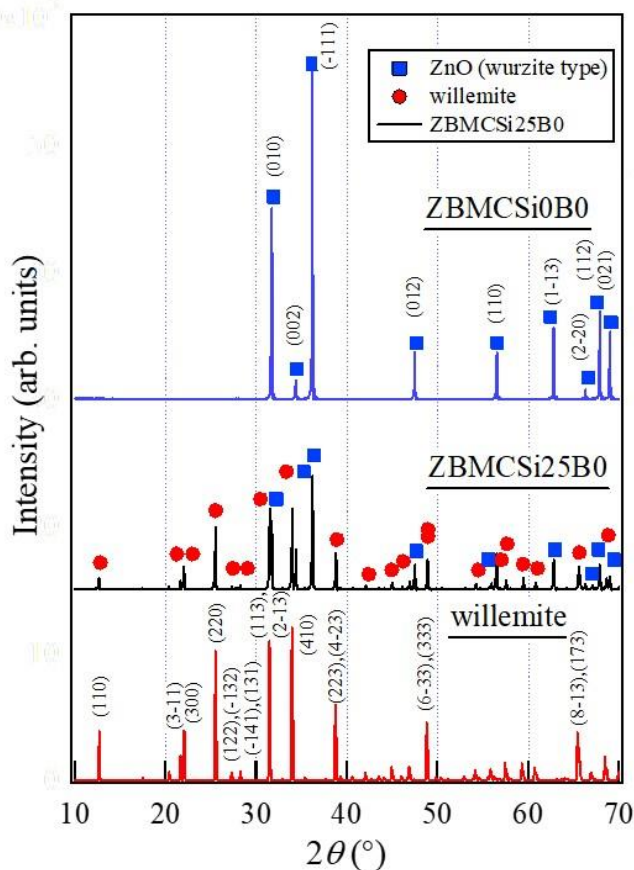


Figure 7.5 XRD patterns for Si for ZBMCSi0B0 and ZBMCSi25B0 samples. ■: ZnO , ●: willemite

The orientation of ZnO particles and resistance to electrical degradation have been reported to be correlated⁸. The increase in the amount of willemite particles has been reported to promote electrical degradation^{17,18}. Changes in the orientation of (100), (002), and (101) planes of a ZnO particle and (220), (113), (410), and (223) planes of a willemite particle will appear as differences in the intensity of the diffraction peaks⁹. The diffraction peak of (220) plane for a willemite particle does not overlap other peaks. Therefore, the intensity of those diffraction peaks for ZnO and willemite particles was analyzed. Figure 7.6 shows a detailed view of the absolute integrated intensity AI of the diffraction peaks from the (100), (002), and (101) planes of a ZnO particle for ZBMCSi0–40B0 and ZBMCSi0–55B1 samples. The horizontal axle of the figures is a molar fraction of SiO₂ in % ($[\text{SiO}_2] / ([\text{SiO}_2] + [\text{ZnO}])$), $[\text{ZnO}] = 100$ mol%,

hereafter MRS) for all molar amounts of both SiO₂ and ZnO ([SiO₂]+[ZnO]). *III* for all planes of ZnO particles was almost the same; however, it decreased linearly in proportion to MRS above 4 % and became zero at 35 %, as illustrated in Figure 7.6 (a). *III* for all planes of willemite particles for both ZBMCSi0-40B0 and ZBMCSi0-50B1 was also almost the same; increased linearly in proportion to the molar fraction of SiO₂ as shown in Figure 7.6 (b). As a result, most of the SiO₂ and ZnO added are used for the generation of willemite, whereas B₂O₃ barely influences the formation of willemite. A compound fabricated with SiO₂ added above 35 % MRS does not function as a varistor because all ZnO grains are eliminated by the formation of willemite. Moreover, the results mean that the orientation of both a ZnO and a willemite particle does not change above 4 % MRS. In contrast, the orientation of a ZnO particle was markedly changed by adding up to 4 % MRS to the samples that contained or did not contain B₂O₃. The crystal structure is then analyzed.

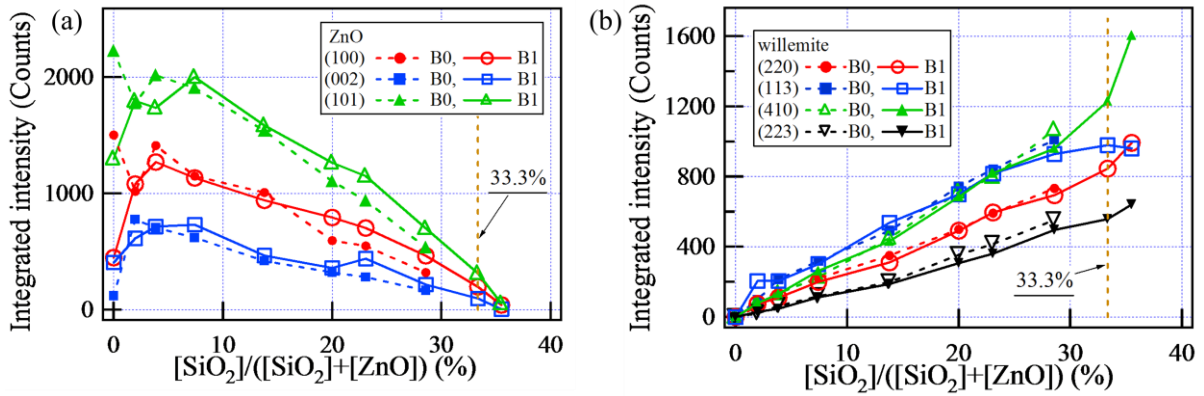


Figure 7.6 Relation between integrated intensity of X-ray diffraction peaks for (a) ZnO and (b) willemite for ZBMCSi0-40B0 and ZBMCSi0-55B1 samples and the molar ratio of SiO₂.

Figure 7.7 shows XRD patterns at (a) $2\theta \approx 26.5\text{--}29^\circ$ and (b) $31\text{--}33^\circ$ for ZBMCSiXB0,1 ($X = 0, 2, 4, 8, 16, 40$) samples. Solid lines represent XRD patterns for ZBMCSiXB0. The dots show XRD patterns for ZBMCSiXB1. Dashed lines show the differences in diffraction peak intensities between ZBMCSiXB0 and ZBMCSiXB1. For ZBMCSiXB0 samples, peaks of relatively strong intensity were observed at $2\theta \approx 27.5\text{--}28.5, 32.5, 46.5, 47,$ and 55° , which disappeared for ZBMCSiXB1 samples. The *hkl* of the diffraction peaks for willemite hardly changed. Amorphous borate glass diffraction peaks caused by the compounds of Bi_2O_3 and B_2O_3 were not observed for ZBMCSiXB1 samples³⁵. As the amount of SiO_2 increased, the difference in diffraction peaks at $27.5\text{--}28.5^\circ$ between samples with and without B changed rapidly. It is composed of superimposing of 3–5 diffraction peaks, $2\theta \approx 27.2, 27.5, 27.7, 27.9,$ and 28.2° , taking the shape and the full width of the half maximum. The broad diffraction peaks observed at $2\theta \approx 27.5\text{--}28.5^\circ$ for ZBMCSi0B0 are Bi_2O_3 . In general, Bi_2O_3 have different

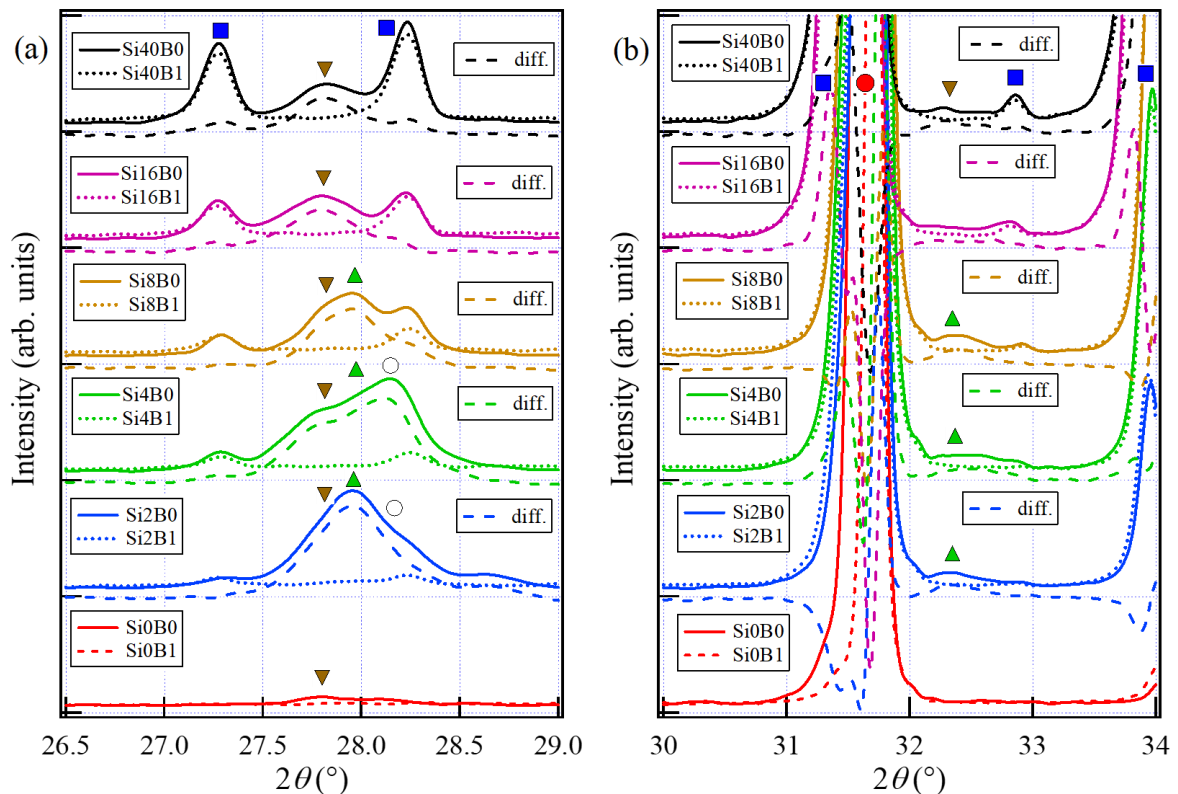


Figure 7.7 XRD patterns for compounds for ZBMCSiXB0 and ZBMCSiXB1 samples ($X=0, 2, 4, 8, 16, 25$) and the difference of them. ●: ZnO, ■: willemite, ▲: $\gamma\text{-Bi}_2\text{O}_3$, ▼: $\beta\text{-Bi}_2\text{O}_3$, ○: unknown.

morphology and various dimensions like 1D nanorods, nanotubes, nanowires, 2D nanoplates, nanoflakes and 3D hierarchical nanoflowers, and so on¹. There are four different polymorphs

such as α -, β -, γ -, and δ -Bi₂O₃ having the crystal structures monoclinic (JCPDS No. 41-1449), tetragonal (JCPDS No. 27-0050), cubic (JCPDS No. 27-0052), and polymorph phases, cubic (JCPDS No. 27-0052), respectively, as discussed in chapter 3^{36,37}. α -Bi₂O₃ is stable at low temperatures up to 730°C, while the cubic δ -Bi₂O₃ is the phase present at high temperatures (up to melting point at 824 °C). The rest of polymorphs are metastable phases at different temperature ranges, like the tetragonal β - and γ -Bi₂O₃ polymorph (450°C–667°C). Each differs by its phase, crystal structure, morphology and properties. The thin bismuth oxide layer at the grain boundaries is necessary to form a potential barrier for improving the varistor properties⁶. The role of Bi₂O₃ is limited to supplying excess oxygen to the grain boundaries⁶. Analysis confirms that α - and γ -Bi₂O₃ were not present in samples. The diffraction peaks for stable and metastable β -Bi₂O₃ show the maximum intensity at $2\theta \approx 27.80^\circ$ and has strong intensity at $2\theta \approx 31.19, 31.82, 32.71, 32.75, 45.82, 46.31, 46.93, 46.99, 53.45, 54.38, 55.43, 55.59, \text{ and } 57.43^\circ$. Among them, the diffraction peaks at $2\theta \approx 31.82$ and 31.19° overlap the diffraction peak for ZnO. The diffraction peaks for δ -Bi₂O₃ show the maximum intensity at $2\theta \approx 27.27^\circ$ and other strong intensity at $2\theta \approx 31.94, 45.79, 54.29, \text{ and } 56.91^\circ$. Therefore, diffraction angles for this broad one roughly agreed to those of β -Bi₂O₃ in particular.

Comparing the two sample groups, when B₂O₃ was added, no matter the amount of SiO₂ and willemite, no β -Bi₂O₃ existed in the materials. Furthermore, adding B₂O₃ does not affect the formation of willemite. As a further demonstration of the relationship between Bi and B, XRD patterns for ZBMCSi16B0 and ZBMCSi16B1 added with Bi₂O₃ of 0.125–0.75 mol% are shown in Fig. 7.8. The intensity of broad diffraction peaks at 27.8 and 32.5 ° increased with increasing the amounts of Bi₂O₃ in samples without B, while it hardly changes willemite. Relation between *AII* of the broad diffraction peak at 27.8 ° and the molar ratio of Bi₂O₃ is shown in Figure 7.9. The increasing rate was small below 0.25 mol% Bi₂O₃ and became larger and constant above it. This result shows that Bi₂O₃ forms compounds with other additives first in small amounts, and the consumption of Bi₂O₃ remains constant for a certain amount of addition (0.25 ml%), after which Bi₂O₃ remains alone for increasing additions. Therefore, the rapid increase of intensity for the broad diffraction peak by addition of the small amount of SiO₂, such as 2 mol%, as shown in Fig. 7.7 may be explained as follows: SiO₂ inhibits the reaction of Bi₂O₃ and other additives, so a part of Bi₂O₃, which corresponds to the rapidly increased amount, exists alone. B₂O₃ induces the formation of Bi-related compounds that do not contain Si. It is speculated that the formed compound contains Zn, Bi₂O₃ and/or B₂O₃. EDS has confirmed that Co dissolves in ZnO, so Co may also be present inside the compound. As

discussed in chapter 6, here, the formed compound is a Bi-B-O glass phase which exists at grain boundaries, as shown in TEM images in Fig. 7.4.

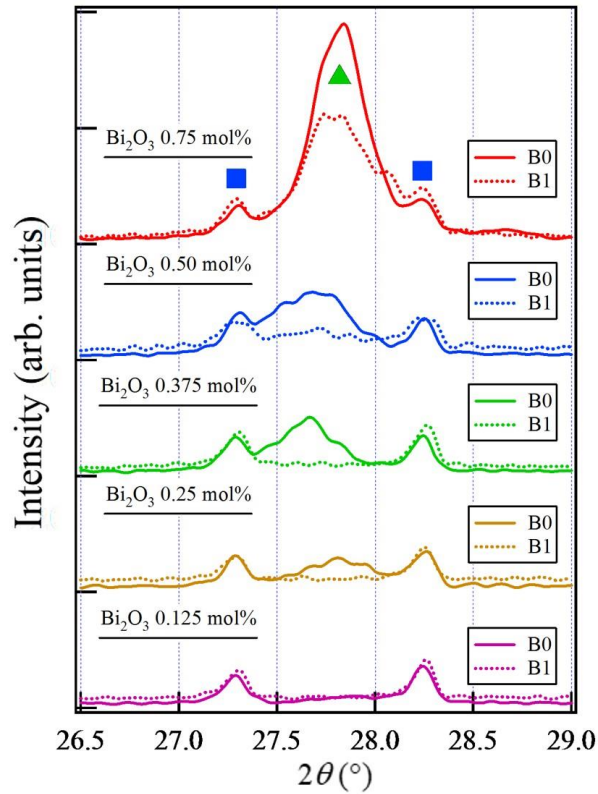


Figure 7.8 XRD patterns for compounds for the samples of ZBMCSi16B0 and ZBMCSi16B1 added Bi₂O₃ of 0.125, 0.25, 0.375, 0.50, and 0.75 mol%. ■: willemite, ▲: Bi₂O₃

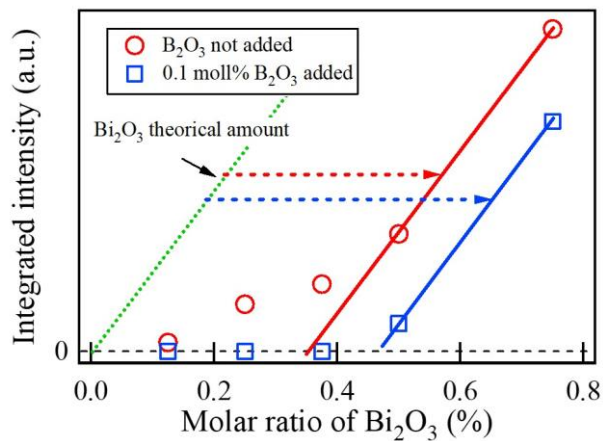


Figure 7.9 Relation between the integrated intensity of XRD diffractions and the molar ratio of added Bi₂O₃ for ZBMCSi16B0 and ZBMCSi16B1 samples.

7.3.3 Relative mass density

Circle plots in Figure 7.10 show the relation of measured mass density and the molar ratio of SiO₂ to ZnO (= [SiO₂]) for ZBMCSi0-40B0 and ZBMCSi0-50B1 samples. The mass density decreased monotonically with increasing SiO₂. As described above, the amount of willemite particles increased linearly in proportion to the amount of SiO₂. The mass densities of ZnO and willemite particles are $D_{\text{ZnO}} \approx 5.67$ and $D_{\text{willemite}} \approx 4.22$ g/cm³, respectively. Assuming that the averaged mass density (AMD) of the sample is determined approximately only in ZnO and SiO₂, AMD is given by

$$\begin{aligned}
 \text{AMD} &= \frac{M_{\text{unit-ZnO}}N_{\text{ZnO}} + M_{\text{unit-willemite}}N_{\text{willemite}}}{V_{\text{unit-ZnO}}N_{\text{ZnO}} + V_{\text{unit-willemite}}N_{\text{willemite}}} \\
 &= \frac{D_{\text{ZnO}}V_{\text{unit-ZnO}}N_{\text{ZnO}} + D_{\text{willemite}}V_{\text{unit-willemite}}N_{\text{willemite}}}{V_{\text{unit-ZnO}}N_{\text{ZnO}} + V_{\text{unit-willemite}}N_{\text{willemite}}} \\
 &= \frac{D_{\text{ZnO}}D_{\text{willemite}}[M_{\text{ZnO}}(1-3\text{MRS}) + M_{\text{willemite}}\text{MRS}]}{D_{\text{willemite}}M_{\text{ZnO}}(1-3\text{MRS}) + D_{\text{ZnO}}M_{\text{willemite}}\text{MRS}}, \tag{7.1}
 \end{aligned}$$

where

$$\frac{V_{\text{unit-ZnO}}N_{\text{ZnO}}}{V_{\text{unit-willemite}}N_{\text{willemite}}} = \frac{D_{\text{willemite}}M_{\text{ZnO}}(1-3\text{MRS})}{D_{\text{ZnO}}M_{\text{willemite}}\text{MRS}} \tag{7.2}$$

$M_{\text{unit-ZnO}}$ and $M_{\text{unit-willemite}}$ are the total net mass of atoms in each unit cell for ZnO and willemite, respectively. N_{ZnO} and $N_{\text{willemite}}$ are the number of each unit in a sample, separately. $V_{\text{unit-ZnO}}$ and $V_{\text{unit-willemite}}$ are the volume of each unit cell for ZnO and willemite, respectively. M_{ZnO} (81.36) and $M_{\text{willemite}}$ (222.76) are the molecular weight for ZnO and willemite, respectively. $\text{MRS} = [\text{SiO}_2] / ([\text{SiO}_2] + 100)$. The solid line in Fig.7.10 shows the AMD calculated using eq. 7.1. Plots show the relative density (RD) calculated by dividing the measured value by AMD. RD of approximately 90–100 % was obtained and increased by adding SiO₂ of ≈ 8 mol%. It has been found that adding SiO₂ or B₂O₃ to a sample enhances sintering.

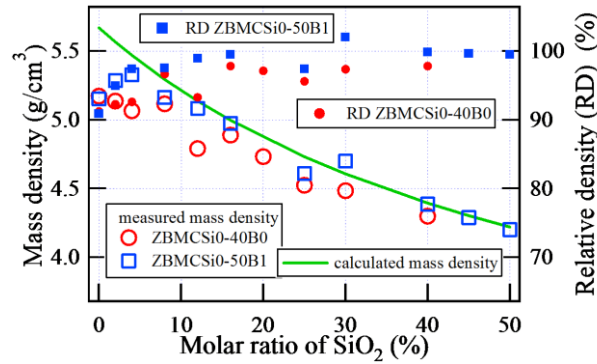


Figure 7.10 Relation between measured mass density, calculated mass density, and the relative density for Si for ZBMCSi0B0 and ZBMCSi25B0 and the malar ratio [SiO₂]

7.4 Electrical properties

7.4.1 Voltage–current characteristics

Normalized voltage–current density (V_N – J) characteristics for ZBMCSi16B0 and ZBMCSi16B1 at several temperatures up to 150°C are shown in Figure 7.11. V_N is the measured voltage per 1 mm thickness. An excellent nonlinearity of V_N – J characteristics was observed in both samples. The Bi or Mn free samples didn't show such excellent nonlinearity. The varistor voltages V_{NN} at 30°C for ZBMCSi16B0 and ZBMCSi16B1 were ≈ 773 and 872 V/mm and were almost constant with increasing measuring temperature. V_N – J characteristics changed sharply from pre-breakdown to breakdown regions by adding B₂O₃. Similar to usual varistors, the value of the current density increased with increasing measurement temperature. The increasing rate was relatively small.

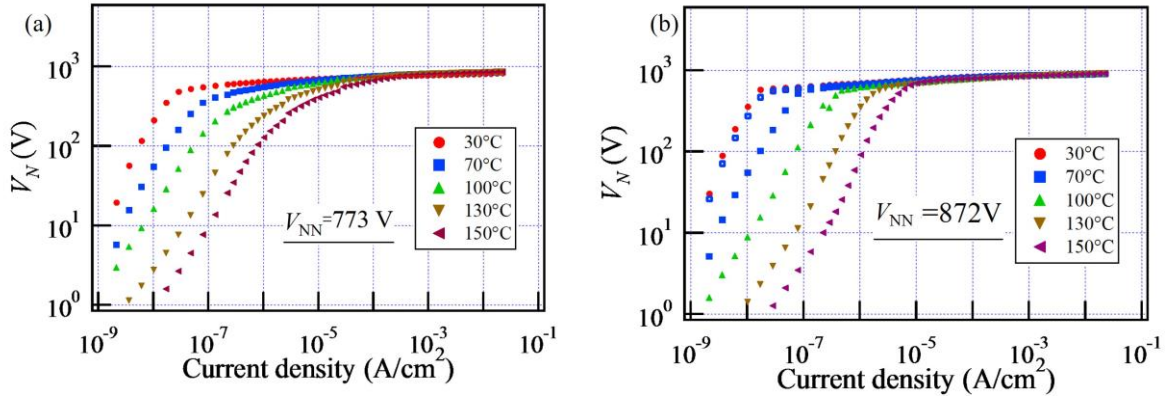


Figure 7.11 $V_N - J$ characteristics at several temperatures for the samples of (a) ZBMCSi16B0 and ZBMCSi16B1. V_{NN} : varistor voltage.

Figure 7.12 shows the relationship between varistor voltages V_{NN} and the molar ratio of SiO_2 for ZBMCSi0-40B0 and ZBMCSi0-40B1. Up to $\pm 12\%$ of deviations were observed from the averaged values of V_{NN} for several samples. V_{NN} increased linearly in proportion to SiO_2 up to 30 mol%. V_{NN} reached 2700 V/mm and 3000 V/mm for ZBMCSi40B0 and ZBMCSi40B1, respectively, and was much higher than that of conventional commercial varistors. Although samples added SiO_2 up to 55 mol% were prepared, when adding SiO_2 more than 45 mol%, the breakdown voltage suddenly increased up to 3000 V/mm and became unstable, as a result of which it was immeasurable.

The average grain size decreased linearly in proportion to SiO_2 amount similar to V_N . This means that V_{NN} is determined mainly by the grain size up to 30 mol% SiO_2 , because V_{NN} is the product of the number of ZnO grains boundaries between two facing electrodes with distance of 1mm and the voltage V_{NNGB} per one grain boundary. Therefore, V_{NNGB} is estimated at 3.6 V below 30 mol% SiO_2 . Similar result was obtained for and ZBMCSi25B1.

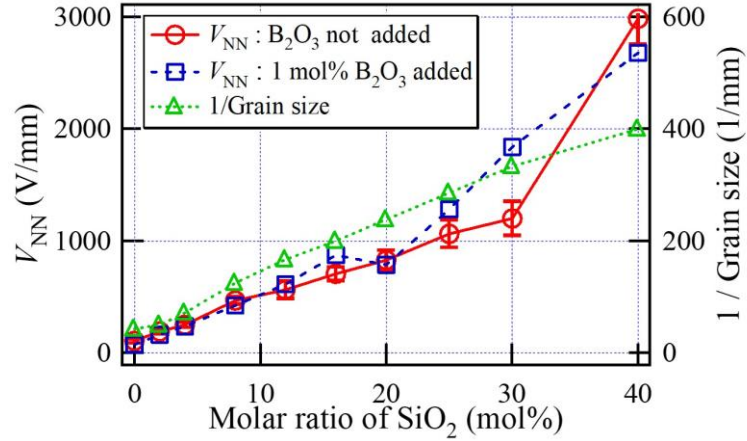


Figure 7.12 Relationship between varistor voltage V_{NN} for ZBMCSi0-40B0 and ZBMCSi0-40B1 samples and inverse of ZnO grain size for ZBMCSi0-40B0 samples and the molar ratio of SiO₂.

Assuming that willemite particles are insulators and S_G for ZnO and willemite were the same, the value of ZnO particles must be more than the volume percolation threshold ($\approx 33.3\%$) so that an electric current can flow through the sample. The volume percolation threshold of $\approx 33.3\%$ corresponds to $\approx 28\%$ mol% SiO₂. Due to the fact that ZnO and willemite particles form clusters, the volume percolation threshold might need to be lowered. S_G for ZBMCSi40B0 was $\approx 2.5\ \mu\text{m}$ and about ten times smaller than S_G of samples without SiO₂ ($23\ \mu\text{m}$). Total surface area of the particles increases as the size of ZnO and willemite particles decreases, while the amount of the additive except for SiO₂ remains constant. There will be a decrease of sediments Bi-layer thickness at grain boundaries, which is necessary for forming nonlinearity⁶. The relative grain boundary layer thickness T_{GB} normalized by the thickness for ZBMCSi0B0 was estimated assuming that the compounds consisting of Bi, Mn, Co, and/or B, of which total amount of constant for all molar ratio of SiO₂, except for Si, cover both ZnO and willemite particles (T_{GB1}) or only ZnO particles (T_{GB2}) using equation given by

$$T_{GB1} = \frac{S_G}{S_{G0}} \frac{1 + \frac{2MRS}{1-3MRS}}{1 + \frac{D_{ZnO} M_{willemite} MRS}{D_{willemite} M_{ZnO} (1-3MRS)}} \quad (7.3)$$

and

$$T_{GB2} = \frac{S_G}{S_{G0}} \left(1 + \frac{2MRS}{1-3MRS} \right), \quad (7.4)$$

where S_{G0} is the grain size. Relations between both T_{GB1} and T_{GB2} and SiO₂ for ZBMCSi0-40B0 are shown in Figure 7.13. T_{GB1} decreased monotonically with increasing SiO₂. On the

other hand, T_{GB2} became roughly constant above 8 mol% SiO_2 . It is expected that T_{GB} has the value between T_{GB1} and T_{GB2} . In either case, the thickness of the grain boundary layer does not become extremely thin even if SiO_2 is increased to 40 mol%. It is constant with the results of SEM mapping.

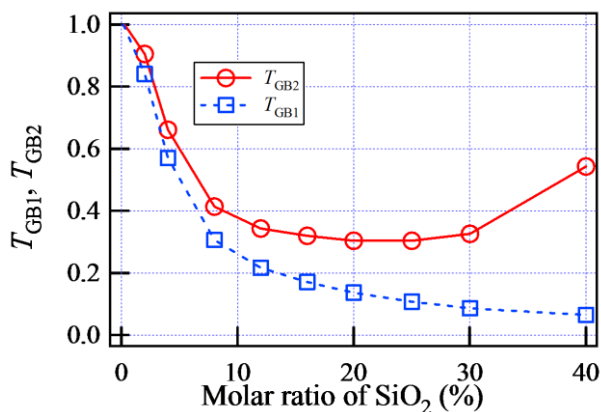


Figure 7.13 Relations between both T_{GB1} and T_{GB2} and molar ratio of SiO_2 .

7.4.2 Electrical degradation

Figure 7.14 (a) presents the nonlinear index before and after electrical degradation, α_{as} and α_{deg} , for ZBMCSiXB0. A small amount of SiO_2 to 6 mol% caused both α_{as} and α_{deg} to rise with increasing amounts of SiO_2 , although the α_{deg} was much smaller than α_{as} due to the electrical degradation occurred. After that, the α_{as} remained around 40-60 but the α_{deg} decreased suddenly with increasing amounts of SiO_2 . As a consequence, electrical degradation became much worse with SiO_2 above 6 mol%. Figure 7.14 (b) shows nonlinear index values before electrical degradation α_{as} for ZBMCSi0-40B0 and ZBMCSi0-40B1. α_{as} for both samples showed the similar SiO_2 dependence, became minimal at 0 and 12 mol% SiO_2 , maximal at 4 and 16 mol% SiO_2 , and became almost constant above 20 mol% SiO_2 . This result is discussed with ICTS later. Values of α_{as} for these samples ranged approximately from 26 to 68, except for the ZBMCSi0B0. the nonlinearity was markedly improved by adding SiO_2 , but not related to B_2O_3 . The leakage current density J_L at 30°C for ZBMCSi0-40B0 and ZBMCSi0-40B1 was less than $\approx 1 \times 10^{-6} \text{ A/cm}^2$ as shown in Fig. 7.14(c) and was value without the problem in practical uses. J_L decreased firstly with adding SiO_2 to around 10mol% and kept constant at $1 \times 10^{-7} \text{ A/cm}^2$,

increased with excessive amount above 25mol%.

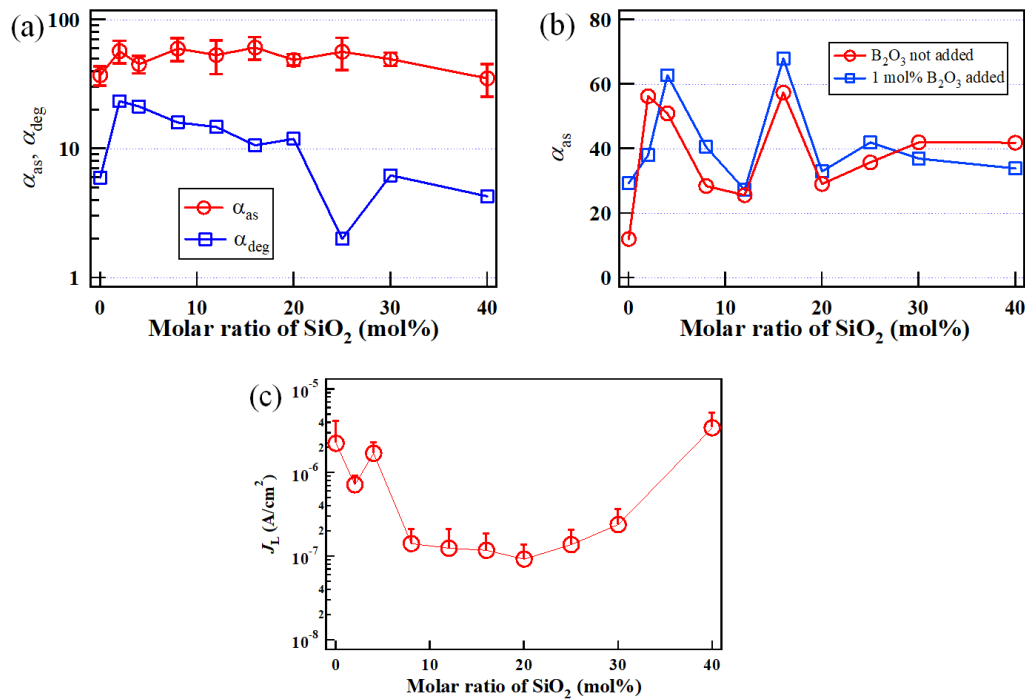


Figure 7.14 (a) Relationship between nonlinear index α_{as} before degradation and after degradation α_{deg} for ZBMCSiXB0. (b) comparison of α_{as} for ZBMCSiX with or without B, (c) leakage current J_L for ZBMCSiXB0.

Figure 7.15 shows the J_L – applying time of voltage characteristic at 130°C for 20 h in air, $J_{LD130^\circ C}$ is the leakage current density during electrical degradation. The voltage of 80 % of V_{NN} was applied. The initial value of J_L at 130°C was $\approx 5 \times 10^{-5} - 1.5 \times 10^{-4}$ A/cm² for ZBMCSi0-40B0 and was $\approx 1.6 \times 10^{-5} - 6.5 \times 10^{-5}$ A/cm² for ZBMCSi0-40B1. Because $V_N - J$ characteristics changed sharply from pre-breakdown to breakdown regions by adding B₂O₃, as described in section 7.4.1. $J_{LD130^\circ C}$ for ZBMCSi0-40B0 samples increased up to ≈ 100 times for 20 h with increasing time and as a result, $V_N - J$ characteristics were markedly degraded. On the other hand, $J_{LD130^\circ C}$ for ZBMCSi0-40B0 samples increased or decreased slightly for ZBMCSi0-4B0 with increasing time and as a result, the resistance to electrical degradation was drastically improved for all molar ratios of SiO₂ up to 40 mol% by adding 1 mol% B₂O₃.

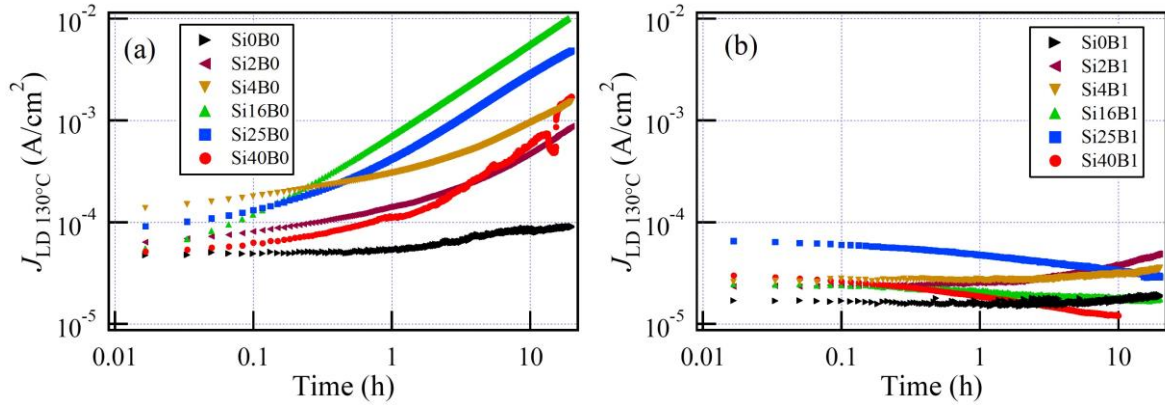


Figure 7.15 Change of leakage current density J_L at electrical degradation.

7.4.3 Interface state levels and barrier structure at grain boundaries

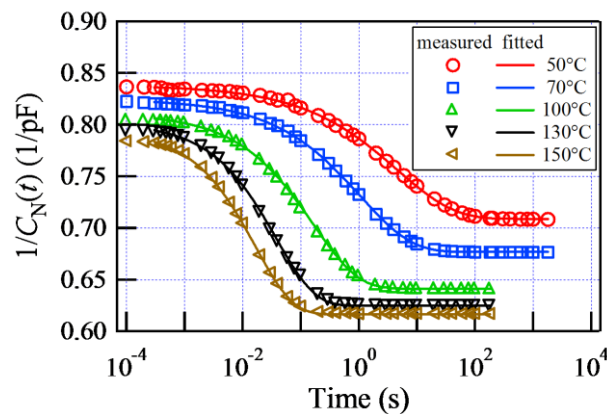


Figure 7.16 $1/C_N(t)$ -time characteristics at several temperatures for ZBMCSi16B1 applying a pulse from 0 to 114 V height for 20 ms.

The $C-V$ measurement method is effective in yielding the values of ϕ and N_D^{12} ; however, it becomes ineffective when the emission and/or capture of carriers by the trap levels at the grain boundaries and in ZnO grains occur. It is reported that the addition of SiO_2 increase the density of traps, which enhance the nonlinearity of $V_N - J$ characteristics²⁵⁻²⁷. Thus, interface states (trap) levels were analyzed by using ICTS. Solid lines in Figure 7.16 shows the fitted $1/C_N(t)-t$ characteristics for ZBMCSi25B2 assuming one kind of interfacial trap level, which is different than those Y-doped varistors. The fitted characteristics obtained by calculations were in good agreement with the measured characteristics. Similar good agreement was provided about other samples. Figure 7.17 (a) and (b) show the relationship between $E_C - E_T$ and CCA and the molar

ratio of SiO₂ to ZnO. $E_C - E_T$ is the depth of the interface trap level E_T measured from the bottom of the conduction band E_C . σ_n is the capture cross-section (CCA). Both $E_C - E_T$ and CCA for ZBMCSi0-40B2 samples were almost constant when SiO₂ changes and were ≈ 0.6 eV and $\approx 10^{-21}$ m² (≈ 0.02 nm radius), respectively. On the other hand, for ZBMCSi2-40B0, $E_C - E_T$ were not constant and especially CCA became much smaller than those for ZBMCSi0-40B2 samples. The value of $E_C - E_T$ increased slightly with increasing on the pulse height and the change width of $E_C - E_T$ was $\approx \pm 0.01$ around $E_C - E_T$ at the pulse height of 1/3 of varistor voltage.

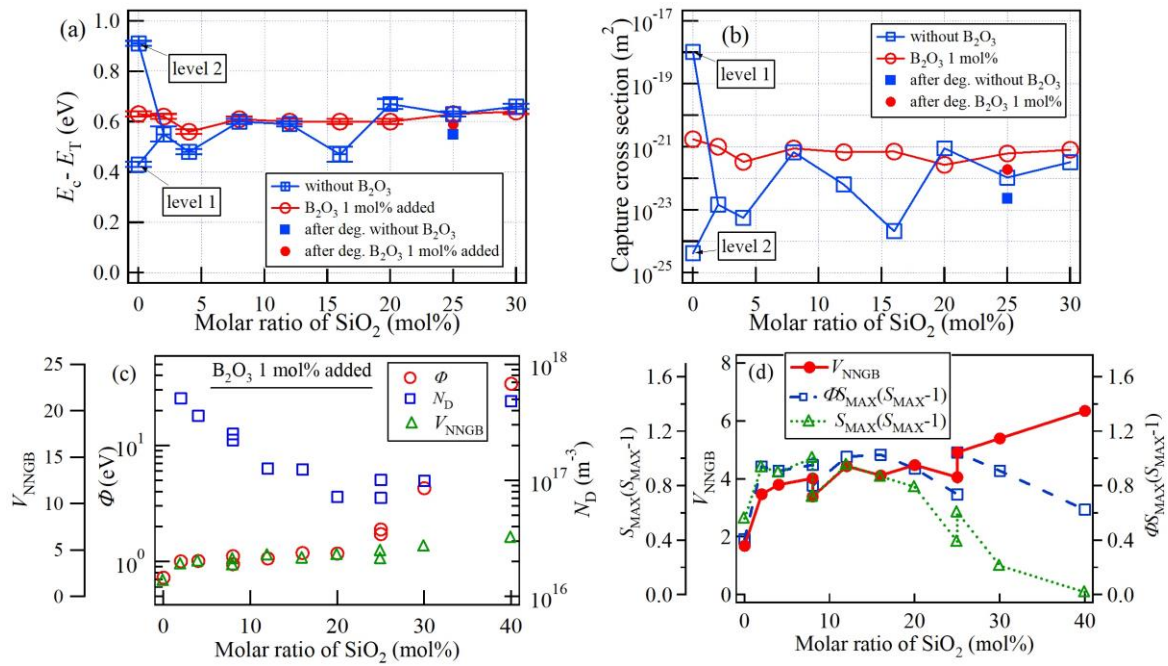


Figure 7.17 Relationship between the depth of (a) trap levels $E_C - E_T$ and (b) the cross-sectional area σ_n (CCA) and molar ratio of SiO₂, (c) N_D , Φ , and V_{NNGB} , (d) V_{NNGB} , $\Phi S_{MAX}(S_{MAX}-1)$, and $S_{MAX}(S_{MAX}-1)$.

The donor density N_D , Schottky barrier height Φ , single boundary varistor voltage V_{NNGB} and $S_{MAX}(S_{MAX} - 1)$ are presented in Fig.17 (c) and (d). The N_D decreased with increasing SiO₂ from 0 to 20mol%, then increased again with more. The Φ increased slightly with addition of SiO₂, and then became almost constant around 1.0 to 1.1eV when SiO₂ was below 25mol%; increased to 1.7eV at 25mol%. Above 25mol%, a sharp increase was found to 34eV, which should be impossible as the band gap for ZnO is 3.2eV. The $C-V$ measurement for ZnO varistors is not suitable in this case. However, the V_{NNGB} corresponds to Φ when SiO₂ was below 20mol%; after this the V_{NNGB} increased slightly, but not as much as Φ . A deeper look at

V_{NNGB} and Schottky barriers, interface states was shown in Fig.17 (d). S_{MAX} is the increase in the ratio of interface state densities to captured electrons at grain boundaries, as discussed in chapter 5. It was found that the V_{NNGB} is dependent on the product of $\Phi S_{\text{MAX}}(S_{\text{MAX}}-1)$ when SiO_2 was below 25mol%, which showed opposite increasement while $\Phi S_{\text{MAX}}(S_{\text{MAX}}-1)$ decreased as SiO_2 above 30mol%. This result indicates that the V_{NNGB} for SiO_2 added ZBMC varistors is dependent on the product of barrier height and the increase in the ratio of interface state density, which are affected by SiO_2 additives when SiO_2 amount is less than 25mol%, as the main structure at grain boundaries is ZnO homojunction between ZnO grains. However, when SiO_2 is above 25mol%, the main structure at grain boundaries turned to ZnO/willemite heterojunction as half of the ZnO changed to willemite (as discussed in chapter 7.3). This change was also observed under SEM. It is suggested that this change of ZnO homojunction to ZnO/willemite heterojunction led to the change in barrier height, as the measurement for ZnO varistors now is not suitable for heterojunction. However, the sample above 25mol% still showed varistor nonlinear V - J properties and the V_{NNGB} increased to 6 V with varistor voltage as high as 2700V/mm. Therefore, it is suggested that the ZnO/willemite heterojunction demonstrates nonlinear V - J properties, which needs further study in future.

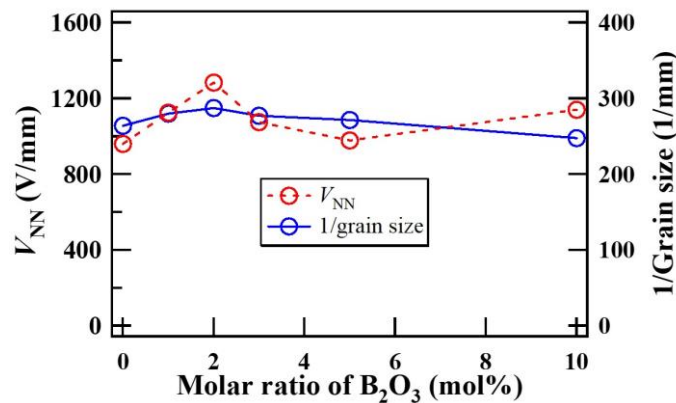


Figure 7.18 Relationship between varistor voltage or inverse of ZnO grain size and B₂O₃ content.

7.5 Effects of B₂O₃ on improvement of electrical degradation

The effects of the addition of B₂O₃ in this section. Figure 7.18 shows the varistor voltage V_{NN} and the inverse of ZnO grain size when changing the amount of B₂O₃ from 0 to 10 mol%. Varistor voltage and the inverse of ZnO grain size were largest when B₂O₃ was added 2.0 mol%.

When B_2O_3 was added more than 2 mol%, varistor voltage and the inverse of ZnO grain size decreased.

Figure 7.19 shows XRD patterns when changing amount of B_2O_3 . The diffraction peaks of β - Bi_2O_3 appeared only when B_2O_3 was not added, because Bi_2O_3 formed the amorphous borate glass with B_2O_3 less than 1 mol%. The diffraction patterns were almost the same when B_2O_3 of 1 – 5 mol% was added. However, when 10 mol% of B_2O_3 was added, the diffraction peaks of β - $Zn_3B_2O_6$ appeared. Because the diffraction peaks of any Bi_2O_3 disappeared, it is conjectured that Bi dissolved in $Zn_3B_2O_6$ or existed in the amorphous borate glass.

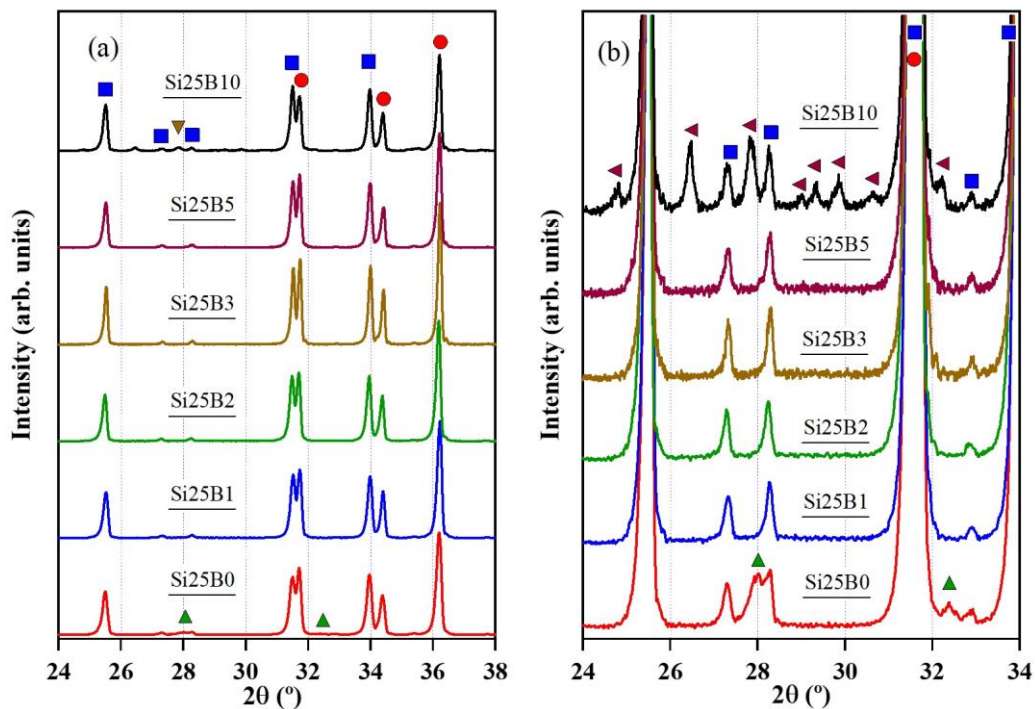


Figure 7.19 XRD patterns for compounds for ZBMCSi25BX samples ($X=0-10$). ●: ZnO, ■: willemite, ▲: β - Bi_2O_3 , ◄: β - $Zn_3B_2O_6$.

Figure 7. 20 shows the leakage current density at 130°C in air as a function of time for samples of ZBMCSi25B0–10. The J_L could be suppressed drastically by adding B_2O_3 of 2 – 5 mol%. However, J_L increased with increasing applying time. This is due to the be suppressed drastically by adding B_2O_3 of 2 – 5 mol%. The phenomenon electrical degradation is caused by movement of ions. B^{3+} ions existing in grain boundary block the movement of both Zn^{2+} and/or O^{2-} . As shown in BSE images and EDS element mapping for samples ZBMCSi25B0 and ZBMCSi25B2, Bi was distributed in boundaries between ZnO grains or between ZnO grain and willemite in ZBMCSi25B0. In the sample of ZBMCSi25B2, Bi was distributed in boundaries between ZnO grain and willemite or between willemite grains. Thus, addition B_2O_3

changed the position of Bi. However, B could not be distributed, it is considered that B existed in boundary with Bi due to the effect for electrical degradation.

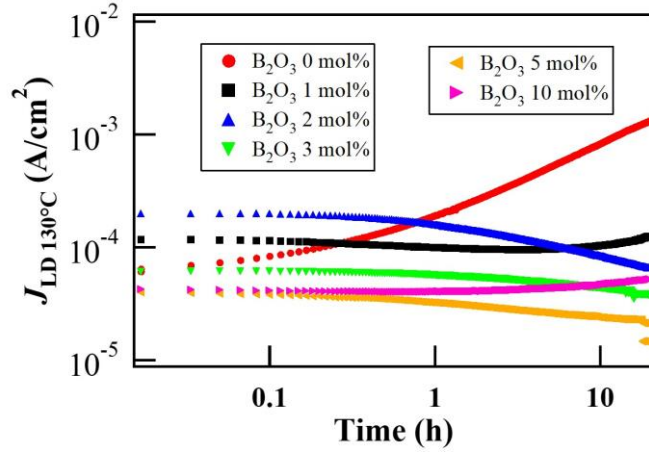


Figure 7.20 Time dependence of leakage current density J_L at 130°C for the samples of ZBMCSi25B0–10.

Figure 7.21 shows the E_C-E_T and CCA with B addition. E_T became shallower varied increasing the amount of B₂O₃ and became almost constant for the amount of 5 mol% and more than. CCA decreased with increasing the amount of B₂O₃. The formation of amorphous borate glass Bi-B-O at grain boundaries change the interface trap to shallower level, and decreased the capture cross area of traps. The shallower interface accelerates the capture of electrons at grain boundaries, that in turn to improve the resistance to electrical degradation as shown in Fig. 7.21.

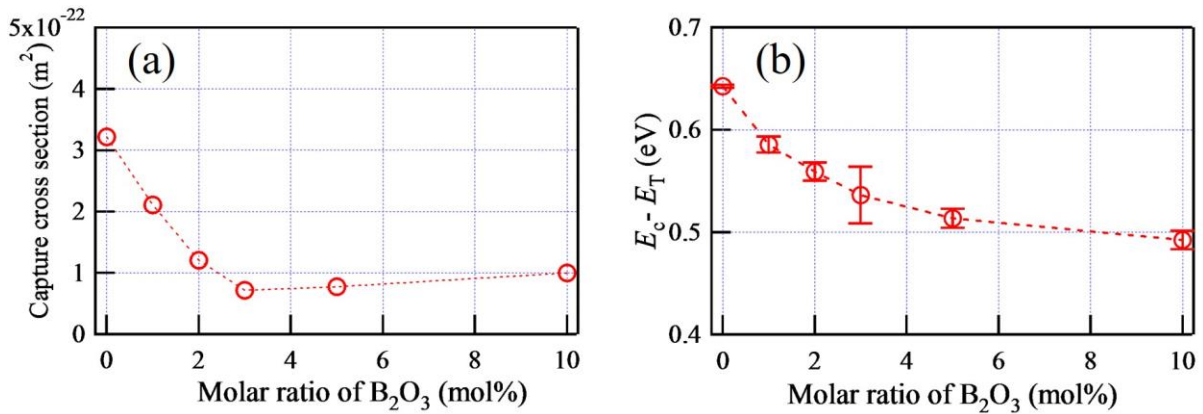


Figure 7.21 Relationship between (a) capture cross sectional area and (b) E_C-E_T and molar ratio of B₂O₃.

7.6 Conclusion

The addition of SiO_2 and B_2O_3 enhanced the sintering process. By adding SiO_2 to a standard Bi-based ZnO varistor, a high varistor voltage up to approximately 2500 V/mm can be achieved. Varistor voltages can be varied from 0 to 2500 V/mm by varying the amount of Si added. Additionally, by adding B_2O_3 , the increase in leakage current density under voltage could be drastically reduced. B_2O_3 , of a concentration of 2 mol% and less, primarily blocks the movement of Zn^{2+} ions and / or O^{2-} ions. This enhanced the resistance to electrical degradation. The above results indicate that it is possible to manipulate the varistor voltage by varying the amount of Si and fabricate a varistor with excellent electrical degradation resistance.

References

1. Matsuoka M. Nonohmic Properties of Zinc Oxide Ceramics. *Jpn J Appl Phys.* 10(1971)736–46.
2. Mahan GD. Intrinsic Defects in ZnO Varistors. *J Appl Phys.* 54(1983) 3825–32.
3. Eda K. Conduction Mechanism of Non-Ohmic Zinc-oxide Ceramics. *J Appl Phys.* 49(1978) 2964–72.
4. Eda K, Iga A, Matsuoka M. Degradation Mechanism of Non-Ohmic Zinc Oxide Ceramics. *J Appl Phys.* 51(1980)2678–84.
5. Chang YM, Kingery WD, Levinson LM. Compositional Change Adjacent to Grain Boundaries during Electrical Degradation of a ZnO Varistor. *J Appl Phys.* 53(1982)1765–8.
6. Gupta TK, Carlson WG. A Grain-boundary Defect Model for Instability/stability of a ZnO Varistor. *J Mater Sci.* (1985)3487–500.
7. Satoi Y, Hirai H, Yoshino H, Yoshikado S. The Effect of Si Addition on Electrical Degradation of ZnO Varistors. *Key Eng Mater.* (2005)281–4.
8. Yoshino Y, Takada M, Morioka J, Yoshikado S. Effects of Mn and Co Addition on Electrical Degradation of ZnO Varistors. *Key Eng Mater.* (2004)83–6.
9. Takada M, Yoshikado S. Relation between Grain Boundary and Electrical Degradation of ZnO Varistors. *Key Eng Mater.* 320(2006)117–20.
10. Takada M, Yoshikado S. Effect of SnO₂ Addition on Electrical Degradation of ZnO Varistors. *Key Eng Mater.* 350(2007)213–5.
11. Takada M, Yoshikado S. Effect of Thermal Annealing on Electrical Degradation Characteristics of Sb- Bi-Mn-Co-added ZnO Varistors. *J Eur Ceram Soc.* 30(2010)531–8.
12. Takada M, Sato Y, Yoshikado S. Relation between Grain Boundary Structure and Electrical Degradation in Zinc Oxide Varistors. *J Am Ceram Soc.* 95(2012)2579–86.
13. Ramírez MA, Simóes AZ, Bueno PR, Márquez A, Orlandi MO, Varela JA. Importance of Oxygen Atmosphere to Recover the ZnO-based Varistors Properties. *J Mater Sci.* 41(2006)6221–7.
14. Kim CH, Kim JH. Microstructure and Electrical Properties of ZnO-ZrO₂-Bi₂O₃-M₃O₄ (M=Co, Mn) Varistors. *J Eur Ceram Soc.* 24(2004)2537–46.
15. Bernik S, Daneu N. Microstructural and Electrical Characteristics of Y₂O₃-doped ZnO-Bi₂O₃-based Varistor Ceramics. *J Eur Ceram Soc.* 21(2001)1879–82.

16. Bernik S, Macek S, Bui A. The Characteristics of ZnO-Bi₂O₃-based Varistor Ceramics Doped with Y₂O₃ and Varying Amounts of Sb₂O₃. *J Eur Ceram Soc.* 24(2004)1195–8.
17. Y, Takada M, Fukumori A, Sato Y, Yoshikado S. Effects of Zr and Y Addition on the Electrical Degradation Characteristics of ZnO Varistors. *Key Eng Mater.* 445(2010)237–40.
18. Watanabe T, Fukumori A, Akiyama Y, Sato Y, Yoshikado S. Effect of Simultaneous Addition of Zr and Y on Electrical Degradation of ZnO Varistors. *Key Eng Mater.* 485(2011) 257–60.
19. Takemura T, Kobayashi M, Takada Y, Sato K. Effect of Antimony Oxide on the Characteristics of ZnO Varistors. *J Am Ceram Soc.* 70(1987)237–41.
20. Mahan GD. Intrinsic Defects in ZnO Varistors. *J Appl Phys.* 54(1983)3825-3832.
21. Tanigawa A, Hirota M, Sakaguchi T, Yoshikado S. Evaluation of the Degradation for ZnO Varistor with Various Additives. *Trans IEE FM.* 118-A(1998)169-175.
22. Chang YM, Kingery WD, Levinson LM. Compositional Changes Adjacent to Grain Boundaries during Electrical Degradation of a ZnO Varistor. *J Appl Phys.*(1982)1765-1768.
23. Gupta TK, Carlson WG. A Grain-Boundary Defect model for Instability / stability of a ZnO Varistor. *J Mater Sci.* 20(1985)3487-3500.
24. Kurokawa K, Sato Y, Yoshikado S. Electrical characteristics of SrCoO₃ – added zinc oxide varistors. *J Ceram Soc Jpn.* 123(2015)583-588.
25. Shao Q, Gao XH, Cao ZC. Effect of annealing on phase structure and degradation of a zinc oxide varistor with Si-additive. *J Eur Ceram Soc.* 17(1997)55–9.
26. Satoi Y, Hirai H, Yoshino H, Morioka J, Yoshikado S. The effects of Si addition on electrical degradation of ZnO varistors. *Key Eng Mater.* 269(2004)83–6.
27. Takada M, Sato Y, Yoshikado S. Relation between grain boundary structure and electrical Degradation in zinc oxide varistors. *J Am Ceram Soc.* 95(2012)1–8.
28. Bai H, Zhang M, Xu Z, et al. The Effect of SiO₂ on electrical properties of low-temperature sintered ZnO-Bi₂O₃-TiO₂-Co₂O₃-MnO₂-based ceramics. *J Am Ceram Soc.* 100(2017)1057-1064.
29. Einzinger R. Metal oxide varistors. *Annu Rev Mater Sci.* 17(1987)299-321.
30. Kutty T, Ezhilvalavan S. The role of silica in enhancing the nonlinearity coefficients by modifying the trap states of zinc oxide ceramic varistors. *J Phys D: Appl Phys.* 29(1996)809-819.

31. So SJ, Park CB. Improvement in the electrical stability of semiconducting ZnO ceramic varistors with SiO₂ additive. *J Korean Phys Soc.*40(2002)925-929.
32. Wu ZH, Fang JH, Xu D, Zhong QD, Shi LY. Effects of SiO₂ addition on the microstructure andn electrical Properties of ZnO-based varistors. *Int. J Mener Mater.* (2010)86-91.
33. Klaska KH, Eck JC, Pohl D. New investigation of willemite. *Acta Crystallographica* B34(1978)3324-3325.
34. Monerreau O, Tortet L, Llewellyn, Rouquerol F, Vacquier G. Synthesis Bi₂O₃ by controlled transiformalion rate thermal analysis: a new route for this oxide. *Solid State Ionics* (2003)163
35. Wan S., Wenzhong L, Wang X. Low-temperature sintering and electrical properties of ZnO–Bi₂O₃–TiO₂–Co₂O₃–MnCO₃-based varistor with Bi₂O₃–B₂O₃ Frit for multilayer chip varistor applications. *J Am Ceram Soc.* (2010)3319–3323.
36. Harwig, HA, Gerards, AG. Electrical-properties of alpha, beta, gamma and delta phases of bismuth sesquioxide. *J. Sol. Stat. Chem.* (1978)265–274.
37. Pérez-Mezcua D, Bretos I, Jiménez R, Ricote J, Jiménez-Rioboó RJ., Gonçalves da Silva C, Chateigner D, Fuentes-Cobas L, Sirera R, Calzada ML. Photochemical solution processing of films of metastable phases for flexible devices: the β-Bi₂O₃ polymorph. *Scientific Reports.* (2016)1-10.

Chapter 8

Conclusion and outlook

In this thesis, the author investigated high voltage Bi-based ZnO varistors with a voltage of up to 1000V/mm (double the commercial varistor voltage) that offer good electrical degradation resistance, which can be used as surge arresters in UHV transmission systems.

The electrical properties of ZnO varistors have been controlled by adjusting additive type and amount. Y_2O_3 was added to commercial ZnO varistors to more than double the varistor voltage. The varistor voltage was highly dependent on the ratio of Y_2O_3 to Sb_2O_3 . Doping Y, however, caused severe leakage currents. To improve the stability and solve the leakage current problem of the Y-doped ZnO varistors for real world applications, additives that may inhibit the electrical degradation were investigated (i.e., Cr, Ni and B). As a result, Y-doped varistors with excellent stability and resistance to degradation were successfully fabricated.

The effects of Cr and/or Ni into Y-doped varistors were studied in chapter 5, including electrical properties, microstructure, interface states and barrier structure at grain boundaries. Varistor voltage was increased more than 1000 V/mm with addition of Cr and/or Ni. Incorporating 0.35 mol% Cr_2O_3 in Y-doped varistors increased single-grain varistor voltage V_{NNGB} from 2.6 to 3.3 V and decreased the leakage current density from 2×10^{-5} to 5×10^{-7} A/cm². Nonlinearity index α before and after degradation increased from 21 to 35. By applying a bias roughly 80% of varistor voltage, the samples experience negligible degradation even at high temperature for a long time, showing strong stability. When adding 1.2 mol% NiO, V_{NNGB} increased to 4V. The highest varistor voltage was 1500 V/mm for 0.3 mol% NiO. Resistance to electrical degradation improved with optimal amounts of Cr or Ni by reduction in grain boundary oxygen vacancies. Though donor density was prominently changed by addition of Cr and/or Ni, the change of barrier height was suppressed by the change of interface state density. By analyzing the interface states and Schottky barrier parameters in combination with the electrical properties, we discovered that either Cr or Ni increased the rate of change of interface state density at grain boundaries, which showed a strong correlation to V_{NNGB} . As a result, the change of V_{NNGB} was related mainly to the empty interface state density under no bias. The electrical properties of ZnO varistors and the interface states have been analyzed using a simulation based on thermionic emission.

Furthermore, the effects of Cr and/or Ni were different in samples without Y. When Cr or Ni were added to samples without Y, no obvious improvement to electrical degradation was

found. This may be due to the lack of a Bi-layer in Y-doped varistors which enhanced the effects of Cr or Ni at the interfaces. When no Y was doped in samples, the Bi-layer at grain boundaries absorbed the Cr and Ni, eliminating their effects on electrical degradation and interface states.

In chapter 6, the effects of B_2O_3 addition to Y-doped varistors were studied. The optimal amount of B_2O_3 (0.75 mol%) drastically improved the electrical properties of Y-doped varistors, reducing the leakage current to $0.8 \mu A/cm^2$ while maintaining exceptionally long-term stability to DC electrical degradation and a voltage around 900 V/mm. Boron ions are found with Bi ions in Y-compounds, which contribute to the formation of a Bi-rich glass phase containing B at grain boundaries when B_2O_3 is above 0.75 mol%. The change in microstructure affected the donor density and barrier structure leading to a change in electrical properties. The Bi-rich phase first reduced Co concentration in the ZnO grain, decreasing donor density N_D . Then, when B_2O_3 was greater than 1 mol%, the excessive B ions acted as donors to increase N_D .

In addition, the relationship between B_2O_3 and SiO_2 in Y-doped varistors was also discussed. The glass phase of B-Si-O was found at grain boundaries under TEM, which affects the efficacy of B_2O_3 additives. An excess of B_2O_3 and SiO_2 produced a glass phase of Bi-B-Si-O at grain boundaries, exacerbated electrical degradation resistance, and resulted in a larger leakage current.

A new analytical method using differential resistance R_D of the nonlinear voltage–current density relation was also proposed and explained in chapter 6, to clarify the effects of B_2O_3 addition. This method separates the three-differential resistance R_{D_i} values ($i = 1, 2, 3$) and was used to analyze the corresponding conduction process located in forward-biased region I, reverse-biased region III, and interface region II of the energy band. The R_{D1} and R_{D2} values exhibited a junction diode-like property in regions I and III. The value of R_{D2} that correlated with α_{asMAX} and long-term stability of varistor and R_{D3} may be related to region II. This method shows good consistency to electrical properties. A deeper understanding of the physical connections and explanations is still needed.

In future, further study of the analytical method using differential resistance R_D is needed. This method may be able to be applied to other types of ZnO varistors or even to similar materials that involve barrier effects. The author expects to use this method in other recipes of ZnO varistors. It may be first time to determine the barrier region and conductance process in an equation. In addition, one of the arctan equations may be related to the tunneling effect. It may also match the other Zener diode or avalanche diode reversed bias breakdown effect.

Next, in order to reduce the amount of additives and keep high voltage and good electrical properties while reducing cost of materials and removing toxic antimony oxides, the effects of SiO₂ additives were investigated as a replacement for Y-Sb co-doping.

In Chapter 7, SiO₂ addition to Zn-Bi-Co-Mn varistors was investigated. Varistor voltage increased as Si content increased due to the formation of second phase Zn₂SiO₄ that inhibited ZnO grain growth. However, the resistance to electrical degradation also decreased. Therefore, B was added into Si-doped ZnO varistors to improve the resistance to degradation. It is considered that the resistance to electrical degradation is improved upon addition of B by its combination with ions in grains and prevention of ion movement. Furthermore, it was found that Bi-Mn-Co-Si-B added ZnO varistors have good resistance to electrical degradation characteristics and the varistor voltage can be controlled by manipulating the amounts of Si and B. The relationship between Bi₂O₃ amount and SiO₂, B₂O₃ was also discussed.

Chapters 5 and 6 of the author's thesis have been published in two prominent journals. The other work will be edited and submitted at a later date.

Publications in this thesis are listed below:

1. Y. Zheng, M. Fujimoto, Y. Sato, S. Yoshikado, Effects of addition of chromium and/or nickel oxides on the electrical characteristics of yttrium oxide-doped high-voltage zinc oxide varistors, *J. Eur. Ceram. Soc.* 41 (2021) 4841–4849.
2. Y. Zheng, Y. Sato, S. Yoshikado, Effects of boron oxide addition on electrical properties of yttrium-doped bismuth-based zinc oxide varistors, *Mater. Chem. Phys.* (2021)125390.
3. T. Maegawa, Y. Zheng, Y. Kataoka, Y. Sato, S. Yoshikado, Electrical Characteristics of High Voltage Bismuth-based Zinc Oxide Varistors added Silicon Oxide and Boron oxide. (editing)

ACKNOWLEDGEMENTS

It is my great pleasure to express my deep gratitude to Professor Yoshikado, my supervisor, who has helped me in these 5 years from my master's to my Ph.D. studies here in Japan, for his patient guidance, enthusiastic encouragement, and useful critiques of my research. In addition to my thesis, I gained an understanding of electrical and electronic materials in general. During our conversations, I expanded a broader perspective on science and learned more about the life of a researcher. The positive attitude he has and the knowledge he shares strongly influence me. I hope that I will be able to follow in his footsteps and have a bright future like my supervisor.

I would like to thank Professor Sato for his kind support and valuable advice on both life and research. Throughout my studies, Professor Sato helped me solve problems I encountered and taught me a lot. I felt such an immense warmth living in a foreign country because of his warmheartedness.

I would also like to extend my thanks to Mrs. Toda of the laboratory of the microscope for helping and teaching me to use the SEM and TEM. Her rigorous and great technique inspired me to find the key point in my materials.

In particular, I would like to thank Mr. Maegawa, Mr. Kawasaki, and Mr. Fujimoto for their assistance. Having them as collaborators was an absolute pleasure. It was a pleasure to stay at our laboratory while I was in Japan, and I thank everyone for their kind assistance. I am grateful to them for their patience and kindness, teaching me Japanese, and helping me navigate Japan. It has been a wonderful experience studying here for these years with them. Thank you also to my friends in Japan for their support, which gives me the strength to continue my studies.

A special thanks should be given to my motherland, China, for supporting me in receiving a scholarship so that I could conduct research in Japan without having to worry about my safety. The strong support and care they provided to every Chinese student in Japan during the difficult days with Corona virus warmed our hearts.

Finally, I wish to thank my family members and Kyle for their support and encouragement throughout my study.

Yumeng ZHENG
19th, November 2021
Kyoto, Japan